FACULTY
OF MATHEMATICS
AND PHYSICS
Charles University

MASTER THESIS

Filip Chudoba

Magnetic domain study in non-collinear antiferromagnets and altermagnets

Department of Chemical Physics and Optics

Supervisor of the master thesis: RNDr. Eva Schmoranzerová Ph.D.
Study programme: Optika a optoelektronika

Prague 2025

I declare that I carried out this master thesis on my own, and only with the cited sources, literature and other professional sources. I understand that my work relates to the rights and obligations under the Act No. 121/2000 Sb., the Copyright Act, as amended, in particular the fact that the Charles University has the right to conclude a license agreement on the use of this work as a school work pursuant to Section 60 subsection 1 of the Copyright Act.

In .... date ....

Author's signature

This thesis would not have been possible without the support of many individuals. I am deeply grateful to my supervisor, Eva Schmoranzerová, for her unwavering guidance, insightful advice, and constant availability throughout this journey.

I sincerely thank Ivan Soldatov and Rudolf Schäfer from IFW Dresden for providing access to their laboratory, facilitating wide-field MOKE microscopy measurements, and offering invaluable assistance with data acquisition and interpretation.

I am grateful to Antonín Baďura, Zbyněk Šobáň, and Helena Reichlová from the Institute of Physics of the Czech Academy of Sciences for the preparation of samples for thermoscanning measurements and insightful discussions on the results.

I want to express my gratitude to David Schmoranzer from the Department of Low Temperature Physics for developing the software that enabled the thermoscanning measurements.

Furthermore, I am thankful to Irena Matulková from the Faculty of Science for conducting Raman spectroscopy measurements, which significantly aided in interpreting the obtained results.

Finally, I wish to express my appreciation to my friends and family for their unwavering support and encouragement throughout my academic journey.

I acknowledge the use of generative language models Grammarly, ChatGPT, and Gemini to enhance the readability and comprehensiveness of this text. These tools were also used to refine Python scripts for data visualization.

Title: Magnetic domain study in non-collinear antiferromagnets and altermagnets

Author: Filip Chudoba

Department: Department of Chemical Physics and Optics

Supervisor: RNDr. Eva Schmoranzerová Ph.D., Department of Chemical Physics and Optics

Abstract: This thesis explores magnetic domain imaging in non-collinear antiferromagnetic and altermagnetic materials using thermoscanning and wide-field MOKE microscopy. Thermoscanning of non-collinear antiferromagnet Mn3GaN revealed Seebeck-effect-dominated signals, confirming the Γ5g phase with suppressed Berry curvature contributions. Wide-field MOKE microscopy of the altermagnetic semiconductor MnTe identified reproducible, thermally induced reflectivity patterns linked to strain effects and Te precipitates rather than magnetism, likely caused by thermal expansion mismatches and defects. Complementary Raman spectroscopy supported these findings. While direct magnetic domain imaging was not achieved, the results establish the groundwork for future studies, emphasizing the importance of optimized methodologies and complementary techniques.

Keywords: magnetic domains, Kerr microscopy, altermagnets

Název práce: Studium magnetických domén v nekolineárních antiferomagnetech a altermagnetech

Autor: Filip Chudoba

Katedra: Katedra Chemické fyziky a optiky

Vedoucí magisterské práce: RNDr. Eva Schmoranzerová Ph.D., Katedra chemické fyziky a optiky

Abstrakt: Tato práce zkoumá zobrazování magnetických domén v nekolinerárních antiferomagnetických a altermagnetických materiálech pomocí termoskenování a MOKE mikroskopie v širokém poli. Termoskenování nekolinerárního antiferomagnetu Mn3GaN odhalilo signály dominované Seebeckovým efektem, což potvrdilo přítomnost fáze Γ5g s potlačenými příspěvky Berryho křivosti. MOKE mikroskopie altermagnetického polovodiče MnTe identifikovala reprodukovatelné, tepelně indukované vzory odlišné odrazivosti, které byly spojené spíše s vlivy napětí a precipitáty Te než s magnetismem, pravděpodobně způsobené rozdílnou tepelnou roztažností a defekty. Doplňková Ramanova spektroskopie tato zjištění podpořila. Ačkoli nebylo dosaženo přímého zobrazení magnetických domén, výsledky vytvářejí základ pro budoucí studie a zdůrazňují význam optimalizovaných metodologií a doplňkových technik.

Klíčová slova: magnetické domény, Kerrovská mikroskopie, altermagnety

Contents

Introduction

The field of semiconductor electronics has driven significant technological progress over recent decades. However, as traditional charge-based electronics approach the physical limits of miniaturization, they face increasing challenges, particularly in energy efficiency and scalability. Spintronics, which leverages the spin of electrons in addition to their charge, offers a promising alternative. By harnessing electron spin, spintronic devices aim to deliver faster data processing, nonvolatile memory, and reduced energy consumption [1].

While early spintronic research centred on ferromagnetic materials, recent advancements have highlighted the unique potential of antiferromagnets and altermagnets [2, 3]. These materials exhibit ultrafast spin dynamics, resilience to external magnetic fields, and symmetry-driven spin textures, making them particularly appealing for next-generation devices. However, their complex spin configurations and the challenges of visualizing and manipulating their magnetic domains remain significant hurdles [4, 5].

The ability to image and understand magnetic domains is critical for the advancement of spintronic technologies. Magnetic domains govern key material properties, influencing transport and magnetotransport phenomena that are fundamental to device operation. Techniques for accurate domain visualization and control enable the optimization of devices such as antiferromagnetic MRAM, racetrack memory, and energy-efficient logic circuits. Altermagnets, in particular, with their symmetry-driven spin dynamics, offer exciting possibilities for applications in high-speed logic and sensing [6]. Despite these promising opportunities, many of these concepts remain in the experimental phase, requiring further refinement before practical implementation [1].

Investigating magnetic domain structures provides insights into how spin alignment and domain configurations influence macroscopic properties. By mapping these structures, researchers can optimize spintronic materials for specific applications. For instance, controlling domain reorientation could improve switching mechanisms in memory devices, while tailored domain configurations could enhance spin transport efficiency in logic circuits. Addressing the challenges associated with magnetic domain imaging and control thus represents a critical step in unlocking the full potential of spintronic materials across computing, sensing, and other technologies [7, 4].

This thesis employs two complementary techniques to study magnetic domains: wide-field magneto-optical Kerr effect (MOKE) microscopy and Scanning thermal gradient microscopy (STGM). Wide-field MOKE microscopy, with its high spatial resolution, excels at imaging surface magnetization and revealing domain configurations [7]. STGM, on the other hand, investigates domains by detecting thermally induced voltage signals, providing an indirect yet powerful method for exploring magnetic order [5, 4]. Together, these methods offer a comprehensive toolkit for characterizing the intricate magnetic structures in non-collinear antiferromagnetic and altermagnetic materials, paving the way for their integration into future spintronic applications.

This thesis is structured into four main chapters. The first chapter provides a theoretical introduction to magnetic ordering in solids, exploring the origins of magnetic order, the different types of magnetically ordered materials, and introducing the concept of altermagnetism. The second chapter focuses on the primary materials investigated in this work: altermagnetic MnTe and non-collinear antiferromagnetic Mn_3GaN. The third and fourth chapters are dedicated to the experimental methods. Chapter three details the STGM measurements, while chapter four examines the wide-field MOKE microscopy. Each experimental chapter outlines the theoretical principles, describes the methodologies, and discusses the results.

1 Introduction to magnetism

Magnetism is a fundamental property in materials rooted in the quantum mechanical characteristics of electrons. The magnetic moment of an electron, $\vec{m}$, originates from its intrinsic spin and its orbital motion around the nucleus and can be described by the operator $\hat{m}$. This magnetic moment can be expressed as [8]:

$$\hat{m} = -(\mu_B/\hbar)(\hat{l} + 2\hat{s}) \tag{1.1}$$

where μ_B is the Bohr magneton ($\mu_B = \frac{e\hbar}{2m_e}$) [9], $\hat{l}$ is the orbital angular momentum operator, and $\hat{s}$ is the spin angular momentum operator. In a macroscopic solid, the net magnetization $\vec{M}$ is defined as the vector sum of all individual magnetic moments per unit volume [8]:

$$\vec{M} = \frac{\sum_i \vec{m}_i}{V} \tag{1.2}$$

where V is the volume of the material, and $\vec{m}_i$ is each electron's magnetic moment.

When a material is subjected to an external magnetic field $\vec{H}$, the combined effect of the field and the material's own magnetization $\vec{M}$ creates magnetic induction $\vec{B}$, given by [8]:

$$\vec{B} = \mu_0(\vec{H} + \vec{M}) \tag{1.3}$$

where μ_0 is the magnetic permeability of a free space. This relation illustrates how the material's internal magnetic moments respond to the external field, being aligned or opposite to it, depending on the material's intrinsic magnetic properties. In ferromagnetic materials, strong internal alignment leads to a large net magnetization, while in diamagnetic materials, the response is weak and opposite to the external field [10]. Other forms of magnetic ordering, such as antiferromagnetic and altermagnetic, are discussed in more detail in later sections (1.3, 1.4), while ferrimagnetic ordering is omitted, as it is not relevant to the scope of this work.

The magnetic properties of materials come from the quantum mechanical characteristics of electrons, particularly their spin and orbital angular momentum. These intrinsic properties of electrons result from solutions of the Dirac equation [11], which describes the behaviour of particles with spin. When an electron is in the presence of an external magnetic field $\vec{B}$, the interaction between the field and the electron's magnetic moment $\vec{m}$ results in an energy shift known as the Zeeman effect. The Zeeman interaction, which couples $\vec{m}$ to the field, is given by [8]:

$$H_z = -\vec{m} \cdot \vec{B} = (\mu_B/\hbar)(\hat{l} + 2\hat{s}) \cdot \vec{B} \tag{1.4}$$

This interaction causes magnetic moments to align parallel or antiparallel to the field, depending on their relative energy states. The total magnetic moment in atoms or ions with many electrons results from the combined contributions of each electron's spin and orbital moments, with these interactions modified by the local environment in the crystal structure [9].

1.1 Exchange interactions and magnetic ordering

The alignment of magnetic moments in solids is predominantly determined by the exchange interaction, a quantum mechanical effect arising from the Pauli exclusion principle and the Coulomb repulsion between electrons. The exchange interaction dictates the alignment of the neighbouring electron spins, which defines the material's type of magnetic ordering. The Hamiltonian for the exchange interaction between two spins $\vec{S_1}$ and $\vec{S_2}$ is represented by:

$$H = -2J\vec{S_1} \cdot \vec{S_2} \tag{1.5}$$

where J is an exchange integral. A positive J indicates ferromagnetic interaction, which tends to result in parallel spin alignment, while a negative J indicates antiferromagnetic interaction, which tends to align the two spins antiparallel [8].

How magnetic moments interact varies with the spatial arrangement and distance between magnetic ions. Direct exchange occurs in ferromagnetic materials, where the atoms are closely packed. Electron orbitals overlap directly, resulting in a strong exchange interaction aligning neighbouring spins parallel to each other. This mechanism is the principal driver of ferromagnetic ordering, where the entire material exhibits a net magnetic moment due to the cooperative alignment of all the spins [10].

In certain insulating materials, where magnetic ions are separated by non-magnetic atoms, a different interaction, known as superexchange, influences the spin alignment. In these cases, the non-magnetic atoms act as a bridge, facilitating an indirect exchange between neighbouring ions. Superexchange interactions often lead to antiferromagnetic ordering, where the spins of adjacent magnetic ions align antiparallel. This indirect interaction allows for stable antiparallel configurations even in the absence of direct overlap between magnetic ions [10].

Metals with conduction electrons can exhibit another exchange interaction known as RKKY (Ruderman-Kittel-Kasuya-Yosida) interaction, first theorized in [12]. Here, the conduction electrons mediate an oscillating exchange interaction between distant magnetic ions. As the distance between ions increases, the RKKY interaction alternates between ferromagnetic and antiferromagnetic alignment. It is significant mainly in dilute magnetic alloys and metallic compounds with magnetic impurities. The oscillating nature of the RKKY interaction is due to the conduction electrons' ability to convey magnetic information over long distances, providing a mechanism for complex magnetic ordering across the lattice [10].

The final type of exchange interaction, known as DMI (Dzyaloshinsky-Moriya interaction), originates from an exchange interaction between two magnetic ions. In this interaction, the ground state of one of the ions interacts with the excited state of a neighbouring ion, with the excitation caused by spin-orbit interaction. When acting on two spins $\vec{S_1}$ and $\vec{S_2}$, it results in the Hamiltonian H_{DM} [10]:

$$H_{DM} = \vec{D} \cdot (\vec{S_1} \cdot \vec{S_2}) \tag{1.6}$$

where $\vec{D}$ is a vector that vanishes in systems with spatial inversion symmetry. This interaction causes $\vec{S_1}$ and $\vec{S_2}$ to be perpendicular to each other and is commonly observed in antiferromagnets where it tilts the antiferromagnetically aligned spins to produce a small net ferromagnetic moment. Materials with this behaviour are known as weak ferromagnets [10], [8].

These exchange mechanisms—direct exchange, superexchange, RKKY and the DM interaction—illustrate the diversity of magnetic behaviour in solids. From the straightforward parallel alignment in ferromagnetic materials to the more complex, often frustrated arrangements in antiferromagnets and dilute magnetic systems, exchange interactions lie at the heart of magnetic ordering.

1.2 Magnetic susceptibility and temperature dependence

The response of a material to an external magnetic field is measured by its magnetic susceptibility χ, defined as the ratio of magnetization M to the applied magnetic field B [9]:

$$\chi = \frac{\mu_0 M}{B} \tag{1.7}$$

In paramagnetic materials, where magnetic moments tend to align with the field, susceptibility follows Curie's law at high temperatures [9]:

$$\chi = \frac{C}{T} \tag{1.8}$$

where C is the Curie constant, and T is the absolute temperature. Curie's law demonstrates how thermal energy influences susceptibility: as the temperature rises, thermal agitation disrupts alignment, reducing the susceptibility as illustrated in Fig. 1.1. In materials with ordered magnetic structures, such as ferromagnets or antiferromagnets, the relationship between χ and T diverges from Curie's law due to the additional stabilizing effect of exchange interactions. These interactions impose stronger alignment constraints below certain critical temperatures, such as the Curie temperature for ferromagnets and the Néel temperature for antiferromagnets. Below these critical temperatures, the magnetic moments in the material become increasingly ordered, giving rise to spontaneous magnetization in ferromagnets or antiparallel ordering in antiferromagnets. This temperature-dependent behaviour is crucial in phase transitions, as observed in materials used for data storage, sensors, and magnetic memory [9, 8].

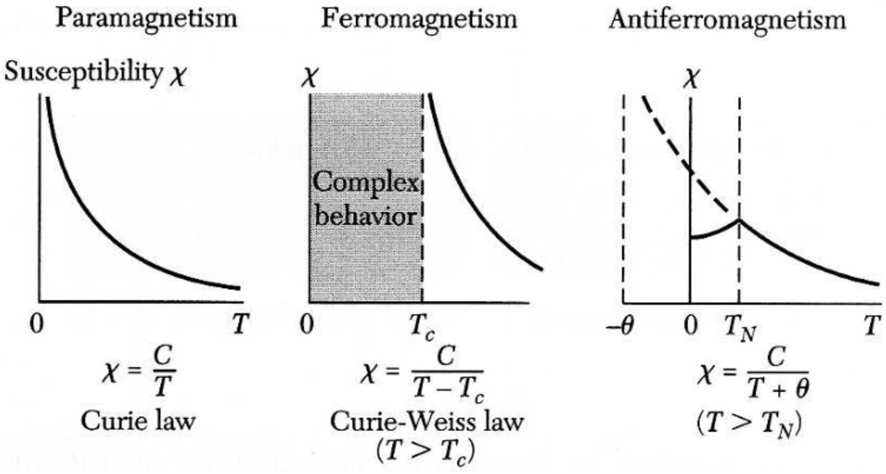

Figure 1.1 Temperature dependence of the magnetic susceptibility in paramagnets, ferromagnets, and antiferromagnets. Below the Néel temperature of an antiferromagnetic, the spins have antiparallel orientations; the susceptibility attains its maximum value at T_N where there is a well-defined kink in the curve of χ versus (T). Adapted from [9].

1.3 Antiferromagnetism

Antiferromagnetism is a type of magnetic ordering where neighbouring magnetic moments align antiparallel, resulting in a net-zero magnetization. This alignment minimizes the system's energy, as a negative exchange interaction favours opposite spin orientations for adjacent ions. In an antiferromagnetic material, two interpenetrating sublattices (A and B) exhibit equal but opposite magnetizations, such that $M_A = -M_B$ [8].

This antiparallel configuration is often stabilized by superexchange interactions, particularly in compounds where magnetic ions are separated by non-magnetic atoms, which mediate an indirect coupling. This indirect exchange aligns neighbouring spins in opposite directions, leading to strong local magnetic moments that cancel each other macroscopically [8].

Antiferromagnetic order remains stable only below a critical temperature known as the Néel temperature T_N. Above T_N, thermal energy disrupts the antiparallel alignment, causing the material to transition to a paramagnetic state where the magnetic moments are randomly oriented. In this high-temperature state, the susceptibility χ of an antiferromagnetic can be described by the modified Curie-Weiss law [8]:

$$\chi = \frac{C}{T+\theta} \tag{1.9}$$

where C is the Curie constant, and θ is typically negative, indicating a preference for antiparallel alignment. This negative intercept represents the stabilizing effect of the exchange interactions that drive antiferromagnetic ordering. Below the Néel temperature, susceptibility decreases as temperature drops (see Fig. 1.1), reflecting the stability of the ordered antiparallel configuration, which limits the magnetic response to external fields. The Néel temperature can vary widely among antiferromagnetic materials depending on factors such as exchange strength and lattice geometry [9].

1.3.1 Non-collinear antiferromagnetism

In addition to collinear structures, certain antiferromagnetic materials exhibit non-collinear configurations, where spins align at specific angles rather than strictly antiparallel. These arrangements commonly arise from geometric constraints or lattice symmetries that prevent a collinear antiparallel configuration [8].

A prominent and, for this work, most relevant example of non-collinear antiferromagnetism is found in triangular antiferromagnets; see Fig. 1.2. In these, the magnetic moments are arranged in a triangular pattern, with spins aligned at 120° relative to their neighbours. This configuration results from geometric frustration where each spin cannot align directly opposite to all its neighbours, so the system adopts a compromise structure [8, 13].

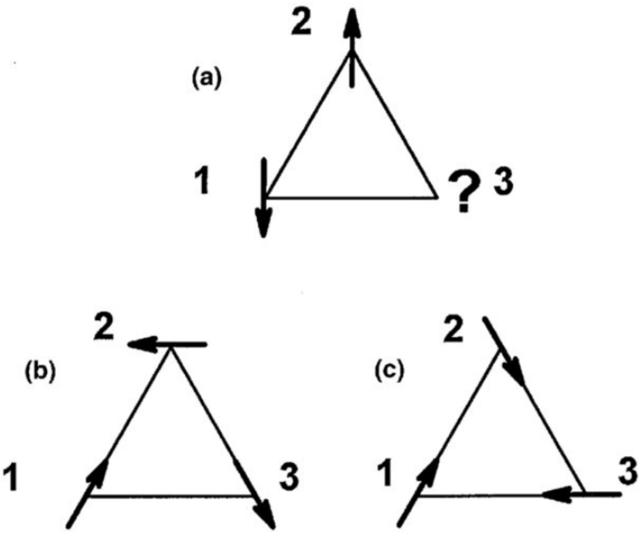

Figure 1.2 Geometric frustration in a triangular antiferromagnet. (a) geometric frustration arising from triangular arrangements of magnetic moments with each pair coupled antiferromagnetically. (b) and (c) two degenerate solutions for the lowest energy of the system for a given spin vector at atom 1. Adapted from [13].

Mn_3AN compounds, where A is an element carrying zero magnetic moment in the compound (such as Ni or Ga), are examples of this non-collinear structure. In these materials, the manganese atoms form a triangular lattice, and due to the crystal's symmetry, spins in Mn_3AN adopt stable configurations like the Γ_{5g} and Γ_{4g} phases [14], see Fig. 1.3. In these states, the magnetic moments are arranged in triangular configurations (see Fig. 1.4), breaking time-reversal, mirror, and rotational symmetries, which enables electronic effects such as the anomalous Hall effect to manifest [15].

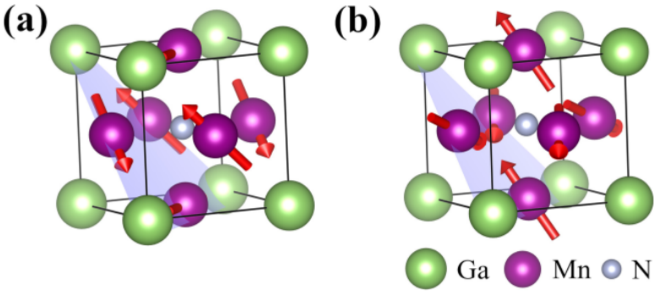

Figure 1.3 Different non-collinear magnetic phases in antiferromagnetic Mn_3AN. (a) Γ_{5g}, (b) Γ_{4g}. Red arrows denote magnetic moments. Adapted from [14].

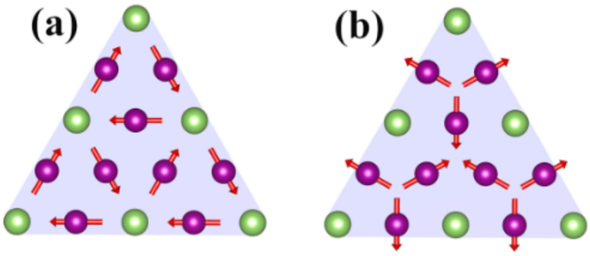

Figure 1.4 (a) Γ_{5g} configuration, (b) Γ_{4g} configuration. Adapted from [14].

Triangular non-collinear antiferromagnets demonstrate across various conditions and are capable of adjusting spin orientations in response to fields or temperature changes while maintaining their triangular structure [4, 5]. These qualities make triangular antiferromagnets particularly promising for spintronic applications, where controlled spin orientations can enable innovative device functionality.

1.4 Altermagnetism

Altermagnetism is a recently identified form of magnetic ordering [2] that introduces a new type of symmetry-driven magnetic structure. In altermagnetic materials, magnetic moments alternate in momentum space, resulting in no net magnetic moment. This ordering arises from crystal symmetries that enable complex spin arrangements within the lattice, making altermagnets distinct from the strict antiparallel alignment of collinear antiferromagnets. Despite the absence of a net magnetic moment, the unique electronic band structure of altermagnets exhibits spin splitting, offering functionalities traditionally associated with ferromagnetic materials [6].

This spin splitting is driven by specific crystal symmetry elements, such as rotations and mirror planes, which dictate the alternating spin polarization in momentum space. As shown in 1.5, these symmetry-protected properties lead to spin splitting in distinct regions of momentum space, determined by the crystal symmetry, including near the Γ-point. Unlike in conventional ferromagnets, where spin splitting results from exchange interactions, altermagnets achieve band splitting purely through crystal symmetry operations. This makes altermagnets unique as materials that are both magnetically ordered and spin-polarized, yet with no net magnetic moment [6].

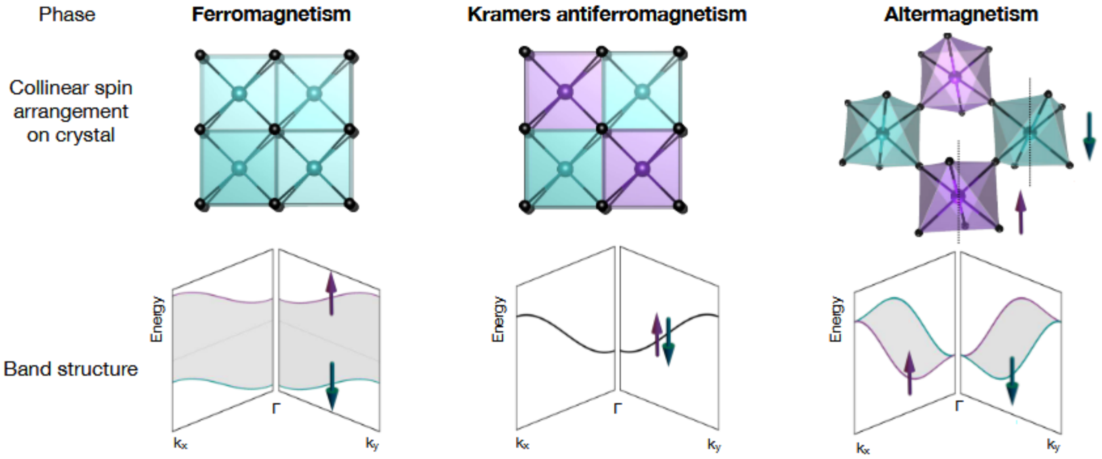

Figure 1.5 **First row:** Illustrative spin arrangements with opposite spin directions represented in purple and cyan. The ferromagnetic and antiferromagnetic crystal structures correspond to FeRh, while the altermagnetic crystal structure corresponds to La_2CuO_4. **Second row:** Schematic band structure showing spin-split bands in ferromagnetic and altermagnetic systems alongside a spin-degenerate antiferromagnetic band. Adapted from [16].

Altermagnets exhibit various types of symmetry-driven ordering around the Γ-point, characterized by the nature of their orbital symmetries. These configurations, d-wave, g-wave, and i-wave, describe how spins are distributed around the Γ-point, reflecting the symmetry characteristics of atomic d, g, and i-orbitals [2]. For instance, MnTe is a g-wave altermagnet, while RuO_2 demonstrates d-wave altermagnetism [6]. This systematic classification highlights the role of crystal symmetry in shaping the electronic band structure and spin distribution in altermagnets.

A key consequence of altermagnetic ordering is its ability to support spin-polarized currents through intrinsic band splitting. This band splitting creates distinct energy levels for spin-up and spin-down electrons along specific crystallographic directions, effectively enabling altermagnets to function as natural spin filters without requiring an applied magnetic field [2]. As illustrated in Fig. 1.5, the symmetry-driven arrangement of spins provides pathways where spin-polarized electrons occupy separate energy states, promoting efficient spin transport within the crystal lattice.

This capability to sustain spin-polarized transport without external fields makes altermagnets highly promising for spintronic applications, particularly those requiring low magnetic noise and energy efficiency. For example, non-volatile memory devices and magnetic sensors benefit from the stable spin configurations intrinsic to altermagnets [6]. Furthermore, their electronic structure supports magneto-transport phenomena such as the anomalous Hall effect [17], anomalous Nernst effect [18], and giant and tunnelling magnetoresistance [19], typically associated with ferromagnetic systems but achieved here without macroscopic magnetization.

2 Studied materials

Due to the similarities in the spintronic phenomena observed in altermagnets and non-collinear antiferromagnets, such as the anomalous Hall effect [20, 14], and anomalous Nernst effect [21, 22], we studied various materials throughout this work. Among the altermagnetic candidates [16] were MnTe samples of differing thicknesses, RuO_2 with two distinct crystallographic orientations, and a series of $Mn_5(Si_xGe_{(1-x)})_3)$ samples spanning from altermagnetic Mn_5Si_3 to fully ferromagnetic Mn_5Ge_3 [23]. Only two non-collinear antiferromagnetic samples were studied: Mn_3GaN and Mn_3NiN.

Preliminary testing using a wide-field Kerr microscope, described in detail in Chapter 4, indicated that only the MnTe and non-collinear antiferromagnetic samples exhibited observable changes during the measurements. Consequently, due to time constraints, these materials were selected for in-depth study, including thermoscanning measurements discussed further in Chapter 3. Hall bar structures were fabricated from one Mn_3GaN sample and one MnTe sample for the purposes of the thermoscanning measurements. Table 2.1 provides a comprehensive list of all samples used, showing their ID, grower, and exact structure.

ID	**Grower**	**Structure**
VA2684	Gunther Springholz (UNI Linz, Linz)	Al_2O_3(10nm)/MnTe(150nm)/SrF_2(111)
VA2684		patterned
VA2685		Al_2O_3(10nm)/MnTe(500nm)/SrF_2(111)
VA1530		MnTe(50nm)/SrF_2(111)/Au(70nm)
VA1532		MnTe(100nm)/SrF_2(111)/Au(70nm)
VA1537		MnTe(150nm)/SrF_2(111)/Au(70nm)
VA1531		MnTe(200nm)/SrF_2(111)/Au(70nm)
197	*****	RuO_2(110)(9nm)/TiO_2
128	*****	RuO_2(001)(9nm)/TiO_2
MnGeSi18	Lisa Michez (CiNAM, Marseille)	$Mn_5(Si_0Ge_{(1-0)})_3)$/Ge(111)
MnGeSi20		$Mn_5(Si_{0.4}Ge_{(1-0.4)})_3)$/Ge(111)
MnGeSi21		$Mn_5(Si_{0.6}Ge_{(1-0.6)})_3)$/Ge(111)
AB22MnSi		$Mn_5(Si_1Ge_{(1-1)})_3)$/Si(111)
MNM22066	Freya Johnson (Cambridge, UK)	Mn_3NiN(13nm)/MgO(100)
21-271	LoMaRe Technologies Ltd	Mn_3GaN(60nm)/MgO/Au(70nm)
21-270		Mn_3GaN(30nm)/MgO, patterned

Table 2.1 List of samples.

2.1 MnTe

Manganese telluride (MnTe) is a semiconductor with antiferromagnetic properties, in which g-wave altermagnetic behaviour was predicted not so long ago [24] and recently also experimentally demonstrated [20, 25]. MnTe can exist in various crystalline phases, each with distinct structural, electronic, and magnetic properties depending on the preparation conditions [26]. The most stable phase at room temperature is α-MnTe, which adopts a nickel arsenide-type crystal structure. Higher preparation temperatures can produce other phases, such as β-MnTe (wurtzite), γ-MnTe (zinc blend), and δ-MnTe (rock salt), each with specific unit cell dimensions and differing behaviours [27].

Phase transitions in MnTe can be thermally induced, allowing shifts between structures with distinct electronic characteristics. For example, β-MnTe is a p-type semiconductor with a direct bandgap greater than 2.4 eV and high resistivity ($>$1000 Ω·cm) [28], making it suitable for optoelectronic detectors [29, 30]. In contrast, α-MnTe, which is an indirect, narrow-bandgap (1.25-1.52 eV) p-type semiconductor with lower resistivity (0.1-1 Ω·cm) [31, 28], is ideal for spintronic applications due to its antiferromagnetic and predicted altermagnetic properties [32, 30].

In α-MnTe, the magnetic moments align within or perpendicular to the hexagonal c-plane, as shown in Fig. 2.1, which is typically parallel to the sample surface. In general, it is energetically more efficient for the arrangement of magnetic moments (or the Néel vector $\vec{L}$) to be in the c-plane. The Néel temperature of α-MnTe thin films is approximately 310 K, with the spin-flop field ranging between 0.5 T and 2 T depending on the specific substrate used [33].

The α-phase of MnTe exhibits predicted altermagnetic behaviour, categorized as g-wave type. This behaviour is characterized by three nodal planes in spin symmetry intersecting at the Γ-point in momentum space, oriented along the crystallographic c-axis, with an additional horizontal nodal plane perpendicular to these three. This symmetry structure allows MnTe to exhibit spin-split electronic bands despite having no net magnetic moment, setting it apart from typical antiferromagnetic materials [2].

Experimental observations have supported this altermagnetic nature. For instance, the anomalous Hall effect, typically seen in ferromagnetic systems, has been detected in MnTe [20], and angle-resolved photoemission spectroscopy (ARPES) measurements reveal spin-splitting in MnTe's electronic band structure, further supporting the altermagnetic model [25].

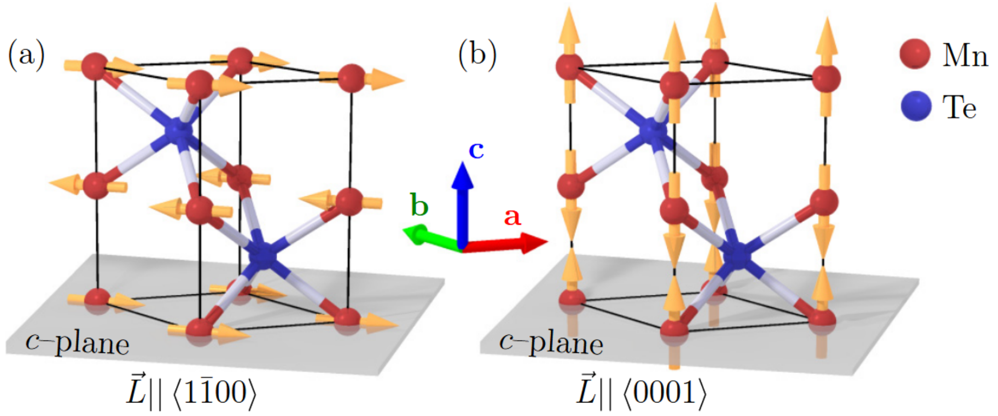

Figure 2.1 Sketch of the atomic and possible magnetic structures of α-MnTe. (a) In-plane/c-plane (ground state) and (b) out-of-plane/c-axis (hard axis) orientation of the magnetic moments of Mn with Néel vector $\vec{L}$ shown. Adapted from [33].

2.2 Mn_3GaN

Manganese gallium nitride (Mn_3GaN) is a metallic antiferromagnetic material with an antiperovskite crystal structure, which has attracted significant interest in the field of spintronics [14]. Antiperovskites are materials with a crystal structure similar to conventional perovskites, see Fig. 2.2, but with an inversion of cation and anion positions. In antiperovskites, typically, a metal occupies the central position in the lattice, surrounded by non-metal ions, creating a highly symmetrical cubic arrangement [34]. This unique structure can stabilize complex magnetic configurations and enables non-collinear antiferromagnetic properties [35, 36].

In Mn_3GaN, the antiperovskite structure allows for specific magnetic configurations that support phenomena like anomalous Hall effect (AHE) and anomalous Nernst effect (ANE) [36]. These magnetic properties are of particular interest in antiferromagnetic spintronics where Mn_3GaN's unique characteristics enable high-speed and low-power operations that would be more challenging to achieve with ferromagnetic materials [37].

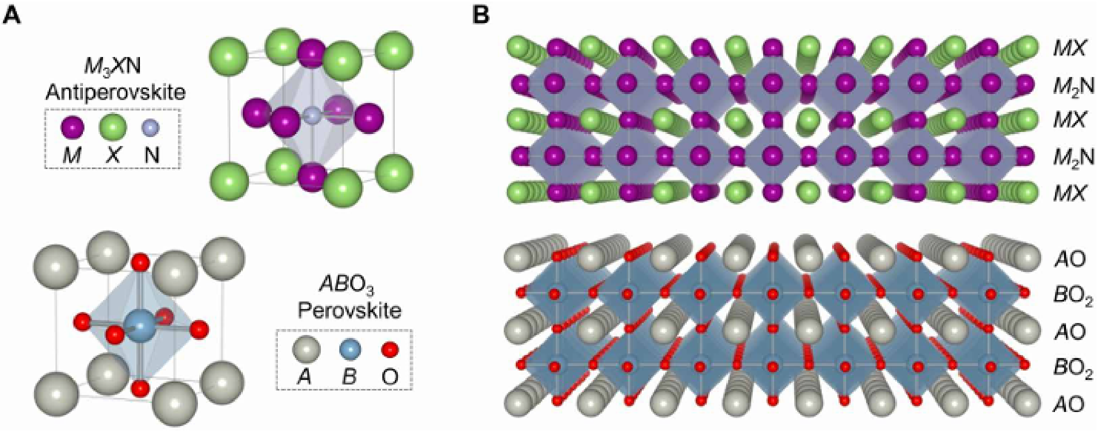

Figure 2.2 Schematic representation of the crystal structures of M_3XN nitride antiperovskite and ABO_3 oxide perovskite compounds and their interfaces. (A) M_3XN and ABO_3 ideal unit cells showing their geometrically analogous crystal structures and reversed anion (N and O) and cation (M and B) positions in the unit cell. (B) M_3XN and ABO_3 slabs represented as a stacking of alternating AO and BO_2 and M_2N and MX planes, respectively. Adapted from [34].

Mn_3GaN's antiperovskite structure places the Mn toms in a Kagome lattice arrangement within the (111) plane [14, 38], which enables distinctive non-collinear antiferromagnetic configurations. The two main magnetic phases of Mn_3GaN relevant to spintronic applications are the Γ_{5g} and Γ_{4g} phases, each characterized by unique spin alignments in the Mn atoms, see Fig. 2.3. The Γ_{5g} phase, which is typically the stable ground state at room temperature, exhibits a 120° triangular spin arrangement in the (111) plane, producing a chiral magnetic structure with no net magnetization and preserving time-reversal symmetry [14].

In contrast, the Γ_{4g} phase can be induced by a 90° rotation of Mn spins within the plane, changing the magnetic symmetry and enabling a finite anomalous Hall effect thanks to the emergent Berry curvature in the band structure [14]. This phase-dependent control over the magnetic and electronic properties of Mn_3GaN offers opportunities for manipulating spintronic responses in devices [14, 36].

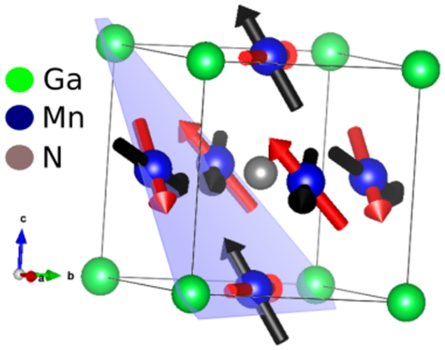

Figure 2.3 In-plane rotation of the magnetic moments of all 3 Mn atoms. The red arrows correspond to the Γ_{5g} configuration, whereas the black ones illustrate the Γ_{4g} configuration. Adapted from [36].

The anomalous Hall effect (AHE) in Mn_3GaN distinguishes it from typical antiferromagnets, where net magnetization is typically absent. In Mn_3GaN, AHE is caused by the Γ_{4g} magnetic phase, where symmetry-breaking within the crystal lattice creates a non-zero Berry curvature in the electronic structure [14]. This symmetry-induced curvature generates an effective internal magnetic field that deflects charge carriers transversely, producing AHE even without conventional magnetization. This property is especially valuable in spintronics, where transverse conductivity can be utilized without needing external magnetic fields [37, 14].

In addition to AHE, Mn_3GaN is predicted to exhibit the anomalous Nernst effect (ANE), which occurs when a temperature gradient across the material generates a transverse electric field. This effect is similarly influenced by the material's unique symmetry and non-collinear magnetic arrangement, particularly in the Γ_{4g} phase. ANE makes Mn_3GaN a candidate for energy-efficient spintronic and thermoelectric application, as it enables heat-to-electricity conversion in devices without requiring magnetic bias [36].

Thin films of Mn_3GaN are often grown epitaxial on MgO substrates, providing lattice compatibility essential for maintaining structural quality and minimizing defects. The MgO substrate supports Mn_3GaN cubic symmetry, which is crucial for retaining the non-collinear antiferromagnetic order in thin films. Controlling the nitrogen concentration during deposition is critical, as slight deviations in stoichiometry can alter magnetic stability and phase purity. Optimized nitrogen levels are especially important for stabilizing the desired Γ_{5g} and Γ_{4g} phases in thin-film applications[37].

Strain introduced by the MgO substrate also plays a role in tuning the Néel temperature (T_N) of Mn_3GaN films. The epitaxial strain has been shown to raise T_N from 290 K in bulk Mn_3GaN all the way up to 380 K in Mn_3GaN/Pt bi-layers [37], enhancing the operational stability of Mn_3GaN-based devices near room temperature. This effect is advantageous for practical applications as it allows Mn_3GaN to be integrated into devices that demand stable magnetic performance at room temperature [37].

3 Thermoelectric and electronic transport

3.1 Electronic and thermoelectric transport phenomena

Magneto-transport effects couple the (internal) magnetic fields with electron momentum. The anomalous Hall effect (AHE) and the anomalous Nernst Effect (ANE) are examples of fundamental transport phenomena in magnetic and thermoelectric materials. These effects arise from intrinsic properties such as Berry curvature in the electronic band structure, directly influencing their transport behaviours. Additionally, other thermo-transport effects can occur, such as the Seebeck effect. Together, these phenomena provide insights into the electronic and magnetic structure of materials and open pathways for spintronic and thermoelectric applications. This section elaborates on the principles of AHE, ANE, and the Seebeck effect, focusing on their interrelations and governing equations.

The AHE is characterised by a transverse voltage V_H that appears perpendicular to an applied current J_x in a magnetic material without needing an external magnetic field, see Fig. 3.1. This phenomenon originates from the Berry curvature, a geometric property of electronic wavefunctions in momentum space, which acts as an effective magnetic field. The Hall conductivity σ_{xy} is given by [39]:

$$\sigma_{xy} = \frac{J_y}{E_x} = \frac{e^2}{\hbar} \int_{BZ} \Omega(\mathbf{k}) f(\mathbf{k}) d\mathbf{k} \tag{3.1}$$

Here, $\Omega(\mathbf{k})$ is the Berry curvature, $f(\mathbf{k})$ is the Fermi-Dirac distribution and e is the electron charge. The integration over the Brillouin zone (BZ) highlights the dependence of AHE on the electronic band structure near the Fermi level. As such, AHE is a vital probe for understanding the topology of electronic bands and magnetisation dynamics [40].

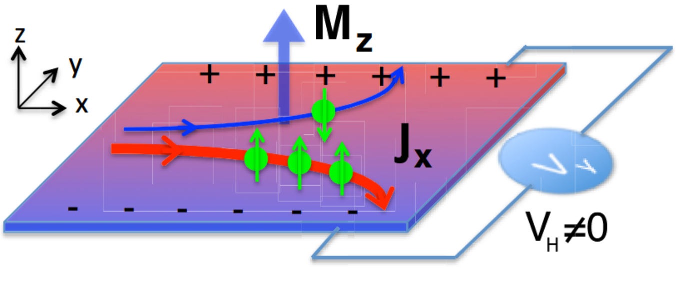

Figure 3.1 Anomalous Hall effect. The electrons with majority and minority spin (due to spontaneous magnetisation M_z) have opposite "anomalous velocity" due to spin-orbit coupling, which causes unbalanced electron concentration at two transversal sides and leads to finite voltage V_H. Adapted from [41].

The ANE is a thermoelectric analogue to the AHE. It occurs when a temperature gradient ∇T generates a transverse voltage V_N perpendicular to both the gradient and the material's magnetic orientation. Like the AHE, the ANE stems from Berry curvature, but its driving force is thermally excited charge carriers. The anomalous Nernst coefficient S_{xy} quantifying this response, is expressed as [42]:

$$S_{xy} = \frac{E_y}{\nabla T} \tag{3.2}$$

where E_y is the transverse component of the electric field.

The relationship between ANE and AHE is formalised through the Mott relation:

$$S_{xy} \approx \frac{\pi^2 k_B^2 T}{3e} \frac{d\sigma_{xy}}{dE}\bigg|_{E=E_F} \tag{3.3}$$

where k_B is the Boltzmann constant, T is the absolute temperature, e is the elementary charge and the derivative of the Hall conductivity σ_{xy} is calculated with respect to the energy E at Fermi level (E_F). This equation connects the anomalous Nernst coefficient to the energy dependence of the Hall conductivity, demonstrating that materials with strong AHE often exhibit significant ANE as well. This intrinsic link provides a unified framework for investigating thermoelectric and spintronic phenomena in magnetic materials. [40].

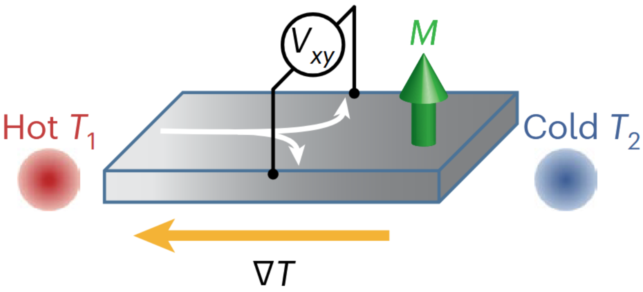

Figure 3.2 Anomalous Nernst effect. Temperature gradient ∇T applied across a material with magnetisation $\mathbf{M}$ induces transverse voltage V_{xy} perpendicular to both the temperature gradient and the magnetisation. Adapted from [43].

The Seebeck effect, though not strictly related to the magnetic order, often accompanies the ANE measurement. It describes the generation of an electric voltage V_S along a material when a temperature gradient ∇T is applied. This phenomenon is characterized by the Seebeck coefficient S_{xx}, which is defined as:

$$S_{xx} = \frac{V_S}{\nabla T} \tag{3.4}$$

The Seebeck coefficient measures a material's ability to convert thermal energy into electrical energy. It depends on factors such as the electronic band structure, carrier concentration, and scattering mechanisms. In magnetic materials, spin-polarised transport can further influence the Seebeck coefficient, adding complexity to the thermoelectric behaviour [42].

3.2 Anomalous Hall and Nernst effects in antiperovskites and altermagnets

The anomalous Hall effect (AHE) in antiferromagnetic materials with non-collinear spin structures is enabled by broken time-reversal symmetry and symmetry-dependent Berry curvature effects. In antiperovskites, such as $\mathrm{Mn_3GaN}$ and $\mathrm{Mn_3NiN}$, the AHE depends heavily on the specific spin configuration of the material. The Γ_{4g} phase (see Fig. 2.3) breaks combined time-reversal and inversion symmetry, allowing Berry curvature to generate a measurable AHE. This configuration features spin arrangements that produce net Berry curvature contributions, resulting in a transverse Hall voltage without net magnetisation. In contrast, the Γ_{5g} phase retains symmetries that cancel Berry curvature contributions, leading to negligible AHE [15].

In $\mathrm{Mn_3NiN}$, the AHE in the Γ_{4g} phase can be modulated by strain, which alters the magnetic and electronic structures to enhance Berry curvature effects. This strain-sensitive behaviour suggests potential applications in piezospintronic devices [15]. Although less explored, $\mathrm{Mn_3GaN}$ exhibits structural and magnetic similarities to $\mathrm{Mn_3NiN}$ implying that it may also show strain-tunable AHE. Such tunability positions Mn-based antiperovskites as promising materials for spintronic applications, where precise control of the AHE is essential [15].

MnTe, as an altermagnetic material, exhibits the AHE due to its symmetry-breaking magnetic structure, which induces Berry curvature without requiring net magnetisation. [44] highlights that variations in AHE signals, driven by the sensitivity of Berry curvature to changes in magnetic phases and domain structures, enable the study of magnetisation dynamics and phase transitions in MnTe. These variations provide a powerful method to track phase transitions under varying external conditions, such as temperature, pressure, or strain.

This property positions MnTe as an effective medium for investigating internal magnetic configurations through its intrinsic AHE, even in the absence of an external magnetic field, supporting applications in spintronics. The AHE response of MnTe offers a pathway to develop devices that rely on stable magnetic phases and efficient magnetic domain control, as indicated by the findings of [44].

The anomalous Nernst effect (ANE), the thermal counterpart to the anomalous Hall effect, is observed in antiperovskites with non-collinear magnetic structures, as demonstrated in studies on $\mathrm{Mn_3NiN}$ [22]. Specifically, the ANE in $\mathrm{Mn_3NiN}$ reaches substantial values when the material is in the Γ_{4g} configuration, which breaks symmetries in a way that allows Berry curvature near the Fermi level to generate a transverse voltage under a thermal gradient. [45] highlights that the ANE is maximised in the Γ_{4g} phase of $\mathrm{Mn_3NiN}$, where the configuration facilitates Berry curvature effects, contrasting with the Γ_{5g} phase, where mirror symmetries cancel the Berry curvature contributions, yielding a negligible ANE.

[22] further confirms the thermoelectric potential of $\mathrm{Mn_3NiN}$, emphasising that the ANE can be modulated by tuning the magnetic structure (for example, by strain, temperature or pressure), which in turn adjusts Berry curvature near the Fermi energy. This sensitivity supports the ANE's use as a probe for magnetic and electronic structure near the Fermi level, making $\mathrm{Mn_3NiN}$ highly promising for applications in spin caloritronics.

While $\mathrm{Mn_3GaN}$ has not been as extensively studied, [45] suggests that other

Mn-based antiperovskites with similar non-collinear antiferromagnetic structures may exhibit large ANE values due to analogous Berry curvature mechanisms. This implies that Mn_3GaN could potentially support a significant ANE, as seen in Mn_3NiN, offering a mechanism for thermal-to-electric conversion suitable for energy-efficient thermoelectric applications.

3.3 Thermoscanning microscopy

Thermoscanning microscopy, or Scanning thermal gradient microscopy [5], is an imaging technique that utilises the anomalous Nernst effect (ANE) to explore the magnetic domain structures of antiferromagnetic and altermagnetic materials. It works by inducing a local thermal gradient across the sample surface, typically achieved by scanning a focused laser over the sample. The out-of-plane temperature gradient generated by the laser spot interacts with the material's in-plane magnetic structure, causing a transverse voltage due to the ANE, which can then be measured to map the magnetic domains.

[5] demonstrated the effectiveness of this method in imaging non-collinear antiferromagnetic domains in Mn_3Sn, see Fig. 3.3. By moving the laser across the sample surface, they induced localised thermal gradients that resulted in a voltage response along the y-direction corresponding to signals generated in different magnetic domains, which are detectable through changes in the ANE. This technique allows for high-resolution imaging of domain configurations, particularly useful in materials where conventional imaging techniques, such as magneto-optical Kerr effect (MOKE), are limited by surface sensitivity.

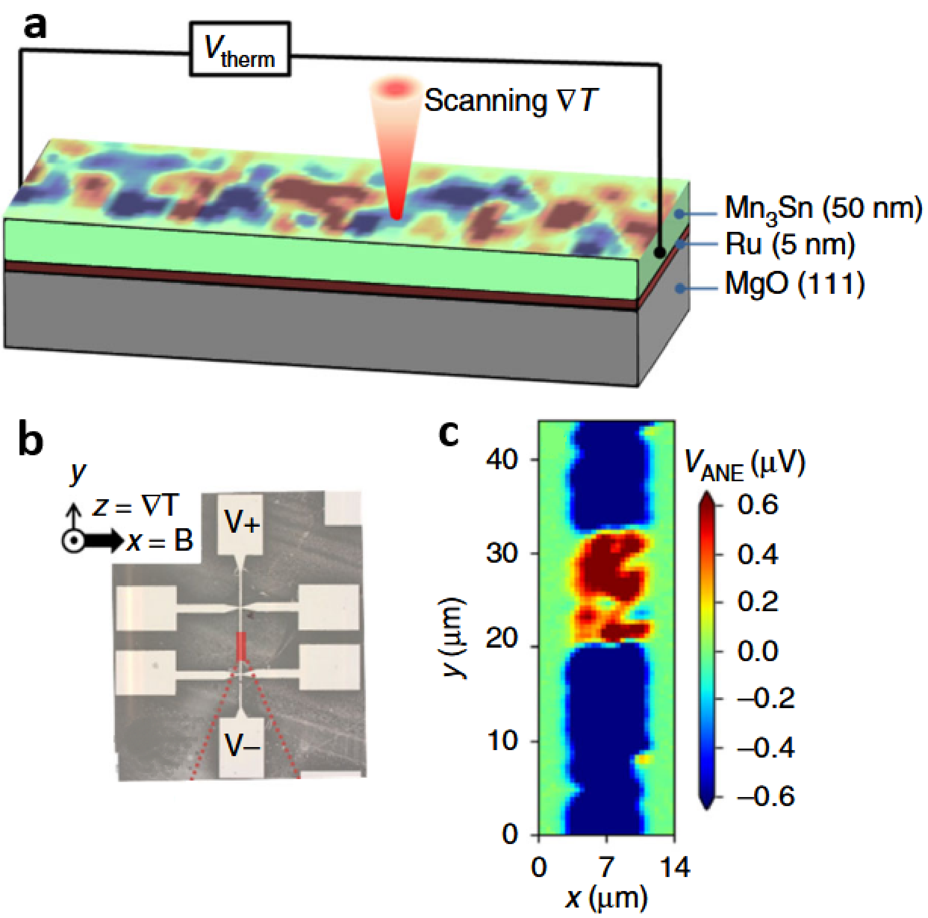

Figure 3.3 **a** Schematics of thermoscanning microscopy on Mn_3Sn. The laser beam is scanned over the sample surface, and the resulting local thermovoltage sign and magnitude reflect the local magnetic properties. **b** Microscope image of a typical device and the experimental geometry. **c** Image of the spatially resolved thermovoltage recorded in the sample. Adapted from [5].

In [4], thermoscanning microscopy was applied to study antiferromagnetic domain orientations in Mn_3NiN. Using a scanning laser to generate out-of-plane thermal gradients, the study demonstrated how the ANE can reveal detailed information on domain structures in materials with complex magnetic ordering. The technique's sensitivity to local magnetic orientation provides valuable insights into domain clustering and the intricate nature of magnetic configurations, further solidifying its utility for advanced magnetic studies.

In Mn_3NiN and Mn_3Sn, both non-collinear antiferromagnets, thermoscanning microscopy proved capable of distinguishing magnetic domains with high spatial resolution, directly linking thermal gradient-induced voltage responses to domain configurations. [5] highlighted how the ANE response varies with different domain orientations in Mn_3Sn, creating distinct voltage contrasts that correlate with magnetic domain boundaries. This domain sensitivity enables researchers to map the arrangement of domains, offering a clearer view of domain wall characteristics and magnetic phase stability.

[4] extended the application of thermoscanning microscopy to Mn_3NiN, utilising it to identify the antiferromagnetic domain orientations within the material.

Beyond imaging, thermoscanning microscopy can facilitate heat-assisted writing, a process where thermal gradients are used not only for observation but also to modify magnetic domains intentionally. [5] demonstrated this principle in Mn_3Sn by using a laser-induced thermal gradient combined with an external magnetic field to manipulate domain patterns. This technique leverages the ANE and localised heating to selectively create or erase magnetic domains, providing a means of writing domain structures with spatial precision. Specific domain configurations can be induced and stabilised by controlling the laser position and the applied magnetic field, supporting applications in magnetic memory and domain-based data storage.

3.4 Experimental setup

The thermoscanning experiment was conducted in the Laboratory of OptoSpintronics (LOS) at the Department of Chemical Physics and Optics. For the measurements, two Hall bar samples were prepared: one based on MnTe (VA2684) and another on Mn_3GaN (21-270), as listed in Table 2.1. Antonín Baďura patterned the MnTe sample, while the Mn_3NiN sample was provided by Zbyněk Šobáň, both from the Institute of Physics of the Czech Academy of Sciences.

For the MnTe sample, a 5 μm-wide Hall bar was patterned using optical lithography and plasma etching (Ar + O_2 + SF_6). A gold layer was deposited onto the sample to facilitate bonding, with the excess gold removed through lift-off. This gold layer was particularly important due to challenges in bonding directly to the MnTe layer grown on SrF_2. The mismatch between the MnTe and SrF_2 lattice often caused the MnTe layer to tear away during bonding attempts, making the gold layer essential for reliable contact.

In the case of Mn_3GaN, a 2 μm-wide Hall bar was patterned using electron-beam lithography and ferric chloride ($FeCl_3$) etching. The contacts were created via the lift-off method, where the desired contact areas were first defined lithographically, followed by the deposition of a Cr/Au metallisation layer with thicknesses of 5 nm and 80 nm, respectively. A total of six Hall bars were created on this sample, but only one of them (#1_A) fully bonded. An image of the Mn_3GaN Hall bar, taken using a scanning electron microscope (SEM), is shown in Fig. 3.4, with additional details available in Fig. 3.5.

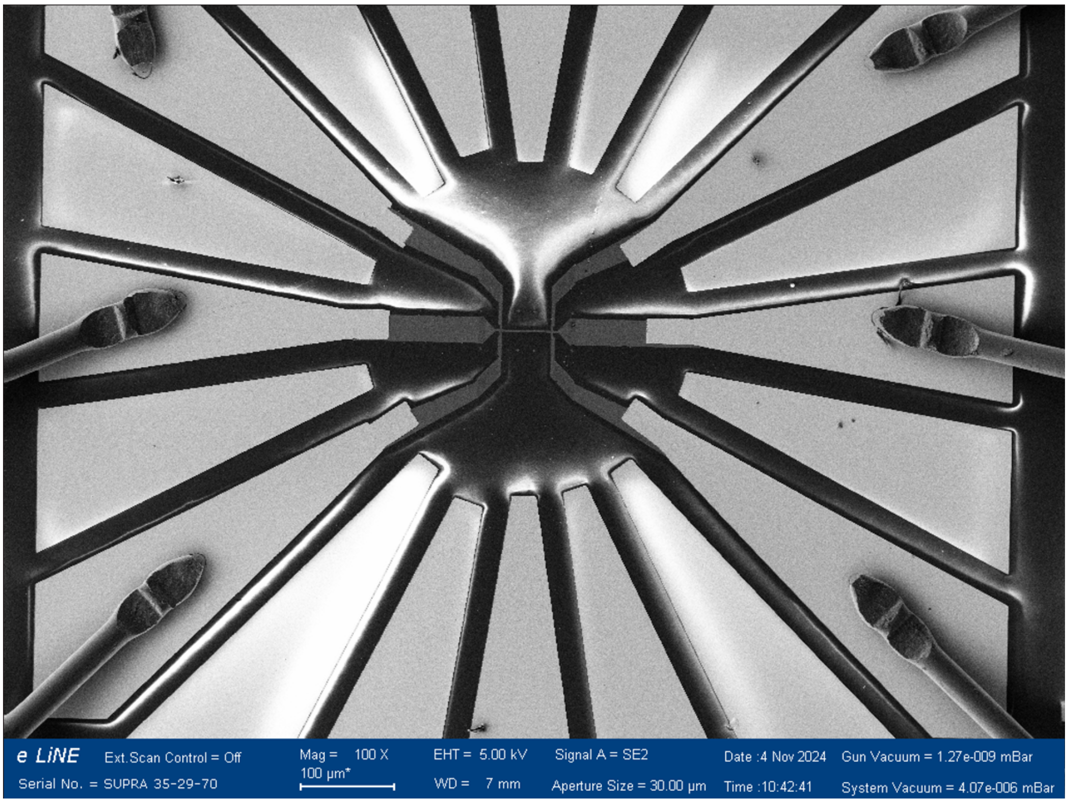

Figure 3.4 Scanning electron microscopy (SEM) image of the Mn_3GaN device (21-270_#1_A). Image taken by Zbyněk Šobáň.

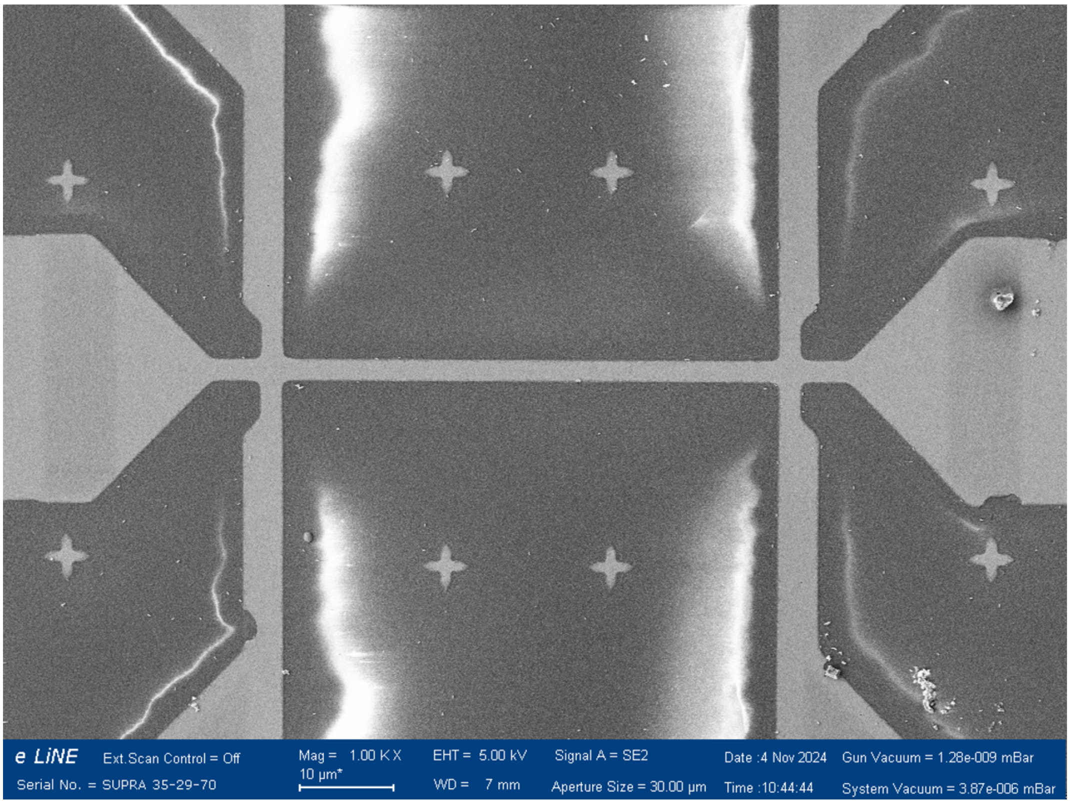

Figure 3.5 Scanning electron microscopy (SEM) image of the Mn_3GaN Hall bar (21-270_#1_A). Image taken by Zbyněk Šobáň.

The thermoscanning experiment utilised a femtosecond titan-sapphire oscillator (MaiTai, Spectra Physics) coupled with an optical parametric oscillator (OPO) (Inspire, Radiantis) to generate the desired wavelength for the setup tuneable in spectral range 345-2500 nm. To modulate the laser beam amplitude for phase-locked detection of thermo-voltage, an optical chopper was introduced, operating at a frequency slightly below 1.2 kHz to maintain consistent modulation throughout the experiment. The laser beam was refined using a lens to align its focal point with that of the LED illumination. This alignment was crucial due to the differing beam profiles of the two sources: the laser beam has a Gaussian profile, while the LED, enhanced by Köhler illumination, produces a highly uniform beam. These differences in beam characteristics required precise adjustment to minimize focal point discrepancies. A dichroic mirror, beam splitter, and a 20× Mitutoyo Plan Apo Infinity Corrected Long WD Objective were employed to merge and align the laser and LED paths effectively.

The LED provided a wide-field image of the sample, allowing precise identification of the illuminated area, while the laser generated the temperature gradient at a focused point on the sample. A CCD camera (Allied Vision, Prosilica GX 1050) was integrated into the setup for imaging purposes, and a reflectivity detector was included to confirm whether the laser was accurately illuminating the sample. The Hall bar's higher reflectivity compared to the substrate served as a reliable indicator of the laser being focused on the Hall bar.

The optical system, depicted in Fig. 3.6, focused the laser to spot sizes ranging from 1.5 μm to 1.8 μm. During the imaging process, the laser spot was scanned across the device using a 3D piezo-positioner (Micronix XY-stage (ES-50PM, PPS-20), New Focus Picomotor (Z-stage)), forming an x-y grid with step sizes between 0.2 μm and 1 μm. An electromagnet capable of generating fields from -0.5 T to 0.5 T was used to apply in-plane magnetic fields during the experiment.

A closed-cycle GM-based cryostat (Advanced Research Systems) equipped with a low-vibration interface was integrated into the setup to enable measurements across a range of temperatures, both above and below the Néel temperatures of the studied materials. This system ensured precise temperature control, allowing for a detailed investigation of the material's magnetic properties under varying thermal conditions.

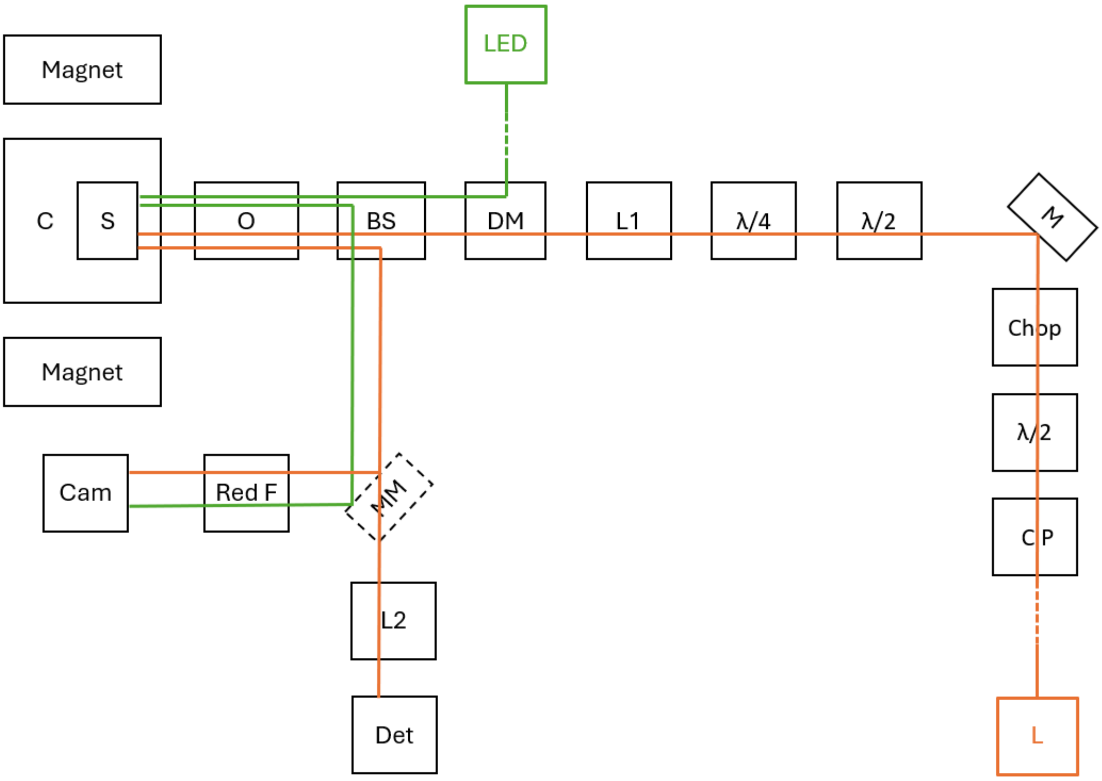

Figure 3.6 Schemetics of the optical part of the thermoscanning setup. Laser source (L), cube polariser (CP), $\lambda/2$ waveplate ($\lambda/2$), optical chopper (Chop), mirror (M), $\lambda/4$ waveplate ($\lambda/4$), -4 D refracting lens (L1), dichroic mirror (DM), beam splitter (BM), objective (O), sample (S), cryostat (C), removable magnetic mirror (MM), spectral high-pass filter (Thorlabs, BG37) (Red F), camera (Cam), 20 D focusing lens (L2), detector (Det).

The electronic part of the setup for the thermoscanning measurement is schematically represented in Fig. 3.7. Three Stanford Research Systems SR830 DSP Lock-In Amplifiers, synchronised with the optical chopper frequency, were utilised to detect the thermally generated signals and sample reflectivity. One amplifier measured the longitudinal voltage ($V_{[010]}$) of the sample, while another recorded the transverse voltage ($V_{[100]}$). The third amplifier monitored the reflectivity of the sample via photovoltage generated by the Si detector.

To enhance the detected signals before processing, Stanford Research Systems SR560 Low-Noise Preamplifiers were integrated into the setup. These preamplifiers were used to amplify the voltage signals, while a custom-made preamplifier was employed to boost the voltage signal from the reflectivity detector, ensuring accurate detection and analysis. Custom LabVIEW software, developed by David Schmoranzer from the Department of Low-Temperature Physics, enabled real-time signal acquisition from the lock-in amplifiers. Additionally, this software controlled the 3D piezo-positioner, allowing for automated scanning across the sample.

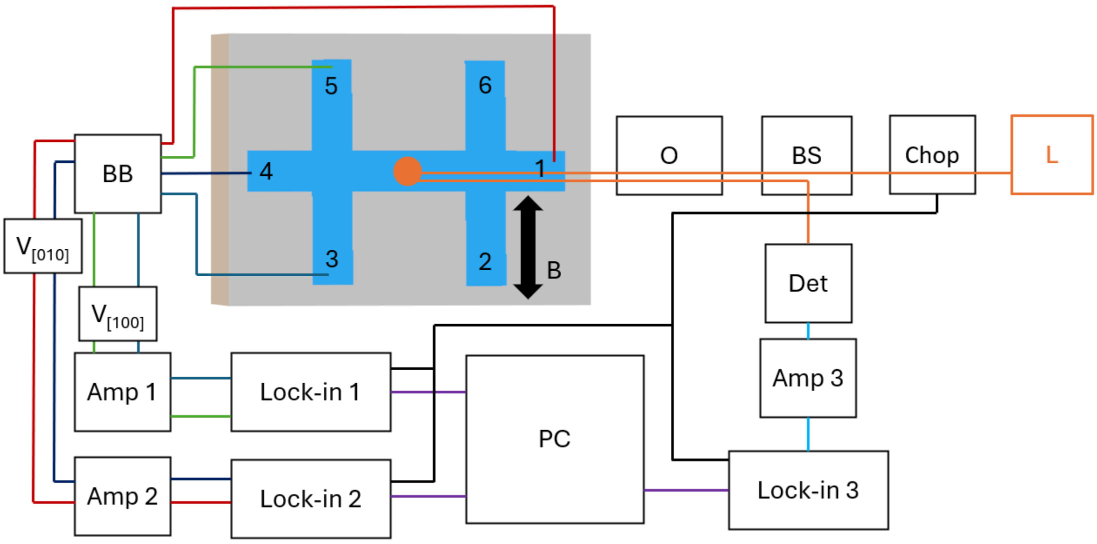

Figure 3.7 Schemetics of the electronic part of the thermoscanning setup. Laser source (L), optical chopper (Chop), beam splitter (BM), objective (O), detector (Det), breakout box (BB), preamplifiers (Amp 1, Amp 2 - SRS SR560; Amp 3 - custom-made). Lock-in 1 was used to detect the transverse voltage ($V_{[100]}$), lock-in 2 was used to detect the longitudinal voltage ($V_{[010]}$) and lock-in 3 was used to detect the reflectivity. The black arrow shows the possible directions of the applied magnetic field **B**.

In addition to the thermoscanning measurements, the temperature dependence of resistivity (ρ) was measured using the setup illustrated in [46]. Due to the absence of a dedicated current source, an AC voltage function generator (RIGOL DG1022Z), generating a -10 mV to 10 mV peak-to-peak sinusoidal signal at 13 Hz, was utilised for the measurement. Lock-in amplifiers were used to detect the resulting voltages. To determine the current through the Hall bar, lock-in 2 was used in conjunction with a known resistor (50 Ω), applying Ohm's law:

$$I = \frac{U}{R} \tag{3.5}$$

Lock-in 1 was configured to measure the resistance of the Hall bar as part of a four-terminal resistance measurement. Using the known dimensions of the sample, the resistivity (ρ) can be calculated from the resistance R using the following relation:

$$\rho = R\frac{A}{l} \tag{3.6}$$

Here, A represents the cross-sectional area of the sample, and l is its length.

3.5 Experimental results

This section discusses the experimental results obtained from the thermoscanning measurements. Patterned samples were essential for detecting the thermally generated voltage, and only two samples were patterned: a 5 μm-wide Hall bar of MnTe (VA2684) and a 2 μm-wide Hall bar of Mn_3GaN (21-270). Among these, only one Hall bar on each sample was successfully bonded, limiting the scope of the experiment to these two bonded samples. Additional details about these samples are provided in Table 2.1. The experimental approach was inspired by methods described in [4] and [5], where similar techniques were applied to comparable materials. Accordingly, the procedures used here closely followed the practices outlined in these studies.

The primary objective of this experiment was to image magnetic domains in the MnTe and Mn_3GaN samples. Various experimental conditions were tested to examine their influence on the formation and behaviour of magnetic domains. Measurements were conducted at different temperatures, both above and below the Néel temperature of the particular material, with and without an applied in-plane magnetic field. The magnetic field was tested in two opposing directions to observe any directional dependence. Additionally, the effect of cooling the samples in the presence of an in-plane magnetic field was investigated. Finally, heat-assisted writing [5, 4] test was planned near the Néel temperature to explore its impact on domain formation and manipulation.

3.5.1 Thermoscanning of MnTe

As discussed in the previous section, bonding the MnTe Hall bar posed significant challenges. Despite attempts to bond two different Hall bars on the MnTe sample, only four contacts on the first Hall bar and one contact on the second Hall bar remained intact at the start of the measurements. The resistance between the surviving contacts was checked to confirm no further damage had occurred. A schematic of the remaining bonds is provided in Fig. 3.8. Due to these limitations, the measurements were restricted to the transverse voltage between contacts 2-6 ($V_{[100]}$) and 3-4 ($V_{[110]}$).

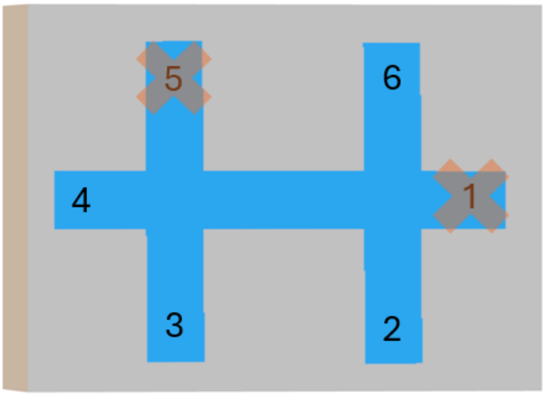

Figure 3.8 Schemetics of the surviving bonds on the MnTe (VA2684) sample.

The lock-in amplifier used in the experiment decomposes the detected signal into four primary components: X, Y, R, and θ. Each component offers specific insights into the signal. The X-component represents the in-phase portion relative to the reference signal, proportional to the signal amplitude and the cosine of the phase difference (ϕ) between the input and reference. Conversely, the Y-component captures the quadrature signal, shifted by 90° relative to the reference, and corresponds to the signal amplitude multiplied by the sine of the phase difference. Together, X and Y form the Cartesian representation of the detected signal.

The total magnitude of the signal, R, reflects the overall signal strength independent of phase, calculated as $R = \sqrt{X^2 + Y^2}$. The phase difference, θ, provides additional context about the relationship between the input and reference signals, expressed as $\theta = \arctan \frac{Y}{X}$. This signal decomposition enables the lock-in amplifier to deliver detailed amplitude and phase information, which is critical for extracting coherent signals in noisy environments. Depending on the experimental objectives, specific parameters (X, Y, R, or θ) are analysed to obtain amplitude, phase-sensitive information, or both.

Measurements of the MnTe sample were conducted after cooling to 20 K, with the scanning laser set to a power of 4 mW. Figure 3.9 shows the measured quantities, illustrating the signal components captured during the experiment.

The *tricontourf* function from the *matplotlib* library was employed to visualise the spatial distribution of thermovoltage data. This function creates filled contour plots by first constructing a triangulation of the x- and y-coordinates from the measurement points, generating a mesh of non-overlapping triangles to represent the spatial layout. Thermovoltage values are interpolated across this triangulation, allowing *tricontourf* to produce smooth and continuous contour levels, each depicted with distinct colours. This approach effectively highlights spatial variations in thermovoltage, providing a clear and intuitive visualisation of the thermovoltage gradients, even when the raw data points are unevenly distributed.

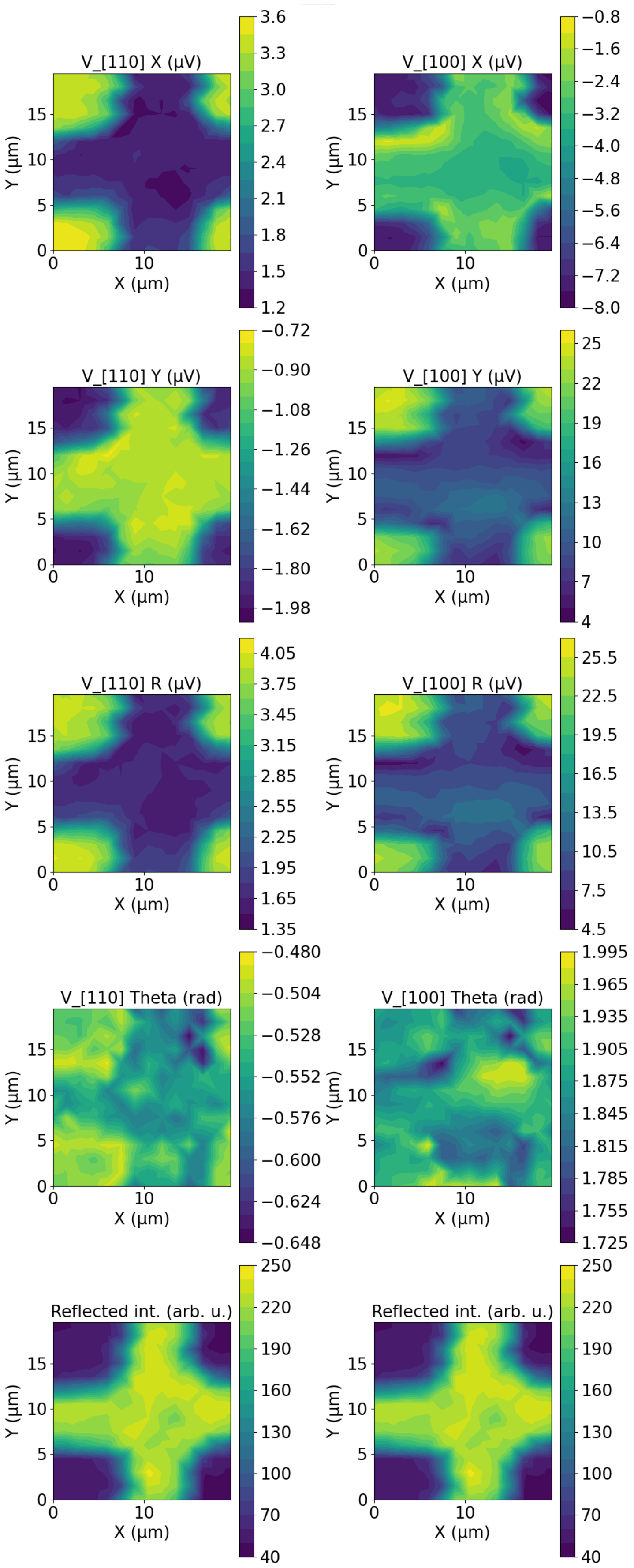

Figure 3.9 $V_{[100]}$ (first column) and $V_{[110]}$ (second column) signal measured in the MnTe sample after cooling down to 20 K with no applied magnetic field and a laser power of 4 mW.

In Fig. 3.9, we show the experimental data. The signal detected when the light was focused on the SrF_2 substrate was unexpectedly larger than that from the MnTe sample. This result was surprising, as the voltage generated by the anomalous Nernst effect (ANE) should only originate from a magnetic material, while SrF_2, being non-magnetic, should not contribute to this effect. Since no magnetic field was applied during the measurement, the ordinary Nernst effect was also ruled out as the source of the detected signal.

A possible explanation is that a strong Seebeck effect from the SrF_2 substrate dominated the measured signal, overshadowing the ANE contribution from the thin MnTe layer. This hypothesis aligns with the observation that the signal decreased at the Hall bar crossing, where the MnTe layer covered the substrate, reducing the substrate's direct contribution. The $V_{[100]}$ signal was larger than $V_{[110]}$, which was expected, as the 2-6 cross of the Hall bar (Fig. 3.8) was directly illuminated, generating an in-plane temperature gradient closer to the contacts detecting $V_{[100]}$. When the laser spot was moved to the centre of the Hall bar or to the 3-4 cross, where $V_{[110]}$ was measured, the signal size varied noticeably depending on the distance between the laser spot and the voltage-detecting contacts.

Given that MnTe has an indirect bandgap at 1.46 eV ($\approx$ 850 nm) [47], measurements were repeated using a wavelength of 870 nm in addition to the original 820 nm, which was optimized for the setup. No significant difference in the detected signals was observed within the margin of error.

Subsequent inspection revealed that all remaining bonds on the MnTe sample had been severed, likely during the cooldown to 20 K. This issue rendered all measurements on MnTe unreliable, as the exact connections of the bonds during the experiment could not be verified. Without confirmation of the proper electrical connections, the detected signals could not be attributed with certainty to the MnTe Hall bar. As a result, further measurements on MnTe were postponed until a more robust and consistent bonding method is developed. Unfortunately, this issue could not be resolved in time to repeat the measurements for this thesis. However, thermoscanning of MnTe remains a priority for future work.

3.5.2 Resistivity measurement of Mn_3GaN

Unlike the challenges faced with the MnTe sample, no issues were encountered with the bonding of the Mn_3GaN Hall bar. To verify the integrity of the bonds and electrical connections, resistance measurements were performed across all possible contact combinations on the Hall bar, as detailed in Table 3.1. Additionally, the temperature dependence of resistivity ρ was measured to investigate its behaviour, motivated by the non-trivial results reported in [37].

Contact 1	**Contact 1**	**R [kΩ]**
1	2	4.8
1	3	11.4
1	4	8.2
1	5	9.6
1	6	5.5
2	3	11.4
2	4	9.7
2	5	11.2
2	6	6.3
3	4	6.3
3	5	6.5
3	6	13.4
4	5	4.7
4	6	10.4
5	6	11.8

Table 3.1 Resistance measured between contacts on the Mn_3GaN Hall bar.

The Mn_3GaN sample was cooled to 30 K in a cryostat, followed by a single heating and cooling cycle. The sample was heated at a rate of 5 K/min and cooled at 3 K/min. Resistivity was calculated using the four-terminal resistance method and Eq. 3.6, with the Hall bar dimensions specified by the lithographic design (2 μm wide, 50 μm long) and the thickness of the sample provided by the grower (30 nm). The results, displayed in 3.10, show a noticeable shift between the heating and cooling curves attributed to the differing rates of temperature change.

Resistivity (R) was also estimated as a sanity check using the source voltage (V_S) divided by $\sqrt{2}$ to account for the peak-to-peak setting of the AC source (10 mV at a frequency of 13 Hz) while the lock-in measures root mean square (RMS). The calculation used the resistance of a known resistor ($R_1 = 50\Omega$) and the voltage measured on lock-in 2 (V_2), as follows:

$$R = \frac{R_1(V_S/\sqrt{2} - V_2)}{V_2} \tag{3.7}$$

The resistivity values obtained through this method differed by only 1 % from those calculated using the four-terminal method, supporting the validity of the measurements.

However, there was a 2-3× discrepancy between the resistivity values measured here and those reported in [37]. This discrepancy is likely due to differences in sample thickness. Transmission spectra from [48] for a series of Mn_3GaN samples, including the 21-270 sample used here, suggest that the actual thickness of this sample may be less than the specified 30 nm.

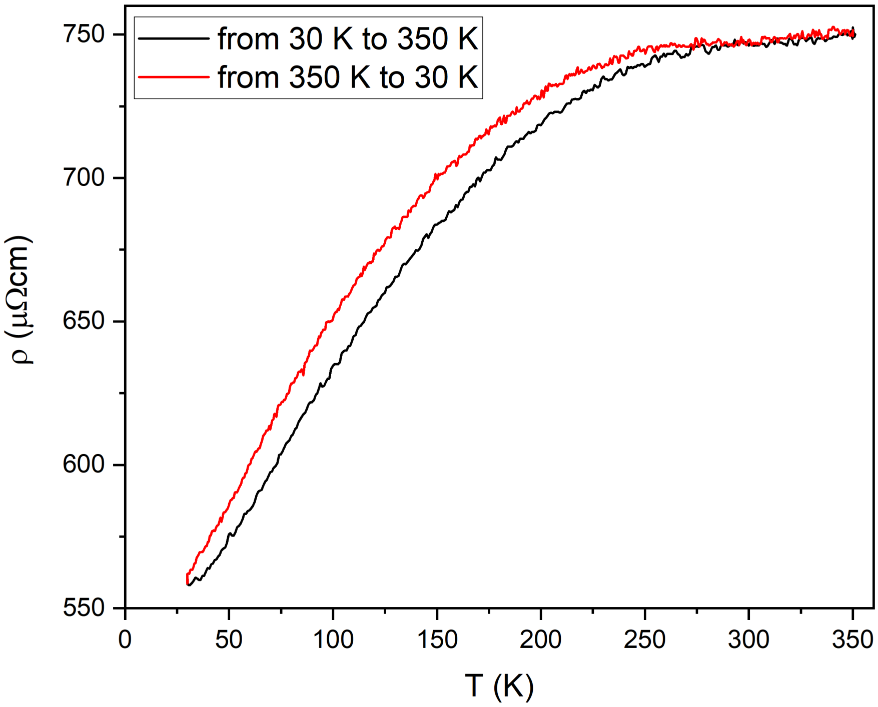

Figure 3.10 Measured temperature dependence of resistivity (ρ) of the Mn_3GaN Hall bar. The black and red lines show the difference between heating and cooling the sample. An AC voltage source with a peak-to-peak amplitude of 10 mV and a frequency of 13 Hz was applied to the sample.

The derivative of resistivity with respect to temperature ($\frac{d\rho}{dt}$) was also calculated and is shown in Fig. 3.11. Following the method in [37], peaks and discontinuities in $\frac{d\rho}{dt}$ were used to estimate the Néel temperature (T_N) and Curie temperature (T_C). These anomalies correspond to changes in magnetic ordering, which influence electron scattering. From the data, the Néel temperature is estimated at $T_N \approx$ 290 K, slightly lower than the reported value for bulk Mn_3GaN [49]. A local maximum around 75 K can correspond to the Curie temperature (T_C), attributed to the coexistence of the Γ_{5g} phase with a ferrimagnetic-like M-1 phase of tetragonal symmetry and non-planar magnetic order [50].

The M-1 phase of Mn_3GaN is particularly intriguing due to its recent identification as a potential candidate for p-wave magnetic order [51].

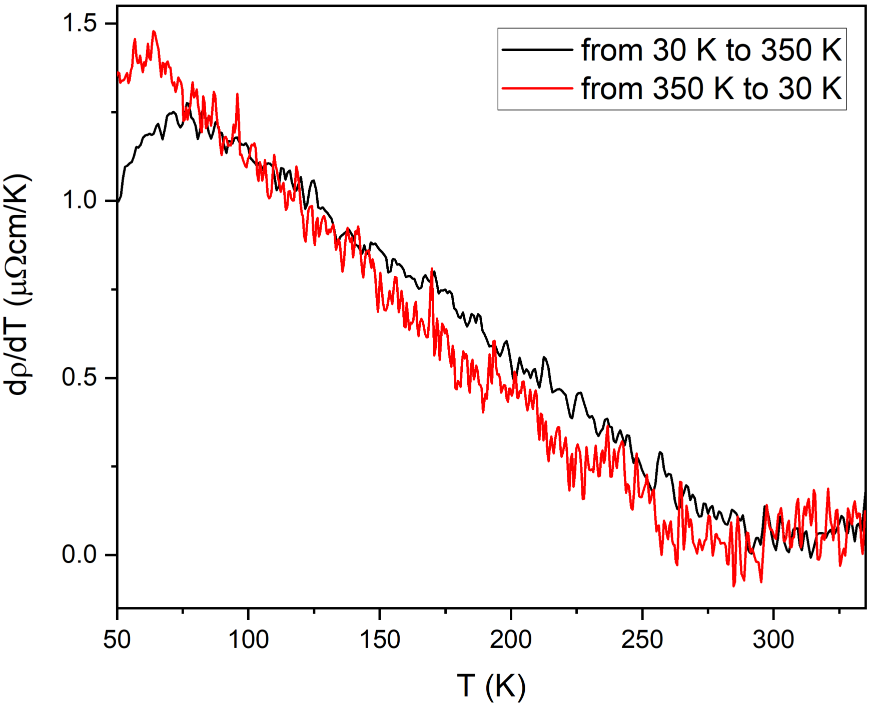

Figure 3.11 Calculated derivative of resistivity with respect to temperature $\frac{d\rho}{dt}$ of the Mn_3GaN Hall bar. Smoothing was performed using 40-point adjacent averaging to improve clarity. The black and red lines show the difference between heating and cooling the sample.

3.5.3 Thermoscanning of $\mathrm{Mn_3GaN}$

The thermoscanning measurements on the $\mathrm{Mn_3GaN}$ sample were conducted under various conditions, including different temperatures, magnetic fields, laser intensities, and polarisations. Heat-assisted writing was also attempted. The results and analysis of these experiments are presented in this section. Figure 3.12 shows how the $\mathrm{Mn_3GaN}$ sample appears on the camera.

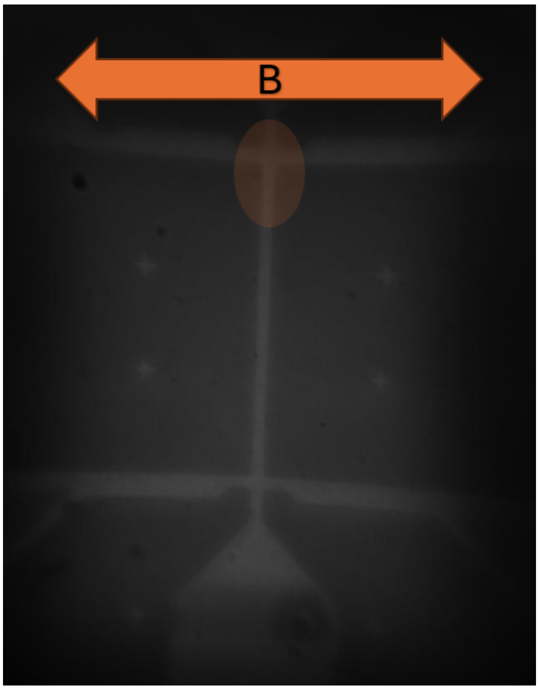

Figure 3.12 $\mathrm{Mn_3GaN}$ sample depicted by the camera. The orange arrow shows the possible directions of the in-plane magnetic field, and the ellipsis highlights the measured area around the cross. Width of the Hall bar is 2 μm.

As with the MnTe measurements, the full dataset from the lock-in amplifiers (X, Y, R, and θ) was initially analysed. However, for clarity and to avoid redundancy, only the X-component data is shown, as it provides sufficient information for comparisons across different conditions. Reflectivity measurements are also included to indicate the laser spot's position relative to the Hall bar.

The initial measurements focused on the Hall bar cross after cooling the sample from room temperature ($\approx$ 296 K) to 20 K. The effect of an applied in-plane magnetic field ($\pm$ 500 mT) was tested in the x-direction. As shown in Fig.3.13, no reversal in the detected voltage was observed with the applied magnetic field. The expected $V_{[100]}$ signal was detected only at the cross, where the sensing bonds are connected, and remained close to zero when the laser spot was located elsewhere on the Hall bar. The signal at the middle of the cross was slightly smaller than its surroundings. As the $V_{[100]}$ signal provided no additional information outside the cross, it is omitted in subsequent discussions of Hall bar measurements. For $V_{[010]}$, the signal was near zero away from the Hall bar, with one notable point within the Hall bar where the signal was approximately twice as large as the surrounding values. This signal also showed no significant change with the magnetic field.

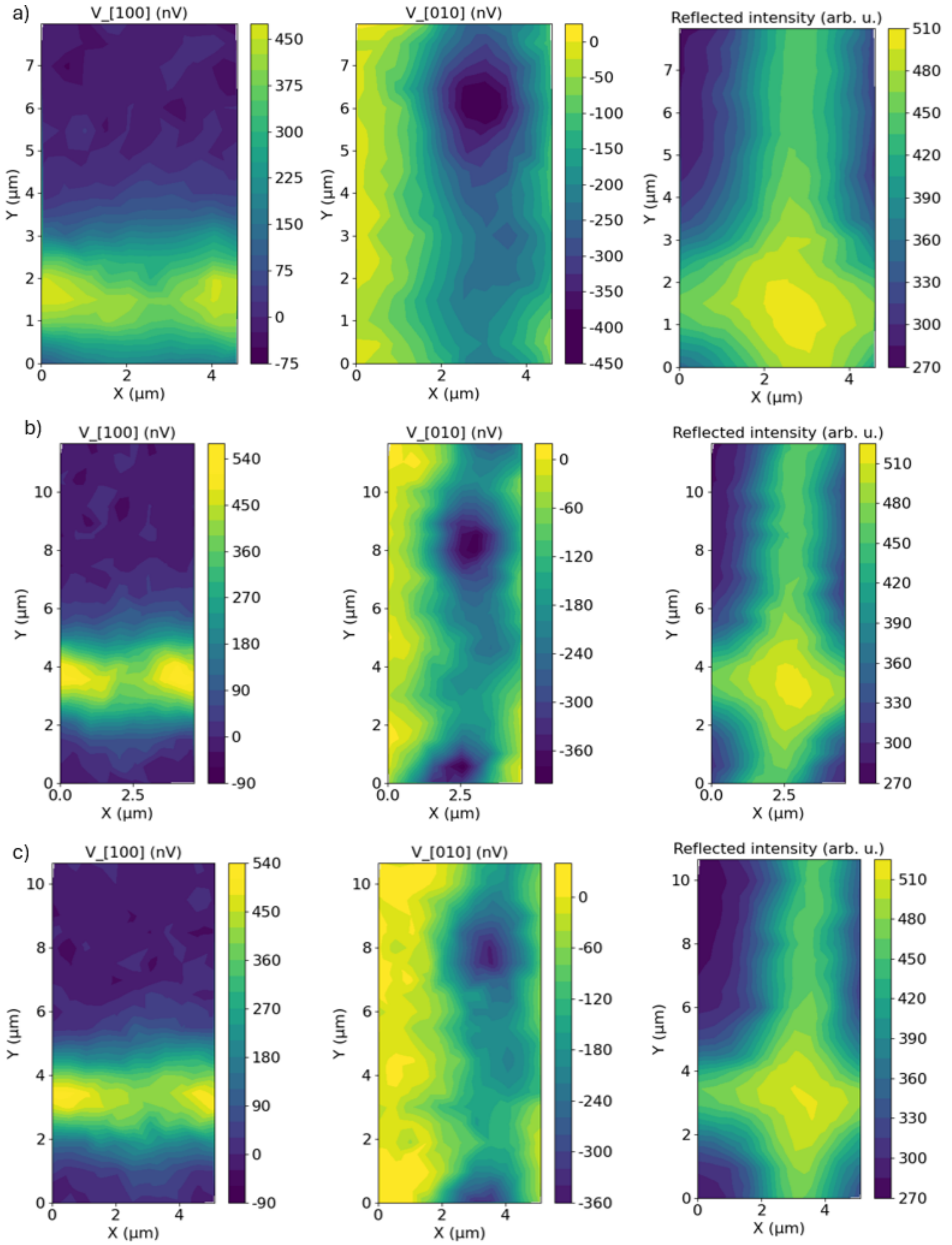

Figure 3.13 Thermovoltage $V_{[100]}$ and $V_{[010]}$ measured in Mn_3GaN Hall bar at 20 K under different applied in plane (x-direction) magnetic fields and the reflected intensity of the area of the device scanned. a) -500 mT, b) 0 mT, c) 500 mT. The laser power was 8 mW.

The sample was subsequently tested at 20 K, 80 K, 140 K, 296 K (room temperature), and 340 K (above the Néel temperature). At each temperature, the effect of an applied magnetic field (± 500 mT) was again tested, but no significant differences were observed. Figure 3.14 shows the $V_{[010]}$, signal measured on the Hall bar approximately 10 μm away from the cross. The $V_{[100]}$ values were negligible and were not included. The $V_{[010]}$ signal decreased with increasing temperature, with a sign change occurring between 140 K and room temperature. The data suggests this transition is closer to 140 K, as the signal magnitude was smaller there than at 296 K.

Significant challenges were encountered with sample stability during these measurements, particularly at temperatures other than the cryostat base temperature of 20 K, where the heater was not employed. The cryostat caused the sample to drift up to 15 μm from its original position within one measurement ($\approx$10-15 min), with greater instability at higher temperatures. Additionally, the cryostat chiller introduced periodic vertical vibrations of 1-2 μm at a frequency of approximately 2 Hz, further impacting measurement precision. At 20 K, distinct areas on the Hall bar produced the majority of the signal, while the signal elsewhere was negligible. However, at higher temperatures, this instability likely blurred the signal, making clear observations difficult.

Further tests included cooling the sample from 340 K to 20 K in the presence of an in-plane magnetic field (± 500 mT) and without any applied field. No noticeable differences were observed between these conditions. The data presented here corresponds to the measurements taken after cooling without a magnetic field, as these provided the most stable and consistent results. Due to the stability issues at temperatures other than 20 K, subsequent measurements were limited to 20 K and room temperature (296 K), where the use of the cryostat could be avoided.

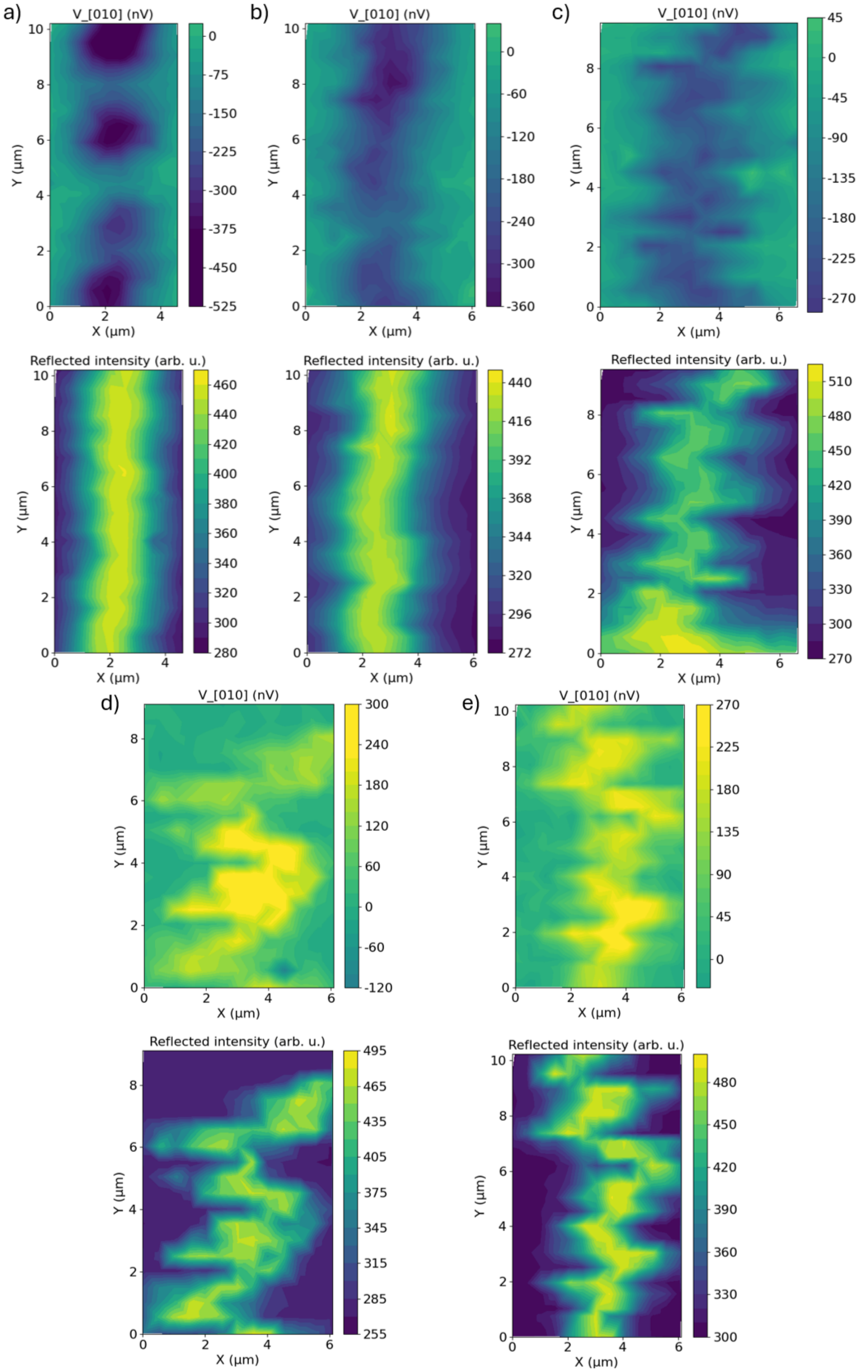

Figure 3.14 Thermovoltage $V_{[010]}$ measured in Mn_3GaN Hall bar at different temperatures and the reflected intensity of the area of the device scanned. a) 20 K, b) 80 K, c) 140 K, d) 296 K, e) 340 K. The laser power was 8 mW.

With better sample stability, larger areas of the Mn_3GaN Hall bar were scanned at 20 K and 296 K, covering approximately half the Hall bar's length. Attempts to scan the entire length were unsuccessful due to sample drift during measurements, even at these more stable temperatures. The effect of an applied magnetic field (± 500 mT) was also tested at both temperatures. Figure 3.15 compares scans under these conditions, showing a consistent signal sign change between 20 K and 296 K but no significant variation with the applied magnetic field.

Distinct structures approximately 1-2 μm in size were observed at both temperatures, distributed across the entire Hall bar. These features, indicated by orange arrows in Fig. 3.15, remained unchanged even after heating above the Néel temperature (340 K) or cooling in opposite magnetic fields, suggesting robust and stable placement. However, one point consistently produced a signal with an opposite sign to the rest of the sample. At 20 K, most signals were negative except for this spot, while at 296 K, the overall signal was positive, with the same spot producing a negative signal. This behaviour made this a point of interest a focus for further investigation.

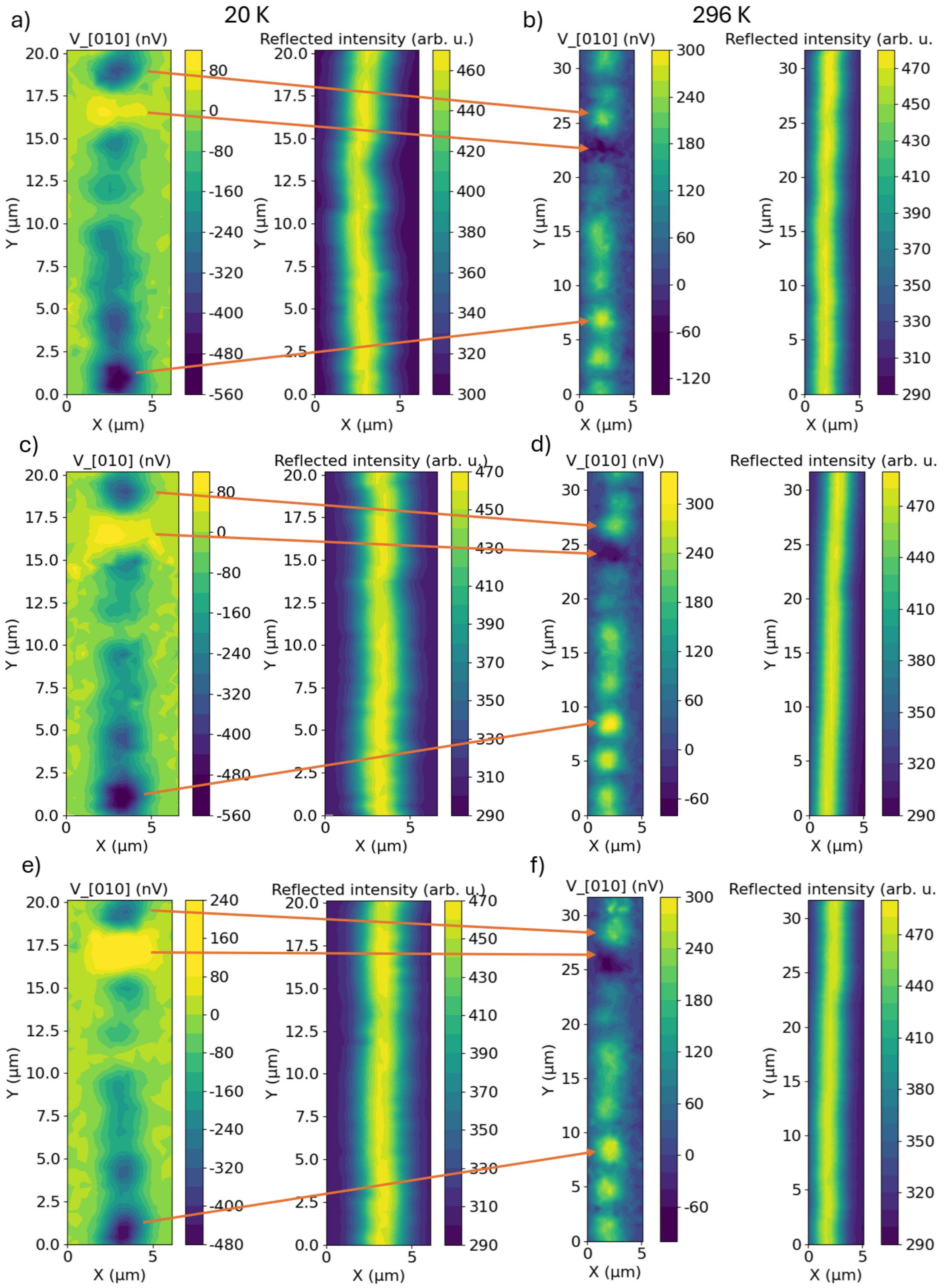

Figure 3.15 Thermovoltage $V_{[010]}$ measured in Mn_3GaN Hall bar at 20 K and room temperature (296 K) and the reflected intensity of the area of the device scanned. Orange arrows highlight the same points on the sample at different temperatures. a) 20 K (-500 mT), b) 296 K (-500 mT), c) 20 K (0 mT), d) 296 K (0 mT), e) 20 K (500 mT), f) 296 K (500 mT). The laser power was 8 mW.

To explore this anomaly, the effect of laser polarisation was tested to uncover the possible presence of linear/circular photovoltage. Three measurements were performed: one with circularly polarised light, as shown in 3.6, and two with linearly polarised light achieved by removing the $\lambda/4$ waveplate and rotating the $\lambda/2$ waveplate by 45° to change the polarisation by 90°. Figure 3.16 shows no detectable dependence of the signal on the laser polarisation, consistent with expectations that polarisation should not influence a thermal gradient.

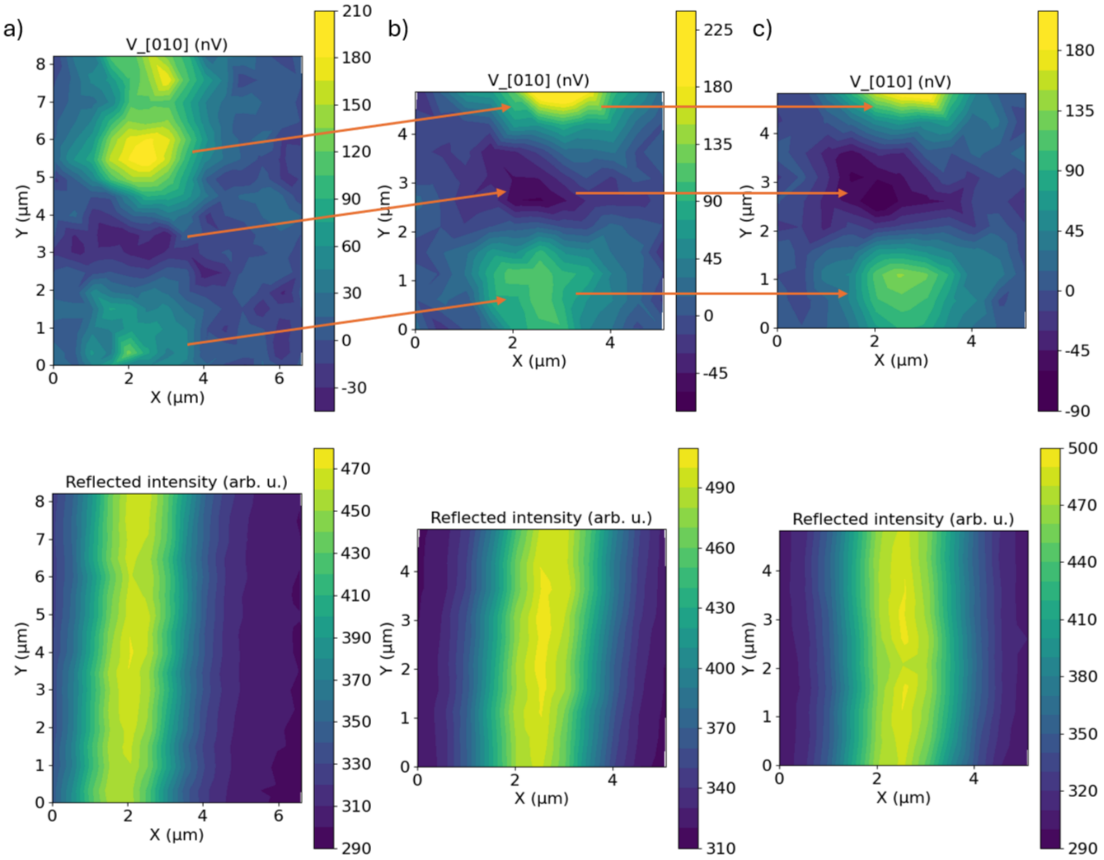

Figure 3.16 Polarisation dependence of thermovoltage $V_{[010]}$ measured in Mn_3GaN Hall bar at room temperature (296 K) and the reflected intensity of the area of the device scanned. Orange arrows highlight the same points on the sample. a) circularly polarised light, b) linearly polarised light, c) linearly polarised light rotated by 90° compared to b). The laser power was 8 mW.

Laser power was also varied to determine its effect on the observed features. Measurements were conducted at 4 mW, 8 mW (the standard power used in other tests), and 16 mW by adjusting the first $\lambda/2$ waveplate in the optical setup. As shown in Fig. 3.17, the signal scaled with laser power across the sample, except at the point of interest, where the signal remained roughly constant. At lower intensities, the anomaly became more prominent as other signals diminished, making it easier to distinguish.

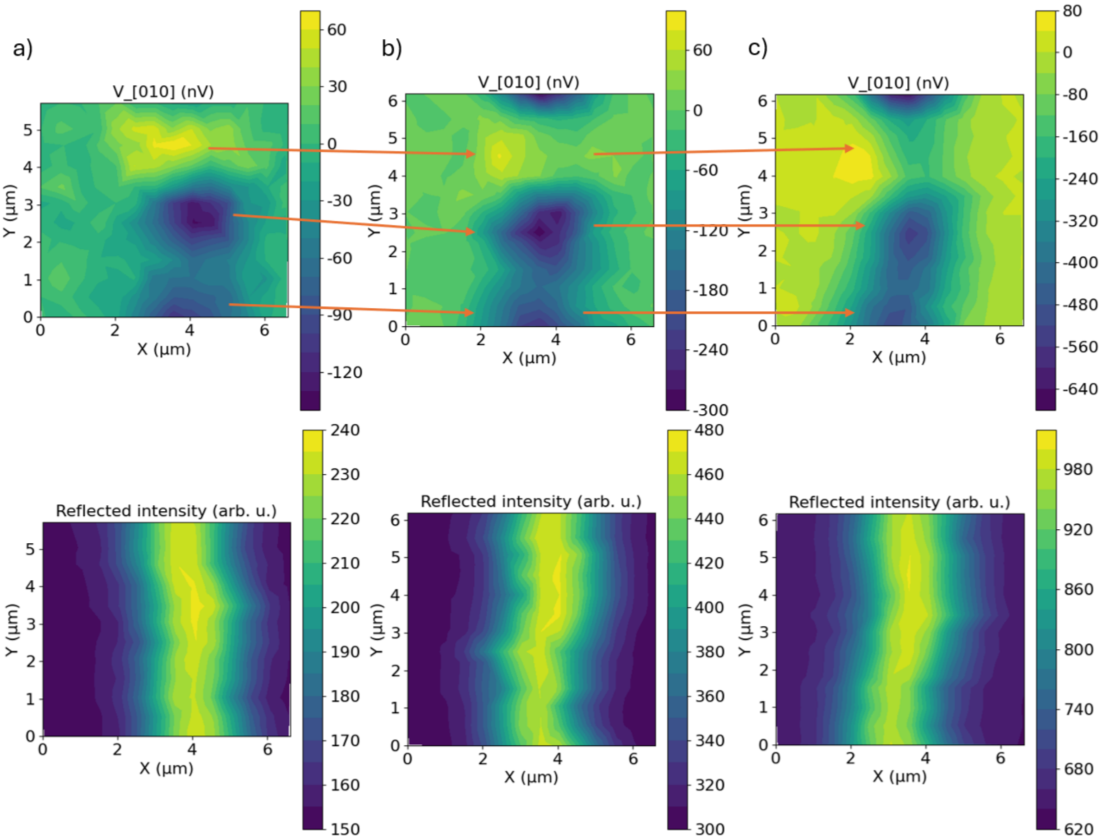

Figure 3.17 Laser power dependence of thermovoltage $V_{[010]}$ measured in Mn_3GaN Hall bar at room temperature (296 K) and the reflected intensity of the area of the device scanned. Orange arrows highlight the same points on the sample. a) 4 mW, b) 8 mW, c) 16 mW.

Finally, heat-assisted writing [5, 4] was attempted to manipulate the signal at the point of interest. A laser with a power of 25 mW was scanned over this region and its surroundings (approximately 4 μm in each direction) in the presence of a -500 mT in-plane magnetic field. Then, the scanning experiment with a low laser power was performed. Figure 3.18 compares the sample before and after this process, showing no observable changes in the signal or its surroundings.

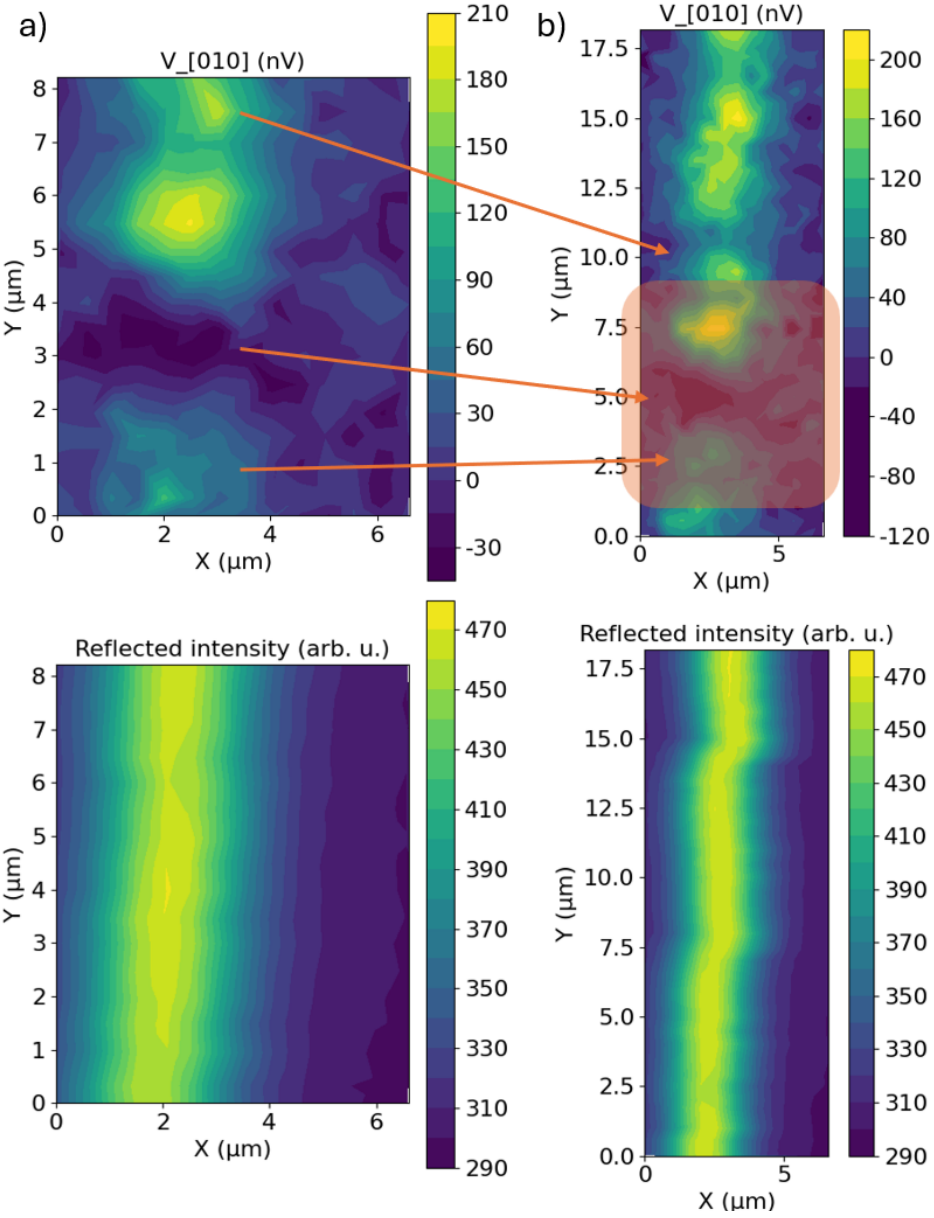

Figure 3.18 Thermovoltage $V_{[010]}$ measured in Mn_3GaN Hall bar at room temperature (296 K) before and after heat-assisted writing with -500 mT in-plane magnetic field. Orange arrows highlight the same points on the sample, and the orange rectangle shows the area where the heat-assisted writing was performed. a) before heat-assisted writing, b) after heat-assisted writing. The laser power was 8 mW.

Given the robustness of the $V_{[010]}$ thermovoltage signal, which only changed with temperature and consistently originated from specific hotspots, further investigation was conducted using a scanning electron microscope (SEM) to identify possible structural defects. As shown in Fig. 3.19, the sample surface near the anomalous signal showed significant irregularities. While minor surface defects were also identified elsewhere (Fig. 3.20), no clear correlation between these defects and the other hotspots detected in thermoscanning measurements could be established.

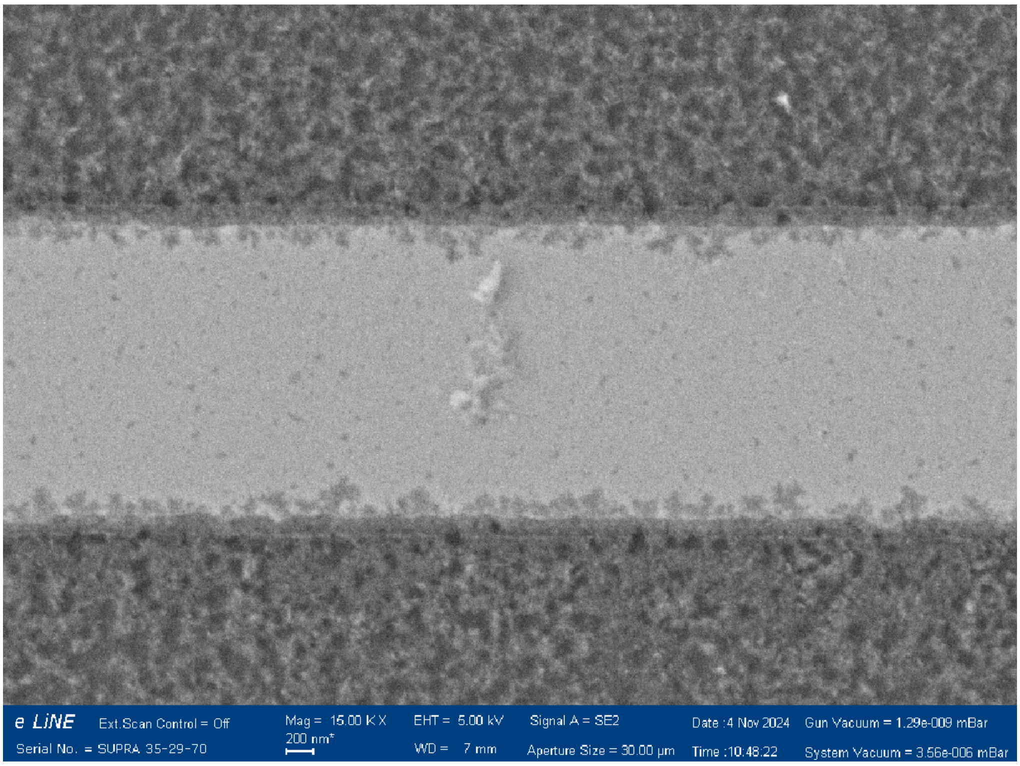

Figure 3.19 Detailed scanning electron microscopy (SEM) image of the Mn3GaN device (21-270_#1_A) showing roughness in the sample surface. Image taken with the assistance of Zbyněk Šobáň.

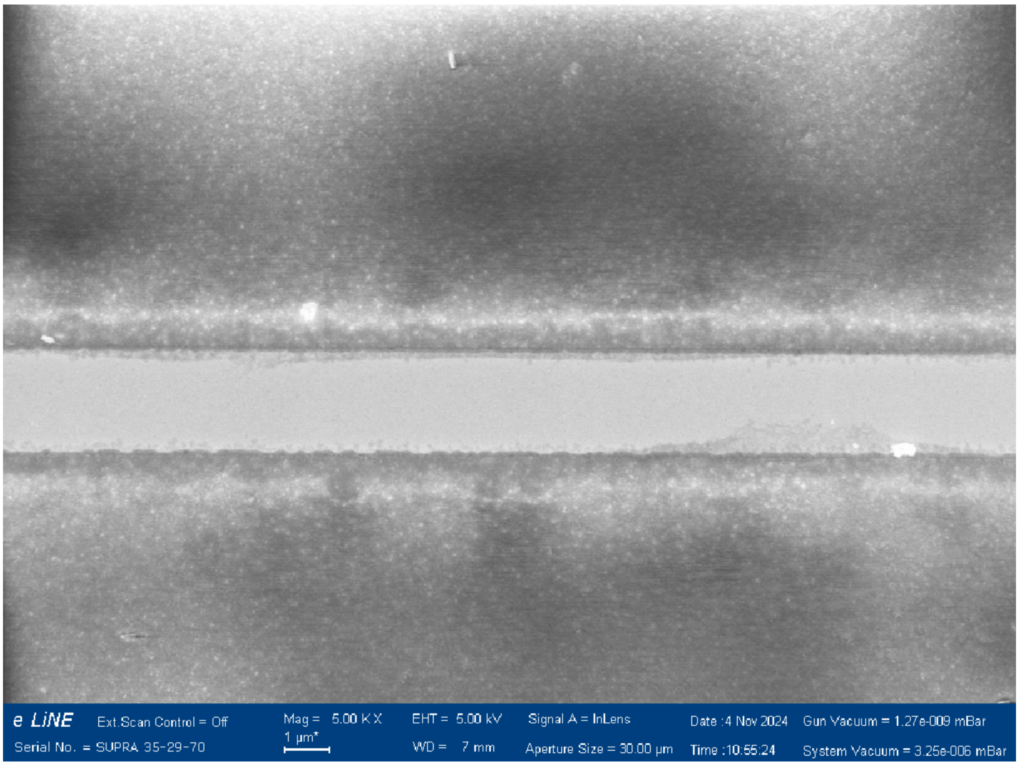

Figure 3.20 Detailed scanning electron microscopy (SEM) image of the Mn3GaN device (21-270_#1_A) showing minor defects in the sample surface. Image taken with the assistance of Zbyněk Šobáň.

3.5.4 Interpretation of the results of the thermoscanning experiment on $\mathrm{Mn_3GaN}$

The thermoscanning experiments revealed no dependence of the detected $V_{[100]}$ and $V_{[010]}$ thermovoltage signals on the applied in-plane magnetic field (± 500 mT) or on cooling the sample through the Néel temperature in the presence of a magnetic field. Similarly, no changes were observed when varying the polarisation of the incident laser light used to generate the temperature gradient. However, the signals were found to scale with laser intensity, indicating a dependence on the magnitude of the thermal gradient. Additionally, the signals reversed signs between 140 K and 296 K, and distinct hotspots were observed across the Hall bar, remaining stationary regardless of the experimental conditions. One particular hotspot producing a signal of the opposite sign to the others was linked to a surface irregularity visible in SEM imaging.

When measuring $V_{[010]}$, a signal generated by the anomalous Nernst effect (ANE) should vary with magnetic domain orientation and vanish above the Néel temperature, where magnetic ordering disappears. Similarly, a signal from the ordinary Nernst effect would change sign with an opposing magnetic field and disappear without an applied field. Moreover, during field cooling, the applied magnetic field would be anticipated to influence the sample's magnetic state, as observed in $\mathrm{Mn_3NiN}$ [4]. However, since neither behaviour was observed, the detected signals are unlikely to originate from the ANE or the ordinary Nernst effect. The lack of an ANE signal suggests that most of the $\mathrm{Mn_3GaN}$ sample is likely in the Γ_{5g} phase, where Berry curvature contributions are cancelled by mirror symmetries, resulting in negligible ANE.

One possible explanation of the detected signal is the Seebeck effect, which generates a thermally induced voltage along the direction of the temperature gradient. In this experiment, however, the laser-induced thermal gradient was primarily out-of-plane, with only minor in-plane components. These in-plane gradients should cancel out across the sample, except at the edges where thermal gradients from the side could produce in-plane voltages. If this were the case, opposite signal directions would be expected at opposing edges of the Hall bar. However, both the $V_{[010]}$ and $V_{[100]}$ signals consistently originate from points roughly centred within the Hall bar, not its edges.

The laser spot size, which was approximately 1.5 μm at the start of each measurement, was regularly optimised using the scanning knife-edge method. However, sample drift during measurements caused the spot size to increase slightly, particularly at higher temperatures. At stable temperatures (20 K and 296 K), the spot size grew to 1.6-1.8 μm after a scan. At intermediate temperatures, such as 140 K, it could reach 2.2-2.4 μm, exceeding the 2 μm width of the Hall bar. This loss of spatial resolution affects the apparent size of features detected in thermoscanning. For instance, an irregularity identified using SEM spanned about three-quarters of the Hall bar width and was 500 nm long, while thermoscanning measurements exaggerated it to the full width and a length of 1000–1500 nm.

Given the consistency of the signals in the centre of the Hall bar and the absence of edge effects, we conclude that the signal originates within the sample itself rather than from its boundaries. While the surface of the sample appears smooth apart from one notable irregularity, it is likely that grains, defects, or impurities within the sample volume are causing localised dissipation of heat and generating the thermo-voltage resulting from the Seebeck effect. This would result in in-plane thermal gradients that do not cancel out, generating the observed signals. Thus, the features detected in thermoscanning are more likely due to structural or compositional irregularities rather than magnetic domains.

The change in the signal's sign with temperature is most plausibly explained by the Seebeck effect. Although direct measurements of the Seebeck coefficient in thin-film Mn_3GaN are (to our best knowledge) unavailable, studies on other Mn_3-based antiperovskites provide useful context. For instance, [52] shows a temperature-dependent sign change in the Seebeck coefficient of Mn_3SnN, and [53] reports similar behavior in Mn_3PdN. his suggests that a similar sign change may occur in Mn_3GaN, potentially between 140 K and 296 K, corresponding to the observed reversal in the detected signal. The substrate is unlikely to contribute significantly to the detected signal, as measurements taken away from the Hall bar show signals that are much smaller and close to zero.

To confirm the hypothesis regarding the Seebeck effect, direct measurements of the Seebeck coefficient in Mn_3GaN would be highly beneficial. A sign change in the coefficient between 140 K and 296 K would strongly support this explanation. While it may also be possible to estimate the Seebeck coefficient using the thermoscanning setup, stability issues at intermediate temperatures make such measurements extremely challenging. Significant drift and instability, particularly above 20 K and below 296 K, would render these experiments time-intensive and unreliable with the current setup. A sample with on-chip heaters and thermometers, as described in [22], would be one of the possible solutions.

Additionally, anomalous Hall effect (AHE) measurements could help verify the Γ_{5g} phase of the sample. As with the ANE, the AHE should be negligible in this phase due to symmetry constraints. However, current limitations in the AHE measurement setup prevent low-temperature measurements, delaying these tests until the issues are resolved.

To improve measurement reliability, future experiments should include wider Hall bars (5-10 μm), ensuring the laser spot size remains smaller than the bar width. This would also minimise signal contamination from surrounding areas, though spatial resolution would still be constrained by sample movement in the cryostat. Hall bars oriented at 45° or 90° relative to each other could enable testing of directional dependencies in the applied magnetic field, addressing current limitations in sample rotation.

4 Wide-field Kerr microscopy

4.1 Introduction to magneto-optical phenomena

Magneto-optics explores the interaction between light and magnetised materials, where the magnetic order modifies the properties of the light. These modifications emerge from the interplay of the light wave with the material's electronic structure, influenced by spin-orbit coupling and the Zeeman effect. The interaction results in changes to the polarisation state of light, including rotation of its polarisation plane and the change in ellipticity. Magneto-optical phenomena are sensitive to the relative orientation of the material's magnetisation and the direction of light propagation, enabling detailed insights into the material's magnetic properties [54].

The importance of magneto-optics lies in its ability to provide non-invasive and highly localised magnetisation measurements, which is crucial for studying complex magnetic structures. The sensitivity of these techniques to electronic and magnetic interactions enables applications ranging from fundamental research on magnetic phenomena to industrial uses such as magnetic data storage and imaging of magnetic patterns.

Magneto-optical effects are classified based on how the material's magnetisation vector aligns with the light's wave vector. In the Faraday geometry (see Fig. 4.1), where the light propagates through the material with its wave vector parallel to the magnetisation, the interaction results in magnetic circular birefringence (MCB) and dichroism (MCD) depicted in Fig. 4.2. These effects cause the polarisation plane of the transmitted light to rotate, a phenomenon known as the Faraday effect, and are linear in magnetisation. This geometry is widely used for probing bulk properties of magnetic materials and understanding their internal magnetic order [55].

In contrast, the Voigt geometry is observed when the wave vector of the light is perpendicular to the magnetisation. This alignment produces magnetic linear birefringence (MLB) and dichroism (MLD), leading to changes in both the polarisation state and the intensity of the transmitted light. The Voigt effect is particularly sensitive to magnetisation components perpendicular to the light path, making it a complementary tool to the Faraday effect for studying anisotropic magnetic properties. Unlike the Faraday effect, the Voigt effect exhibits a quadratic dependence on magnetization and is generally weaker in magnitude [56, 55].

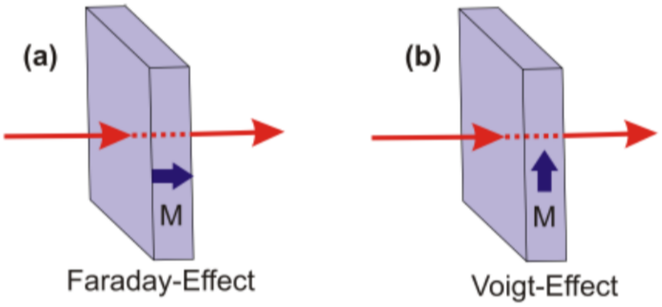

Figure 4.1 Illustration of the Farraday geometry (a) and the Voigt geometry (b) of magneto-optical effects. Adapted from [57].

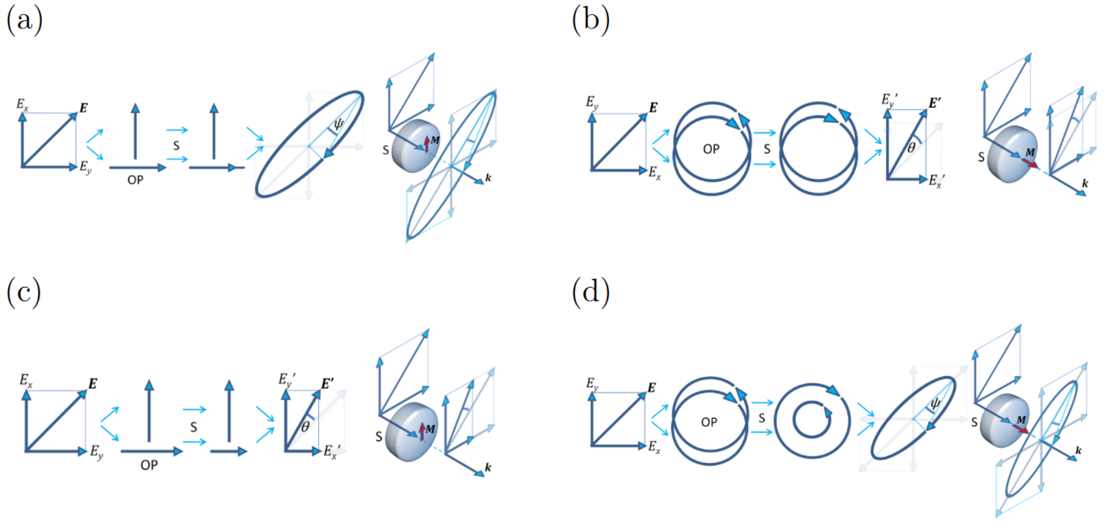

Figure 4.2 Magneto-optical phenomena: (a) magnetic linear birefringence (MLB), (b) magnetic circular birefringence (MCB), (c) magnetic linear dichroism (MLD), (d) magnetic circular dichroism (MCD). Adapted from [55].

The magneto-optical Kerr effect (MOKE) occurs when linearly polarised light reflects off a magnetised surface, causing changes in the reflected light's polarisation state, including rotation and ellipticity. These changes result from the interaction between the light wave and the surface's magnetisation, mediated by spin-orbit coupling and modifications to the electronic structure near the surface. The sensitivity of MOKE to surface and near-surface magnetisation makes it particularly suitable for studying thin films and magnetic microstructures [58].

The Kerr effect is categorised into three geometries depending on the orientation of the magnetisation vector relative to the incident light and the plane of reflection, shown in Fig. 4.3. In polar MOKE, the magnetisation is perpendicular to the sample surface, making this geometry highly sensitive to out-of-plane magnetisation components. This configuration is widely used for imaging perpendicular magnetic domains and observing transitions in thin films. Longitudinal MOKE, where the magnetisation lies parallel to the sample surface and in the plane of incidence, is primarily used to study in-plane magnetisation. The transverse geometry, sensitive to magnetisation perpendicular to the plane of incidence and in the sample plane, alters the amplitude of the reflected light rather than its polarisation [58, 54].

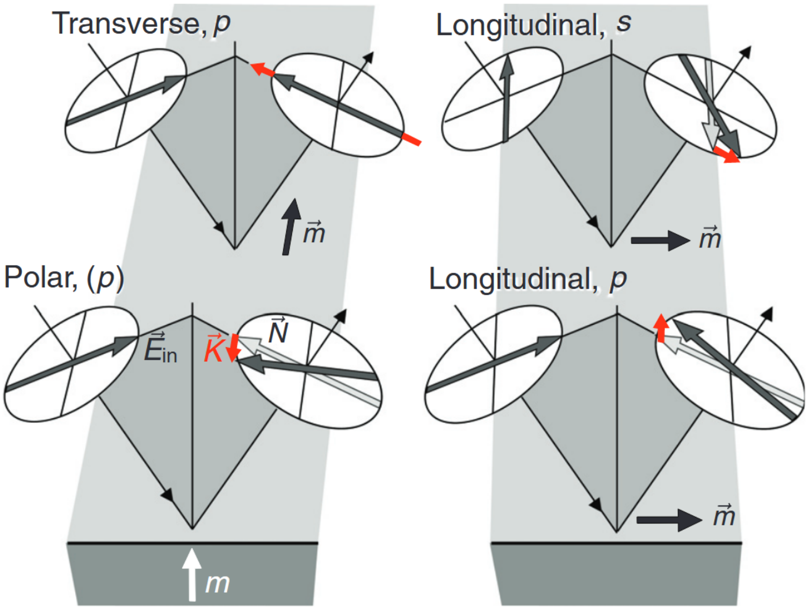

Figure 4.3 Schematics of the basic Kerr effect modes. Shown is the magnetisation vector $\vec{m}$, the electrical vector of the incident, plane-polarised light wave $\vec{E}_{in}$, the regularly reflected field amplitude $\vec{N}$, and the Kerr amplitude $\vec{K}$. Inversion of the magnetisation direction would lead to an inversion of the Kerr amplitude vectors. Adapted from [58].

MOKE has traditionally been used to study ferromagnetic materials, but its applications have expanded to include antiferromagnetic systems, particularly those with non-collinear spin arrangements. In these cases, the Kerr signal arises from the non-zero Berry curvature in the electronic structure, similar to the processes responsible for the AHE and ANE. Studies by [59] demonstrate the effectiveness of polar MOKE imaging for visualising magnetic octupole domains in Mn_3Sn, a non-collinear antiferromagnet. Similarly, [60] highlights the use of MOKE for probing antiferromagnetic domains in Mn_3Ir films, further showcasing its capability for probing antiferromagnetic domains in non-collinear systems. Given that altermagnets exhibit similar properties to non-collinear antiferromagnets, including AHE and ANE driven by symmetry-dependent Berry curvature effects, it is reasonable to anticipate that MOKE could also be employed for imaging altermagnetic materials.

4.2 Wide-field Kerr microscope

Wide-field Kerr microscopy is a powerful imaging technique that utilises the magneto-optical Kerr effect (MOKE) to visualise magnetic domain structures. By analysing changes in the polarisation of light upon reflection from a magnetised surface, the technique can resolve domain configurations in ferromagnetic and antiferromagnetic materials. Its primary strength lies in its ability to capture domain structures across a wide field of view, making it particularly suited for studies of thin films and large magnetic systems [61, 62].

The polar geometry of MOKE is most commonly employed in wide-field Kerr microscopy, as it is sensitive to out-of-plane magnetisation components and provides high contrast for domains with perpendicular anisotropy. Longitudinal and transverse geometries are also applicable for in-plane magnetisation imaging, although these are less commonly utilised in wide-field setups, as they require larger angles of incidence and thus objectives with high numerical aperture [63].

The core of a wide-field Kerr microscopy setup, depicted in Fig. 4.4, is an optical polarisation microscope modified for magneto-optical measurements. A stable light source, such as an LED, provides uniform illumination of the sample. The non-coherent polarised light interacts with the magnetised surface, and the reflected beam is analysed for changes in the polarisation state, which are indicative of the underlying magnetic structure. Köhler illumination is commonly employed to ensure even lighting across the sample, essential for high-contrast imaging of magnetic domains [64].

The angle of incidence of the light plays a critical role in the type of information obtained. Perpendicular (normal) incidence is most commonly used in polar Kerr microscopy, as it maximises sensitivity to out-of-plane magnetisation components. This geometry ensures that the detected Kerr rotation is directly related to the perpendicular magnetic domains without significant contributions from in-plane components.

In contrast, oblique incidence introduces additional sensitivity to in-plane magnetisation components, enabling the use of longitudinal or transverse MOKE. Oblique incidence angles are particularly useful when analysing complex domain structures or when combining out-of-plane and in-plane imaging. However, this geometry can also introduce complications, such as increased ellipticity and parasitic contributions from sample surface roughness or non-uniformity, which require careful calibration and optimisation of the optical setup [64, 61].

Modern systems, such as those developed by Schäfer and Soldatov [65], incorporate motorised analysers and compensators to enhance sensitivity and suppress artefacts, ensuring that signals from the Kerr effect are accurately isolated. Additionally, digital image processing techniques are employed to subtract background noise, further improving the visibility of magnetic domains. These advancements enable clear visualisation of even subtle magnetisation contrasts in complex materials [63].

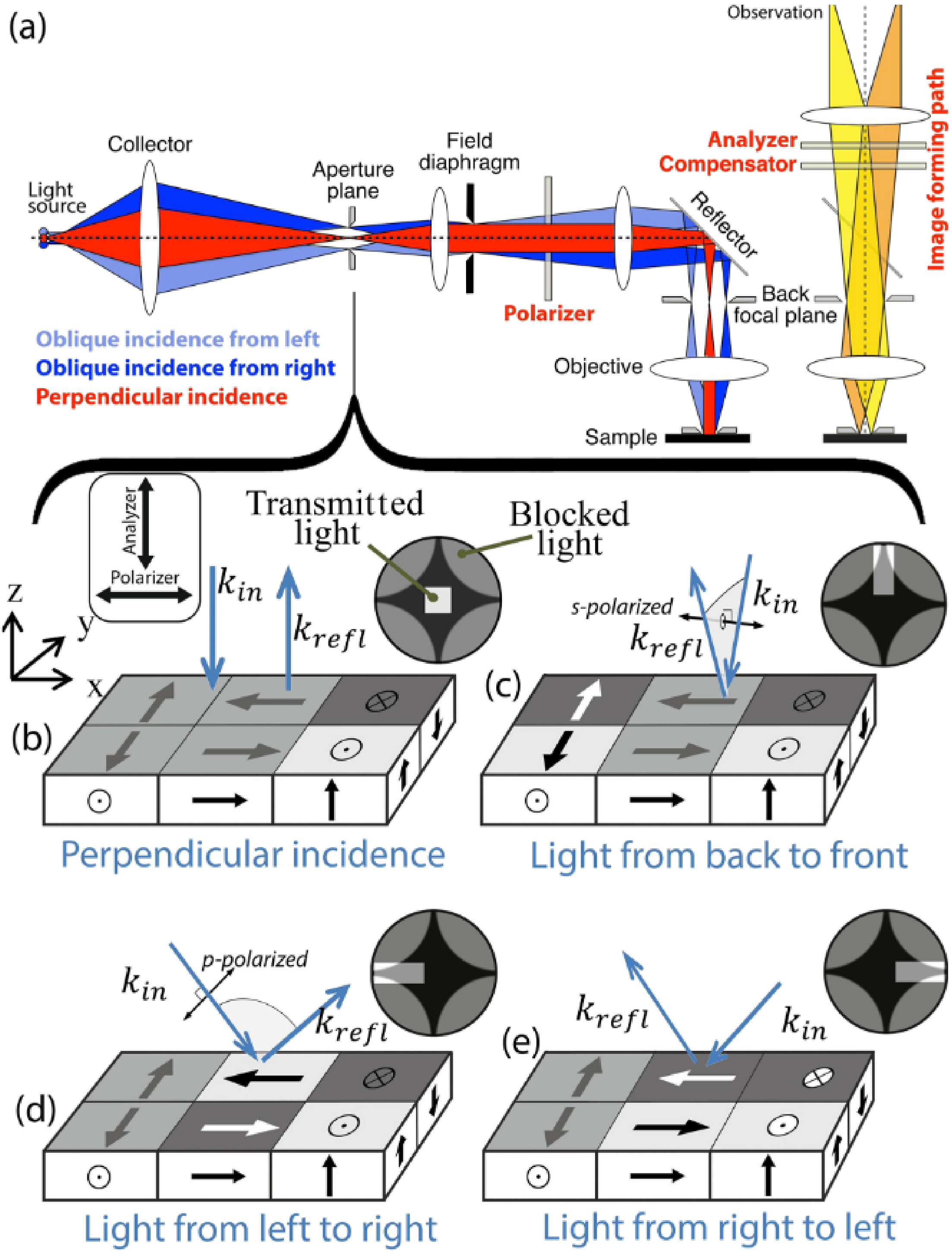

Figure 4.4 (a) Ray paths for illumination and image formation of a wide-field Kerr microscope with displaceable slit aperture, conventionally used for the adjustment of the sensitivity direction. The basic geometries of the Kerr contrast are illustrated as follows: polar contrast (b), longitudinal with s-polarized light (c), and longitudinal in transverse direction with p-polarized light with direct (d) and inverted contrast (e). Adapted from [64].

The spatial resolution of wide-field Kerr microscopy is governed by the optical diffraction limit, reaching approximately 300 nm under optimal conditions with visible light. However, real-world factors such as lens aberrations, sample roughness, and alignment precision often limit practical resolution to slightly larger scales [61].

Sensitivity to Kerr rotation is critical for detecting weak magnetic contrasts. The wide-field Kerr microscopy system developed by Schäfer and Soldatov achieves an exceptional sensitivity of 2.4 mdeg (0.6 mdeg in the pure in-plane mode), enabling the visualisation of subtle magnetisation changes in ultrathin films and complex antiferromagnetic materials. These performance levels are achieved through calibration and optimisation of optical components, such as fine adjustments to analyser angles and compensator settings [64].

Wide-field Kerr microscopy offers a unique combination of sensitivity, versatility, and efficiency for imaging magnetic domains. Its ability to visualise both out-of-plane and in-plane magnetisation components makes it a valuable tool for studying magnetic systems. Furthermore, its wide field of view and straightforward sample preparation requirements make it accessible for a variety of research applications.

However, the technique is limited to surfaces with sufficient reflectivity. Additionally, while its lateral resolution is suitable for most magnetic studies, it falls short compared to nanoscale imaging methods like X-ray microscopy (XMLD, XMCD), which has been very recently used to map altermagnetic states in MnTe in the work of [66].

4.3 Experimental setup

As part of this work, a wide-field Kerr microscope was constructed in the Laboratory of OptoSpintronics at the Department of Chemical Physics and Optics. The microscope design was based on the earlier work of Kristýna Hovořáková [67] and represents a simplified redesign of her original setup. While the previous microscope was conceived as a highly versatile instrument capable of functioning both as a scanning and wide-field Kerr microscope, the new setup prioritises reduced complexity and improved stability. Additionally, its portability allows it to be easily transported between laboratories, further enhancing its usability. The newly built microscope, shown in Fig. 4.5, was constructed with the assistance of Tomáš Trejtnar and successfully tested as part of his Bachelor's thesis, where the performance of novel light sources for Kerr microscopy was evaluated [68].

Although the new microscope was demonstrated to successfully image switched domains in FePt multilayers [68], it was not used for the measurements in this work. The primary reason was the limited sensitivity of the setup, which is critical for imaging magnetic domains in non-collinear antiferromagnetic and altermagnetic materials that produce only weak Kerr signals. Additionally, the setup is restricted to room-temperature measurements, whereas most samples in this study (see Table 2.1) have Néel temperatures below room temperature, making temperature control essential for domain imaging.

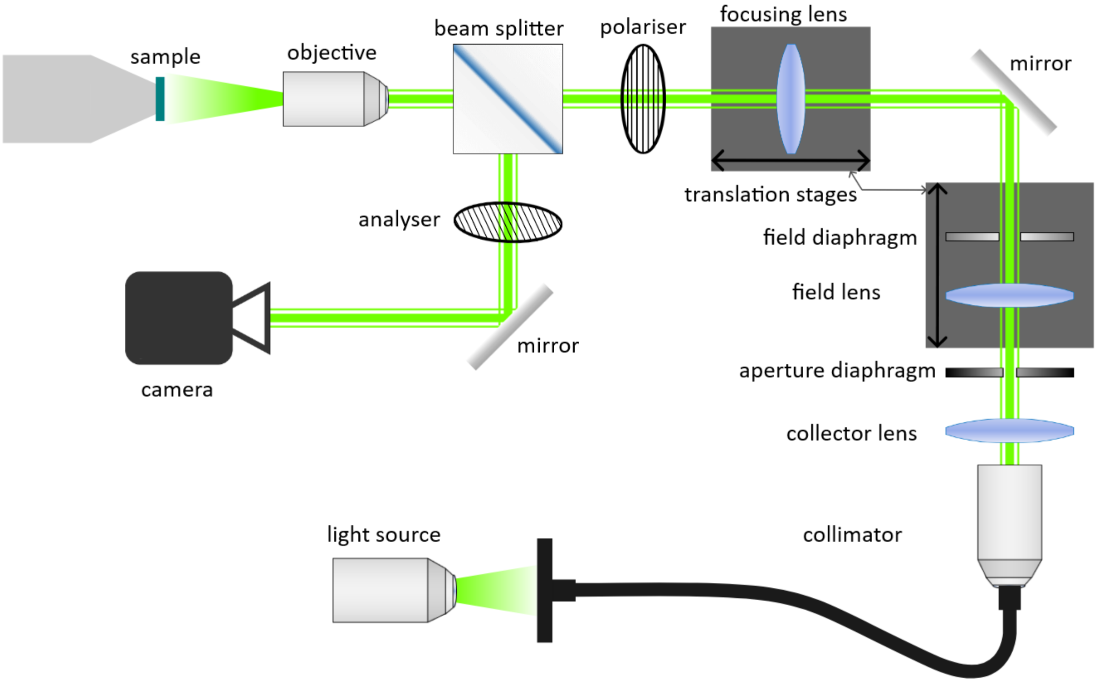

Figure 4.5 Schematics of the newly built wide-field Kerr microscope. Adapted from [68].

To address these limitations, the wide-field Kerr microscopy measurements were conducted at IFW Dresden using the state-of-the-art microscope developed by Rudolf Schäfer and Ivan Soldatov [65]. This setup is optimised for low-temperature measurements, reaching temperatures as low as 70 K with liquid nitrogen cooling. It also provides the capability to apply magnetic fields of ± 300 mT in-plane and ± 100 mT out-of-plane. Furthermore, the system incorporates active sample stabilisation via a 3D translation mechanism with feedback from the camera, ensuring exceptional measurement stability. Its spatial resolution, reaching approximately 500 nm, enables precise imaging of fine domain structures.

The IFW Dresden setup utilises a novel LED-based illumination system (see Fig. 4.6), described in detail in [64]. This system allows for precise control of illumination angles and polarisation states, enabling seamless switching between polar and longitudinal contrasts. Unlike traditional slit aperture systems, which require mechanical adjustments, this setup employs computer-controlled LED pairs to tailor the illumination for specific magnetisation components. The LED arrangement supports real-time contrast optimisation for polar contrasts and is sensitive to out-of-plane magnetisation and longitudinal contrasts, which highlight in-plane magnetisation aligned parallel or transverse to the plane of incidence.

The ability to control s- and p-polarized light further enhances the system's flexibility in resolving complex magnetic structures. For longitudinal contrasts, s-polarization emphasises in-plane magnetisation along the plane of incidence, while p-polarization highlights transverse components. This setup eliminates overlapping polar sensitivity often encountered in conventional systems by enabling precise subtraction and addition of images. The resulting contrast clarity facilitates detailed analyses of magnetisation dynamics and allows for the exploration of multi-axial magnetic systems with unparalleled accuracy.

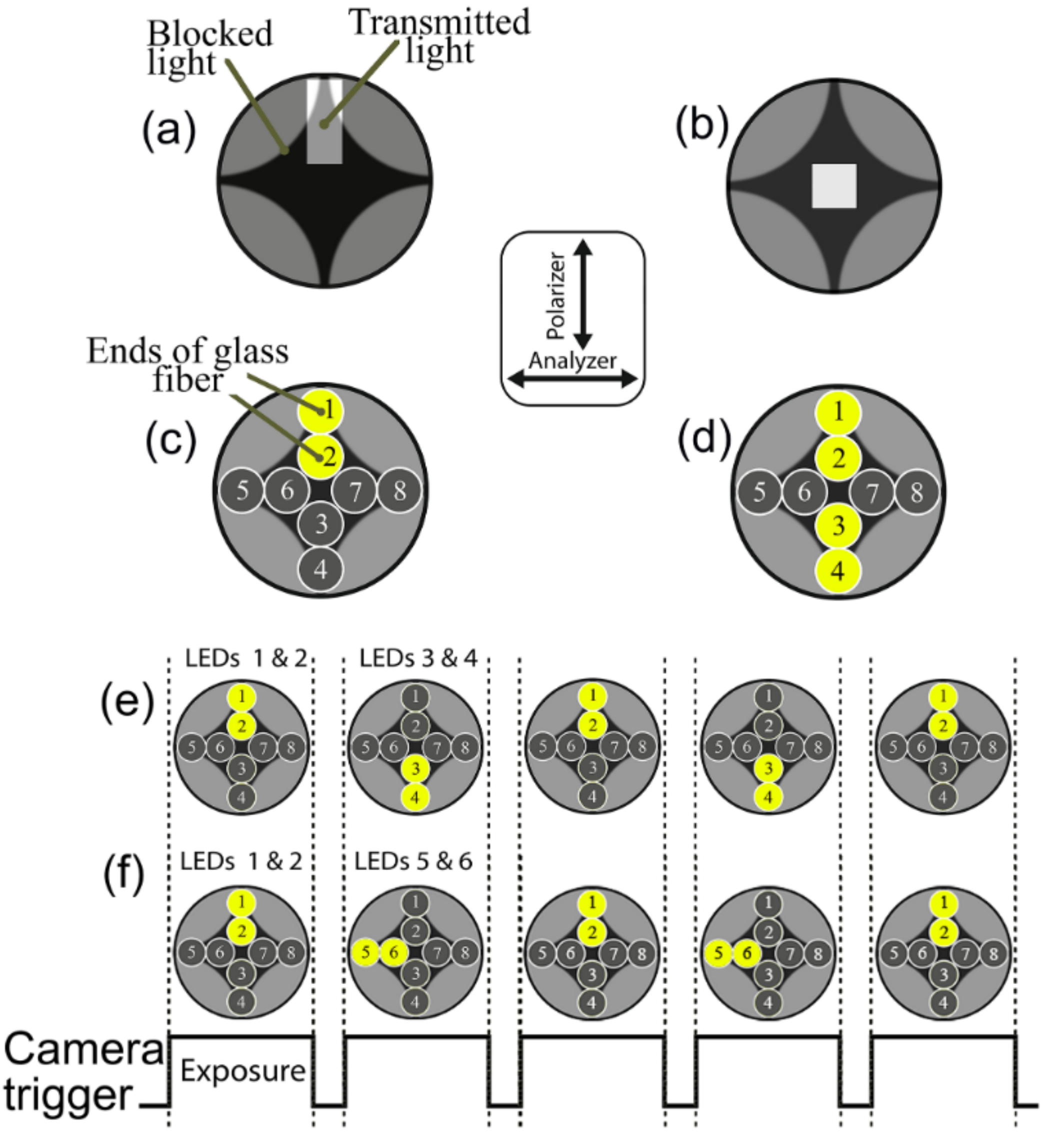

Figure 4.6 Conoscopic images in a conventional setup with displaced (a) and centred (b) aperture slit for oblique and perpendicular incidence, respectively, and corresponding images for the novel setup [(c) and (d)]. The active LEDs are highlighted. (e) Time diagram of the control sequence for the suppression of polar contrast. The corresponding LEDs are switched ON and OFF synchronously with the camera exposure, and the difference of subsequent exposures is taken in situ. An image with pure in-plane sensitivity is obtained then. (f) Alternately activating the LEDs at orthogonal branches of the LED cross leads to dual-component imaging. Adapted from [64].

4.4 Experimental results

All wide-field Kerr microscopy measurements for this work were conducted at IFW Dresden in the laboratory of Rudolf Schäfer and Ivan Soldatov. The first set of measurements, carried out in November 2023, included all the samples listed in Table 2.1 except for VA2684, VA2685, and the patterned samples. These measurements were performed by first capturing a reference image at a specific temperature, followed by cooling or heating the sample across its Néel temperature. To enhance sensitivity to changes in the magneto-optical Kerr (MOKE) signal, the reference image was subtracted in real time from subsequent images during the temperature change. Measurements were also performed in the presence of an in-plane magnetic field (±300 mT) or an out-of-plane magnetic (±100 mT). For all imaging, a Nikon CFI Plan Fluor 60x objective with a 0.85 numerical aperture was utilized.

4.4.1 Experimental results across non-collinear antiferromagnetic and altermagnetic materials

The LED-based light source depicted in Fig. 4.6 was primarily used with polar MOKE sensitivity, which also enables the detection of the Voigt effect, allowing for the imaging of antiferromagnetic domains in thin films [62]. Various LED illumination wavelengths, including red, green, blue, and white (RGB combination), were tested to determine whether a particular wavelength offered improved contrast due to the spectral sensitivity of MOKE effects in various materials. However, as shown in Fig. 4.7, certain samples (VA1530, VA1532, VA1537, MnGeSi20, MnGeSi21), see Tab. 2.1, exhibited surface roughness or damage that significantly affected the measurements. These imperfections amplified the sensitivity of the difference images (generated by subtracting the reference image) to even minor sample movements, making it difficult to distinguish true MOKE signals from artefacts caused by scratches, holes, and other surface defects. Although the automated 3D translation stage, which compensates for sample movement due to thermal expansion of the cold finger, to which the samples are attached inside the cryostat, minimised this issue, its correction capabilities were limited.

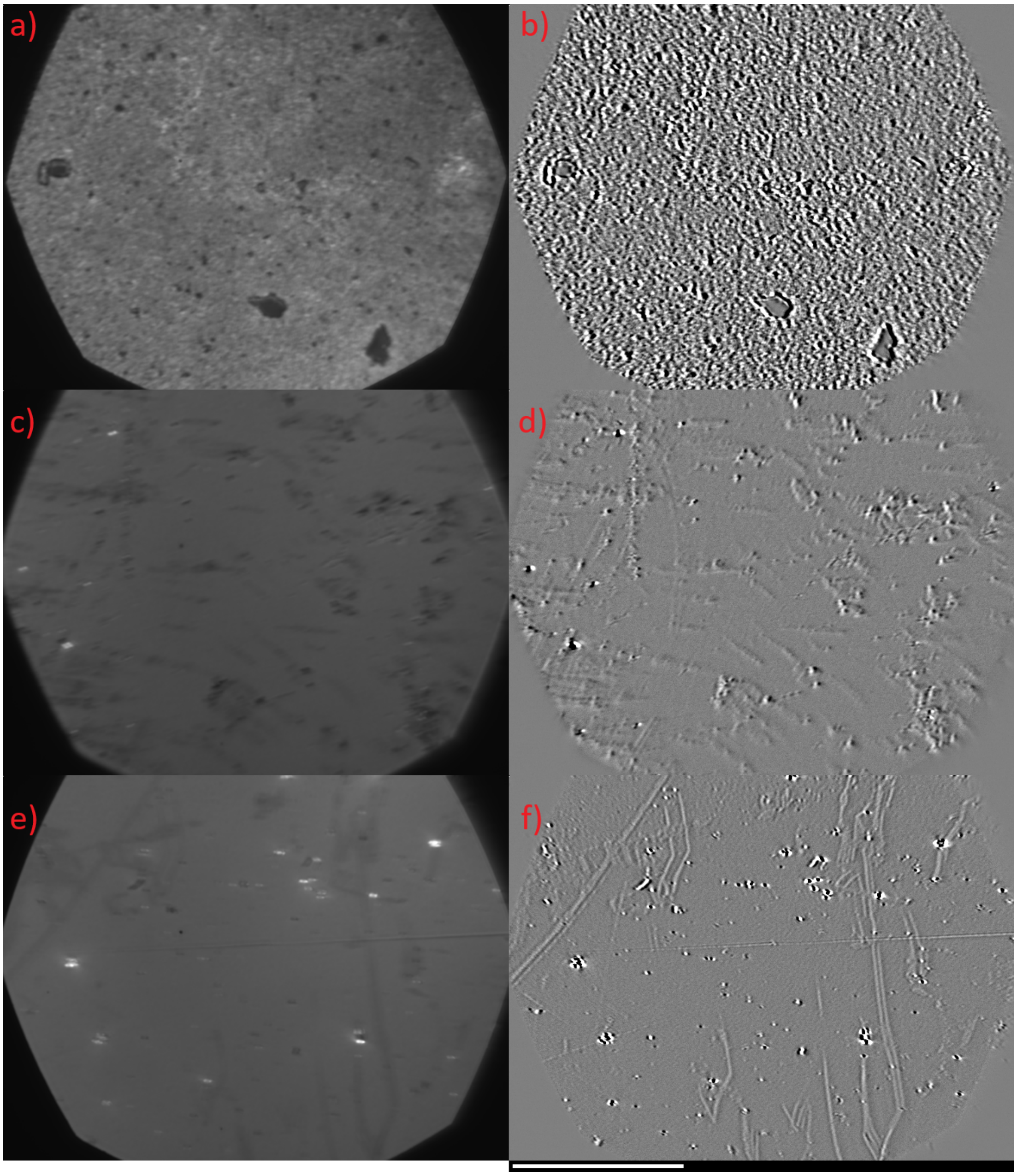

Figure 4.7 Examples of samples with surface damage captured under blue LED illumination with polar MOKE sensitivity. The first column displays reference images, while the second column shows difference images, obtained by subtracting the corresponding reference images captured at the same temperature. A white scale bar at the bottom of each image indicates a length of 50 μm. a)-b) MnTe (VA1537) at 148.5 K, c)-d) $Mn_5(Si_{0.4}Ge_{(0.6)})_3$) (MnGeSi20) at 248.5 K, e)-f) $Mn_5(Si_{0.6}Ge_{(0.4)})_3$) (MnGeSi21) at 298.5 K. Images were acquired using a Nikon 60x/0.85 NA Plan Fluor objective.

No apparent MOKE signal was observed during cooling or heating across the Néel temperature for some of the samples with undamaged surfaces. This was the case for AB22MnSi, MnSi18, 128 and 197, as illustrated in Fig. 4.8. To further investigate these samples, magnetic field loops were conducted at stable temperatures. This involved applying an out-of-plane magnetic field ranging from -100 mT to 100 mT and back to -100 mT, with reference images taken at different field strengths and subtracted to identify any changes. However, no effects were observed, even when different illumination wavelengths (red and blue) were tested. As a result, these samples, like the damaged ones, were excluded from further investigation.

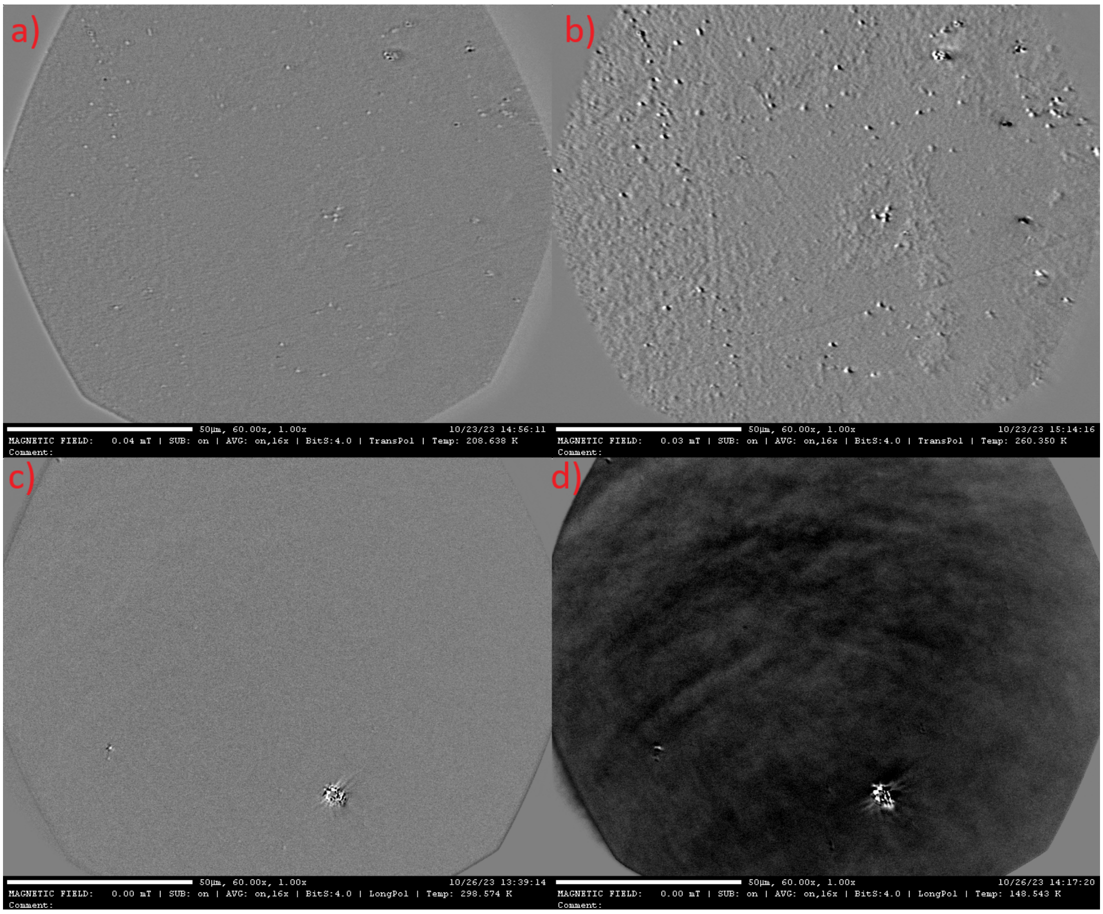

Figure 4.8 Examples of samples showing no significant changes in the MOKE signal during cooling or heating, captured using blue LED illumination with polar MOKE sensitivity. Difference images were generated by subtracting a reference image taken at the same temperature as those in the first column. a) Mn_5Si_3 (AB22MnSi) at 208.5 K, b) Mn_5Si_3 (AB22MnSi) at 260.5 K, c) RuO_2 (128) at 298.5 K, d) RuO_2 (128) at 148.5 K. The wavelike patterns visible in d) are due to the slight surface irregularities. Images were acquired using a Nikon 60x/0.85 NA Plan Fluor objective.

For the non-collinear antiferromagnetic samples Mn_3NiN (MNM22066) and Mn_3GaN (21-271), that were previously subject to the thermoscanning (STGM) experiment, small features approximately 1-2 μm in size were observed appearing across the surface during cooling. These features, referred to as "dots," largely disappeared upon reheating the samples to room temperature. In the case of Mn_3NiN, this behaviour is shown in Fig. 4.9, where the dots vanished between 290 K and 305 K. No other notable changes were detected when the sample was heated from 80 K to 325 K. Investigations focused on the vicinity of the Néel temperature ($T_N = 250K$, as reported in [15]), at which the dots were already fully formed. However, no significant changes in the MOKE signal were observed while transitioning through the Néel temperature without an applied magnetic field, as depicted in Fig. 4.10.

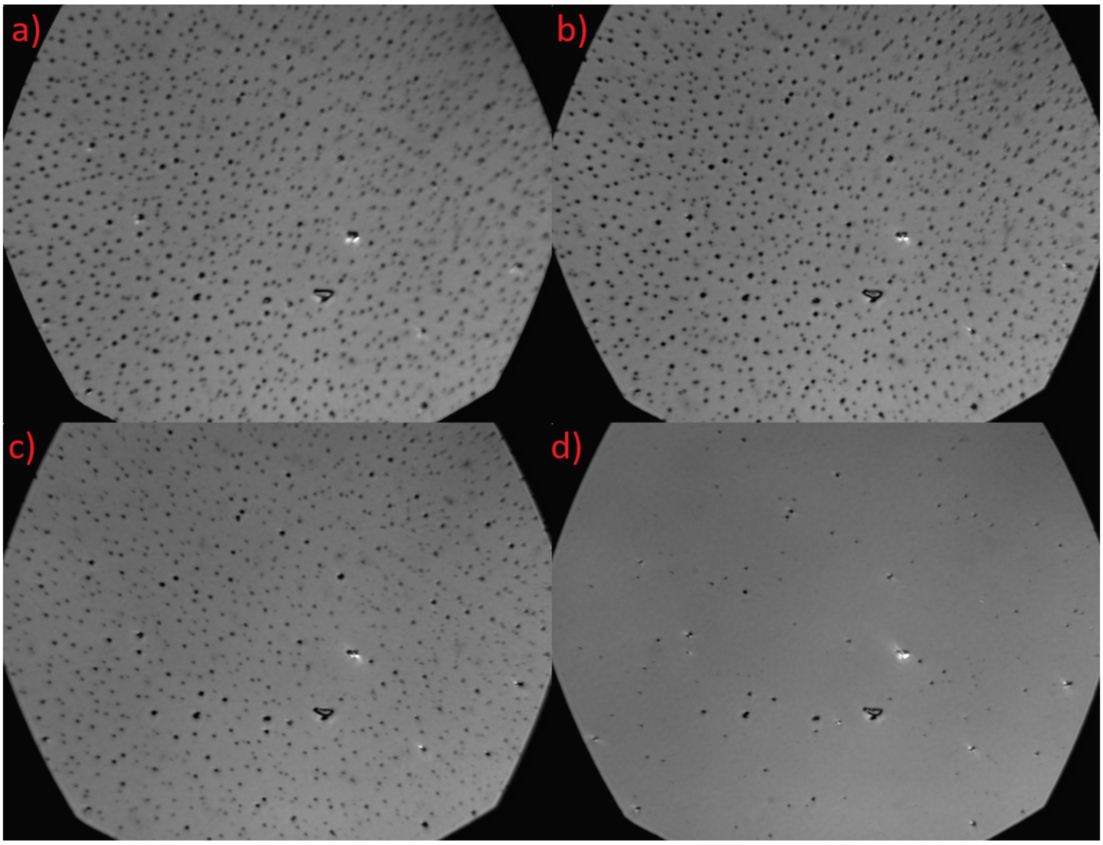

Figure 4.9 Dots disappearing from the surface of Mn_3NiN sample (MNM22066) during heating between 290 K and 305 K with no applied magnetic field under blue LED illumination. Sample temperatures: a) 80 K, b) 280 K, c) 295 K, d) 320 K. Images were acquired using a Nikon 60x/0.85 NA Plan Fluor objective.

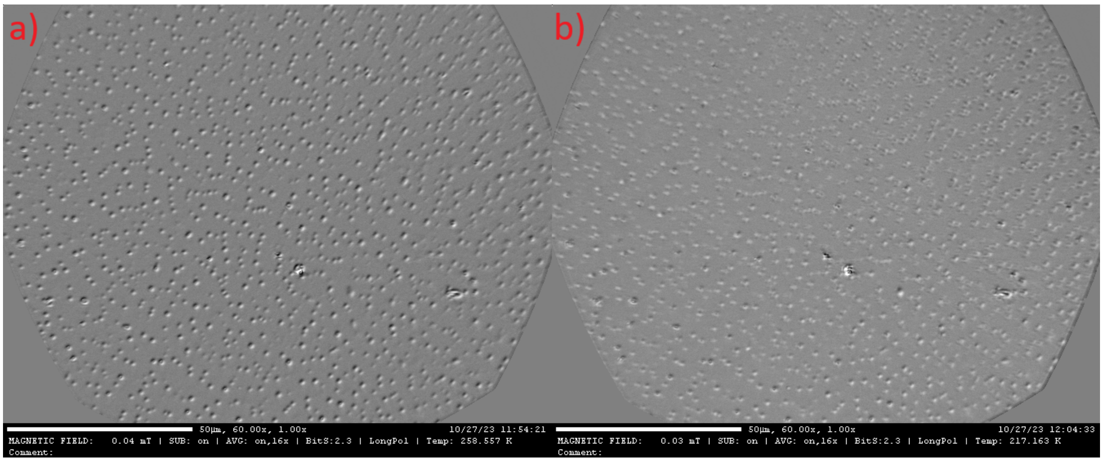

Figure 4.10 Changes in MOKE signal from Mn_3NiN sample (MNM22066) when cooling down across T_N with no applied magnetic field under blue LED illumination. The reference image was taken at 258.5 K. Sample temperatures: a) 258.5 K, b) 217 K. Images were acquired using a Nikon 60x/0.85 NA Plan Fluor objective.

A similar phenomenon was observed in Mn_3GaN (21-271), where dots appeared between 290 K and 285 K during cooling and disappeared between 295 K and 305 K, mirroring the behaviour seen in Mn_3NiN. In addition to these small dots, larger features, approximately 3-6 μm in size and referred to as "speckles," were detected. These speckles formed between 284 K and 275 K during cooling in an out-of-plane magnetic field of 100 mT, as illustrated in Fig. 4.11. Both the dots and speckles were distinguishable without the need for reference image subtraction, as they exhibited distinct reflectivity characteristics, making them easy to differentiate. Beyond this, no further changes were observed in the Mn_3GaN sample, even when cooled to 80 K.

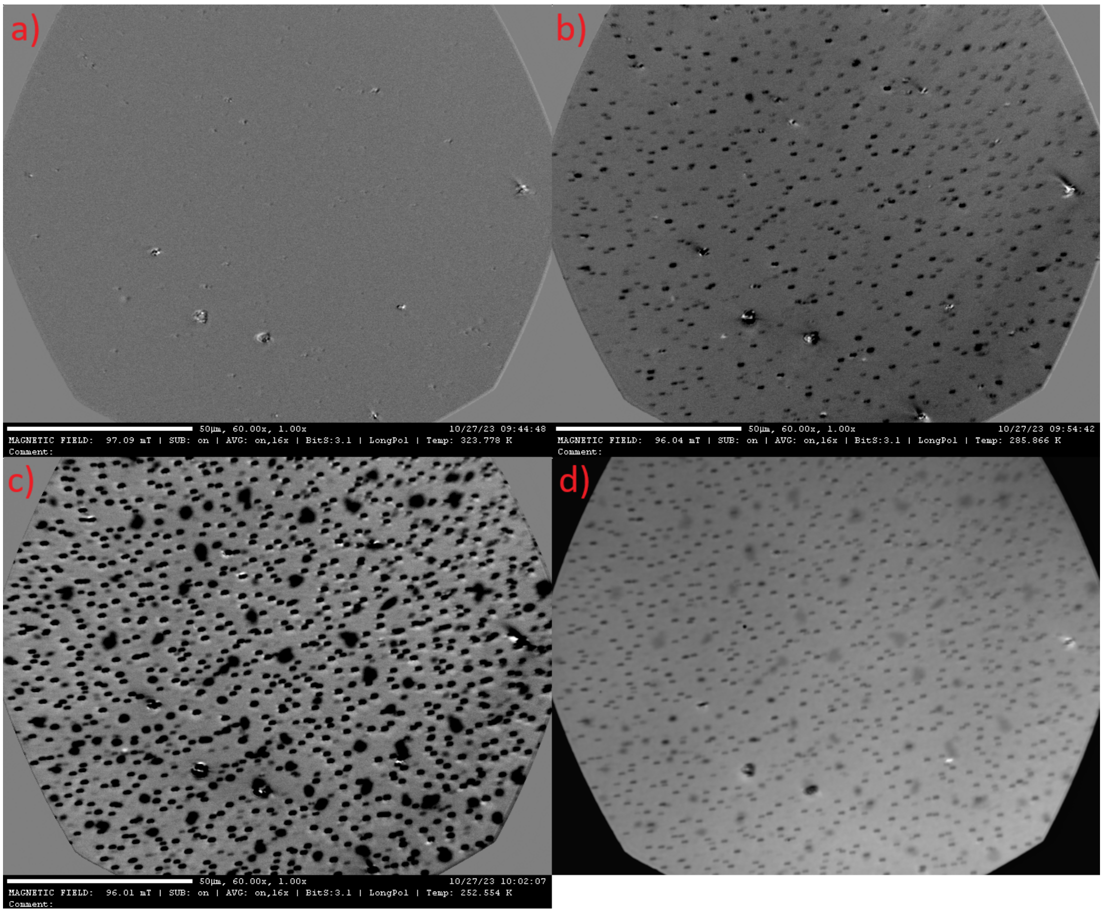

Figure 4.11 Changes in MOKE signal from Mn_3GaN sample (21-271) when cooling down across T_N with applied 100 mT out-of-plane magnetic field under blue LED illumination. The reference image was taken at 324 K. a) 234 K, b) 286 K, c) 252.5 K, d) 252.5 K without subtracting the reference image. Images were acquired using a Nikon 60x/0.85 NA Plan Fluor objective.

4.4.2 Interpretation of the results of the wide-field MOKE microscopy experiment on non-collinear antiferromagnetic and altermagnetic materials

For most of the tested samples, no significant results were observed, leaving limited scope for interpretation. Samples with rough surfaces, such as VA1530, VA1532, VA1537, MnGeSi20, and MnGeSi21 (see Tab. 2.1 for more detail), were not extensively investigated as their surface conditions rendered measurements impractical. Among the smoother samples (AB22MnSi, MnSi18, 128, and 197), no noteworthy behaviour was detected. This absence of a signal may be attributed to these samples' coercive fields being too high to be influenced by the available magnetic fields or to their polar MOKE signals being too weak to detect. Alternatively, the domains might be considerably smaller than 1 μm, falling below the resolution limit of the microscopy method, with their random orientations (a consequence of the high coercive fields) leading to an overall suppression of the MOKE signal. These explanations, however, remain speculative, as the investigation of these samples was limited by the available measurement time.

The non-collinear antiferromagnetic samples Mn_3NiN and Mn_3GaN exhibited the formation of dot-like patterns during cooling. These dots appeared and disappeared at similar temperatures in both materials, but in the case of Mn_3NiN, their appearance did not coincide with any known phase transition, such as the Néel temperature ($T_N = 250$ K). Initially, this raised suspicions that the dots could be condensation artefacts. However, this hypothesis was ruled out since the measurements were performed under vacuum conditions, and the patterns were not uniformly distributed across the surface. Furthermore, as demonstrated by the MnTe (VA1531) sample (Fig. 4.12), the non-uniform distribution of dots further supports their intrinsic origin, likely related to strain induced during cooling. This strain, amplified by the mismatch in thermal expansion coefficients between the thin films and their substrates, could create small defects detectable with the microscope.

In Mn_3GaN, additional "speckle-like" structures were observed after cooling below the Néel temperature, but insufficient time was available to investigate these features further. It remains unclear whether the speckles consistently form at the same locations or exhibit variability across cooling cycles. Although thermoscanning measurements on similar Mn_3GaN (21-270) samples did not reveal analogous structures, the differences in measurement techniques and conditions, particularly resolution and temperature range, may account for this discrepancy.

4.4.3 Experimental results on altermagnetic MnTe

The most intriguing results were obtained during measurements of the 200 nm MnTe sample (VA1531) grown on SrF_2 substrate. Cooling and heating cycles were performed around its Néel temperature ($T_N \approx 310$ K, as reported in [33]), both with and without an applied magnetic field. While the surface of the sample showed visible damage, it was still in suitable condition for measurements. During the first measurement, conducted without a magnetic field, the formation of small dots was observed around 280 K, as shown in Fig. 4.12. These dots appeared predominantly in lighter regions of the sample and were unevenly distributed across its surface, suggesting that their formation was intrinsic to the sample rather than an artefact of the measurement equipment.

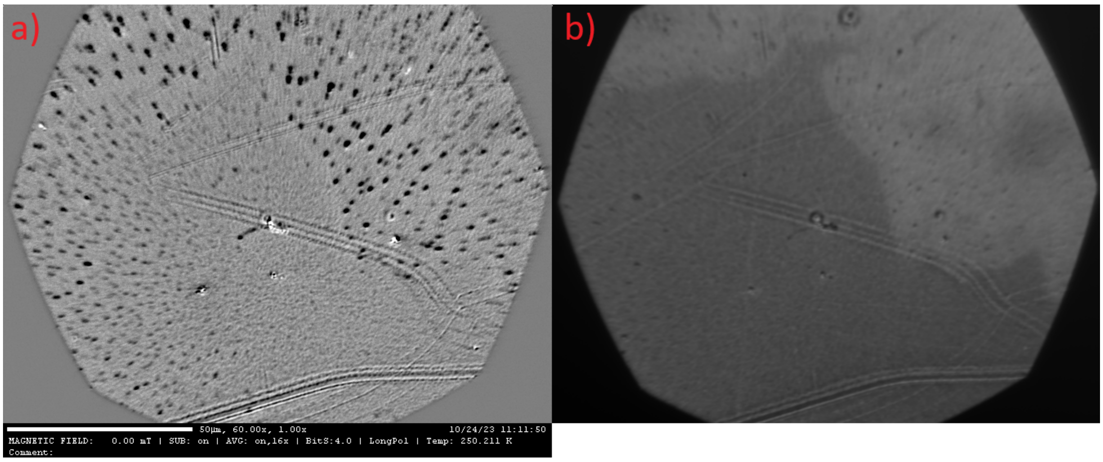

Figure 4.12 Dots formed on the MnTe (VA1531) sample after cooling down from 320 K to 150 K in no magnetic field. The images were taken at 250 K with white LEDs used for illumination in polar MOKE geometry. a) difference image (reference was taken at 320 K) b) regular image to demonstrate the inhomogeneity of the sample. Images were acquired using a Nikon 60x/0.85 NA Plan Fluor objective.

Even more remarkable results were observed during a subsequent cooldown from 320 K to 255 K in the presence of a 50 mT out-of-plane magnetic field. In this case, as illustrated in Fig. 4.13, larger areas began forming at approximately 305 K and expanded to cover most of the sample as the temperature decreased. Upon heating, these areas gradually disappeared but left behind residual changes in certain regions, which persisted even after the sample was heated to 330 K, the upper-temperature limit of the experimental setup.

Attempts to reproduce this phenomenon under identical conditions were unsuccessful. Instead, only the formation of small dot patterns, similar to those observed during the first measurement (Fig. 4.12), was detected. Additional experiments were conducted with stronger out-of-plane magnetic fields (±100 mT), in-plane magnetic fields of 300 mT, and without any applied field. Regardless of the conditions, the results consistently showed only the formation of dots, with no reappearance of the larger areas observed during the second cooldown.

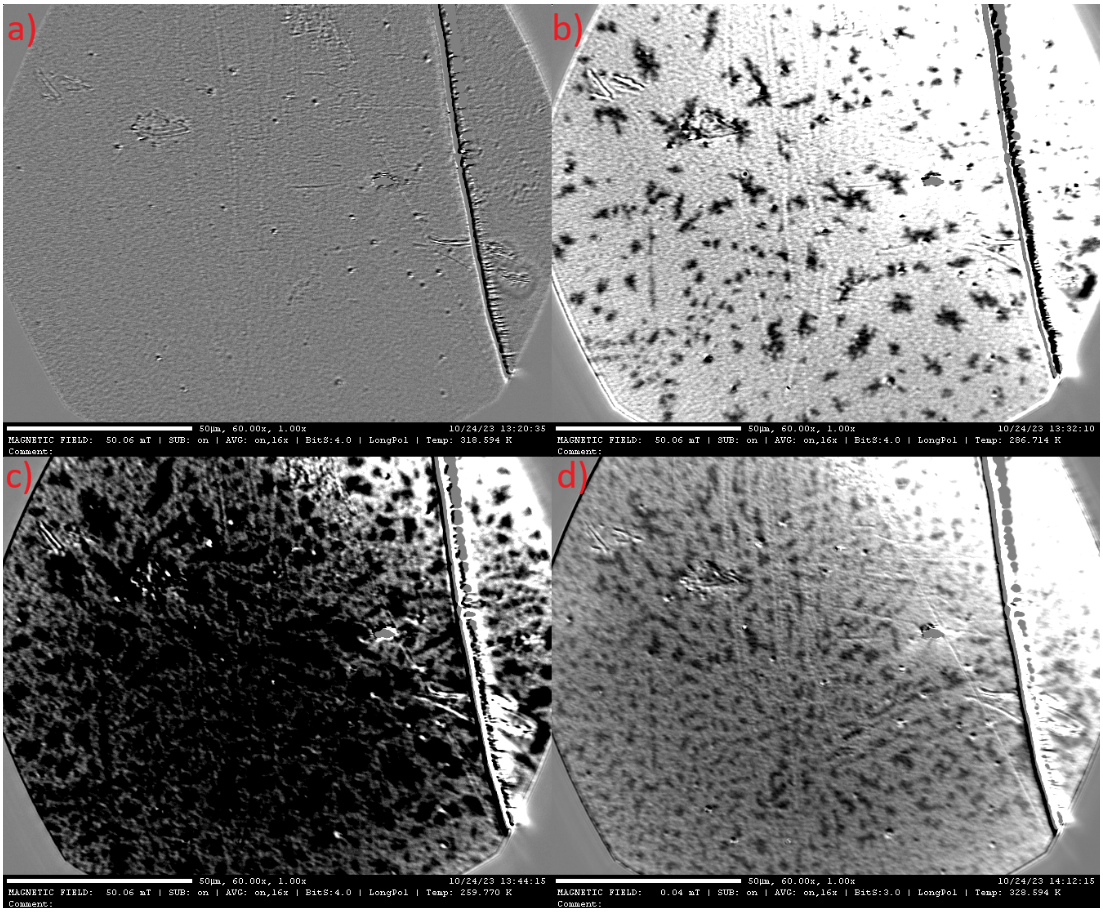

Figure 4.13 Formation and disappearance of structures on the MnTe (VA1531) sample during cooling from 320 K to 255 K and heating back to 320 K in a 50 mT out-of-plane magnetic field. Captured with blue LED illumination (polar MOKE geometry) and a Nikon 60x/0.85 NA Plan Fluor objective. a) Initial state, 318.5 K; b) structures forming, 286.5 K; c) fully developed structures, 260 K; d) residual changes after heating, 328.5 K.

Following the promising results observed on the 200 nm altermagnetic MnTe sample on SrF_2 (VA1531) and the availability of newly prepared 150 nm (VA2684) and 500 nm (VA2685) altermagnetic MnTe samples on SrF_2, the second round of MOKE measurements at IFW Dresden in February 2024 focused primarily on MnTe. Initial experiments were conducted on the thinner sample, 150 nm MnTe (VA2684), involving three cooling and heating cycles between 320 K and 250 K. One cycle was performed without an applied magnetic field, while the other two were carried out with an out-of-plane magnetic field of ±90 mT. The results are shown in Fig. 4.14.

As evident from Fig. 4.14a), the sample's surface exhibited significant irregularities, complicating the measurements. Small areas of different reflectivity (”structures”) began to form during the cooling process, appearing around 297 K and continuing to grow to at least 270 K. Due to the surface imperfections, it was challenging to determine the precise boundaries of these structures or the exact temperature at which their growth ceased. Upon reheating, all observed structures disappeared by 308 K, leaving no residual traces. Again, the rough surface made it difficult to identify the temperature at which the structures started to shrink.

No significant differences were observed among the three measurements, regardless of whether a magnetic field was applied. Unlike the earlier experiments with the older MnTe sample (VA1531), the formation of temperature-dependent structures was successfully reproduced in this thinner sample. However, due to the limitations imposed by the surface roughness, further investigation of this sample was not pursued.

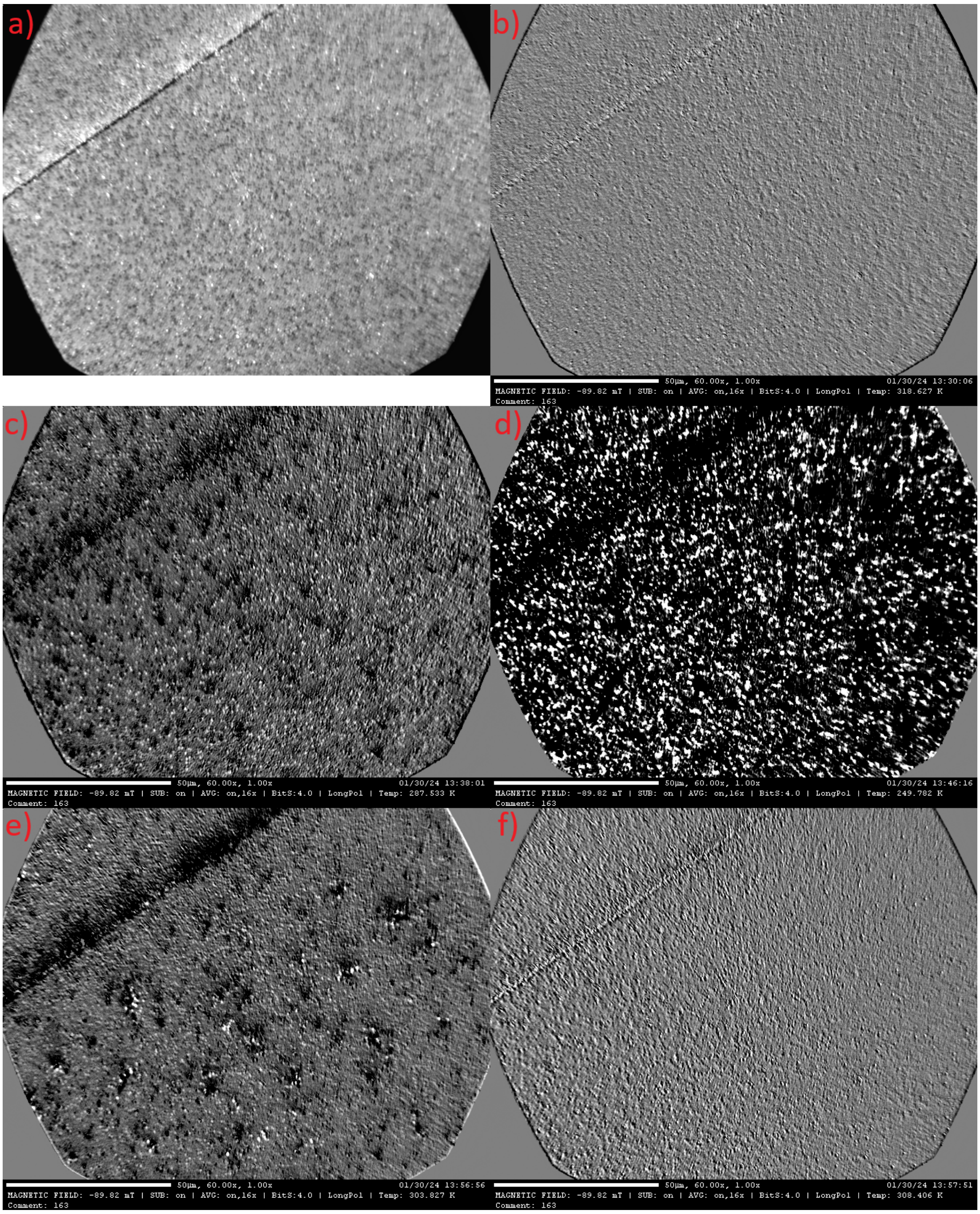

Figure 4.14 Formation and disappearance of structures on the MnTe (VA2684) sample during cooling from 320 K to 250 K and heating back to 320 K in a -90 mT out-of-plane magnetic field. Images were captured with blue LED illumination (polar MOKE sensitivity) and a Nikon 60x/0.85 NA Plan Fluor objective. a) Reference image at 318.5 K; b) initial state, 318.5 K; c) structures forming, 287.5 K; d) fully developed structures, 249.5 K; e) structures disappearing, 304 K; f) return to the initial state, 308.5 K.

Most of the experiments focused on the 500 nm MnTe sample (VA2685), where cooling and heating cycles were performed over the Néel temperature under various magnetic field conditions. Blue LED illumination provided the best contrast for these measurements, although green, red, and white LEDs were also tested. The polar MOKE sensitivity was primarily used, as it produced the sharpest images. Longitudinal and transverse MOKE geometries were also briefly explored using the configurations depicted in Figures 4.4 and 4.6. However, no differences were observed between these methods, and only polar MOKE results are presented here.

Consistent with previous observations on thinner MnTe samples, distinct patterns formed during cooling and gradually disappeared upon reheating above the Néel temperature. Figure 4.15 illustrates the formation, growth, and subsequent disappearance of these patterns during a cooling cycle in a -90 mT out-of-plane magnetic field. The figure also highlights that different patterns emerge and vanish at specific temperatures. This behaviour is further explored in Fig. 4.16, which demonstrates the hysteresis loops of these patterns, revealing distinct temperature-dependent characteristics.

Three primary patterns, labelled A, B, and C, were identified. Pattern A, the largest, first appeared around 292 K during cooling, followed by pattern B (around 278 K) and pattern C (approximately 267 K). Additionally, two types of dot-like patterns were observed: one with a halo-like structure appearing near 278 K and the other without a halo, appearing closer to 255 K. Cooling was extended to 170 K, but no further changes were detected below 250 K. Most experiments, therefore, focused on cycles between 320 K and 250 K. As shown in Fig. 4.16, all patterns disappeared before 312 K during heating, and cycles were terminated at 320 K.

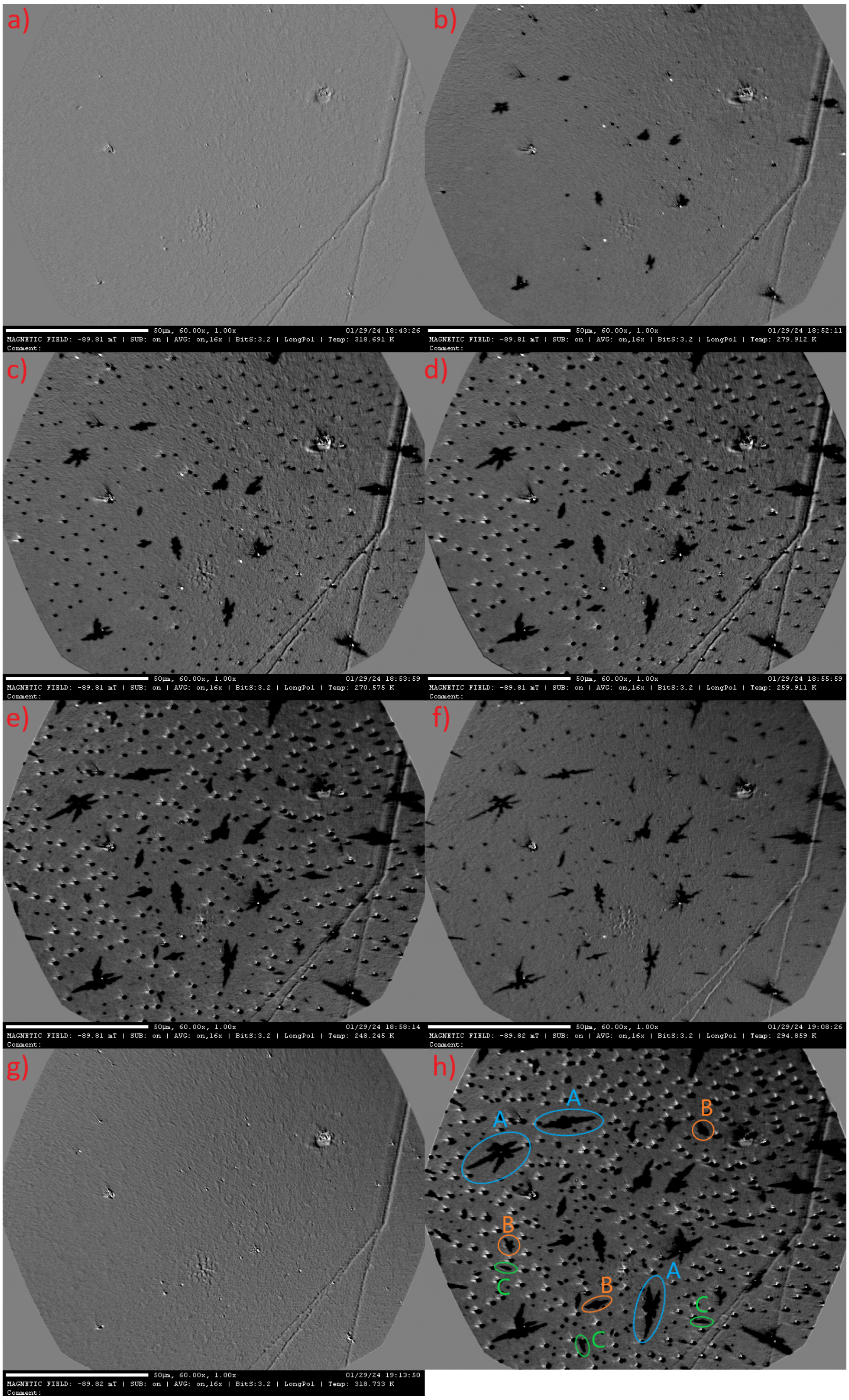

Figure 4.15 Formation and disappearance of patterns on the MnTe (VA2685) sample during cooling from 320 K to 250 K and heating back to 320 K in a -90 mT out-of-plane magnetic field. Captured with blue LED illumination (polar MOKE sensitivity) and a Nikon 60x/0.85 NA Plan Fluor objective. Reference image taken at 318.5 K. a) Initial state, 318.5 K; b) onset of pattern A, 280 K; c) onset of pattern B, 270.5 K; d) onset of pattern C, 260 K; e) fully developed patterns, 248 K; f) shrinking patterns, 295 K; g) complete disappearance, 318.5 K; h) distinct pattern types, 248 K.

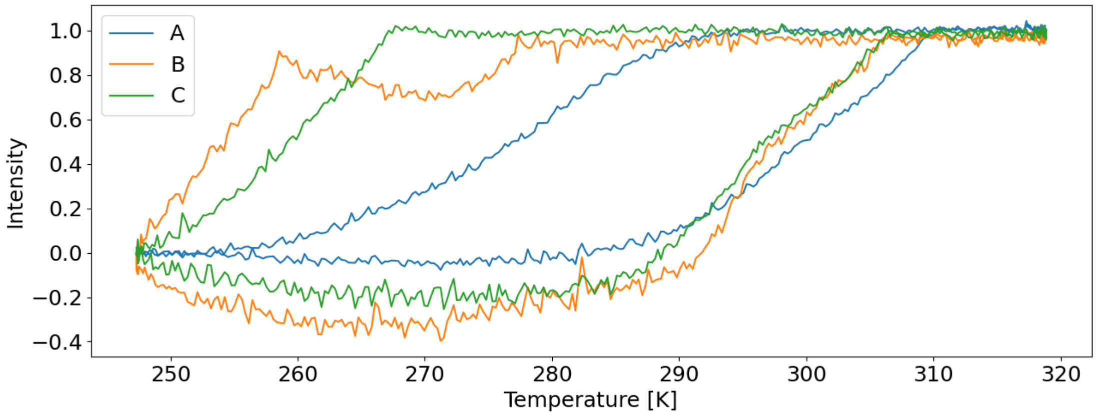

Figure 4.16 Hysteresis behaviour of the distinct patterns formed on the MnTe (VA2685) sample during cooling from 320 K to 250 K and heating back to 320 K in a -90 mT out-of-plane magnetic field. The figure highlights the differing temperature dependencies of patterns A, B, C.

The emergence of these structures was consistent regardless of the applied magnetic field or its direction. Repeated cycles with ±90 mT out-of-plane, ±300 mT in-plane magnetic fields, and no field at all revealed no directional preference in the growth of the largest structures (pattern A). Figure 4.17 compares the structures formed under these varying conditions. While the growth orientation of pattern A appeared random, it loosely followed the six-fold symmetry of the MnTe crystal lattice.

Analysis of the hysteresis behaviour revealed a subtle influence of the magnetic field on the growth dynamics of the structures. To investigate this effect, a total of fourteen cooling/heating cycles (six without a magnetic field, four with an in-plane field, and four with an out-of-plane field) were examined across two pieces of the VA2685 sample. Approximately 10 patterns A appeared during each of the cycles. When focusing on pattern A, it was observed that the hysteresis loop shifted approximately 6 K higher when the cooling and heating cycles were conducted in a magnetic field, regardless of its direction (Fig. 4.18). This analysis was based on identifying the onset and complete disappearance temperatures of the structures, offering low measurement error (approximately 0.25 K). The results were consistent across multiple measurement cycles and different regions of the sample, providing strong statistical confidence.

Despite these detailed measurements, it was not possible to compare the same region of the sample across different magnetic field orientations (in-plane versus out-of-plane) due to limitations in realigning the microscope after swapping the magnetic field coils. Figure 4.17 does, however, indicate that structures typically formed and grew from similar locations across measurements.

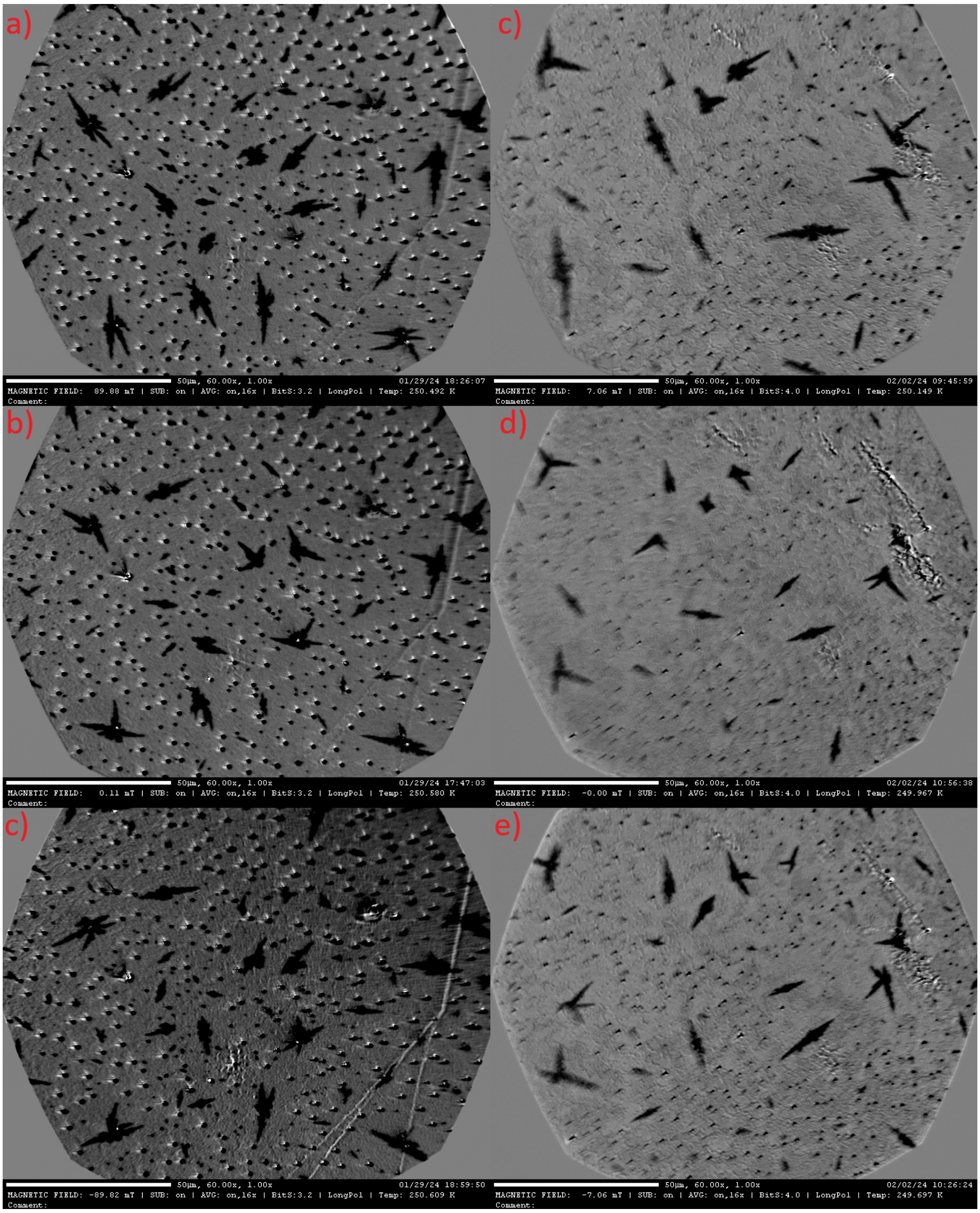

Figure 4.17 Comparison of patterns formed on the MnTe (VA2685) sample after cooling from 320 K to 250 K under various magnetic field conditions. Images were captured using blue LED illumination with polar MOKE sensitivity, and a reference image was taken at 318.5 K. a) 90 mT out-of-plane magnetic field, b) no magnetic field, c) -90 mT out-of-plane magnetic field, d) 300 mT in-plane magnetic field, e) no magnetic field, f) -300 mT in-plane magnetic field. Images were acquired using a Nikon 60x/0.85 NA Plan Fluor objective.

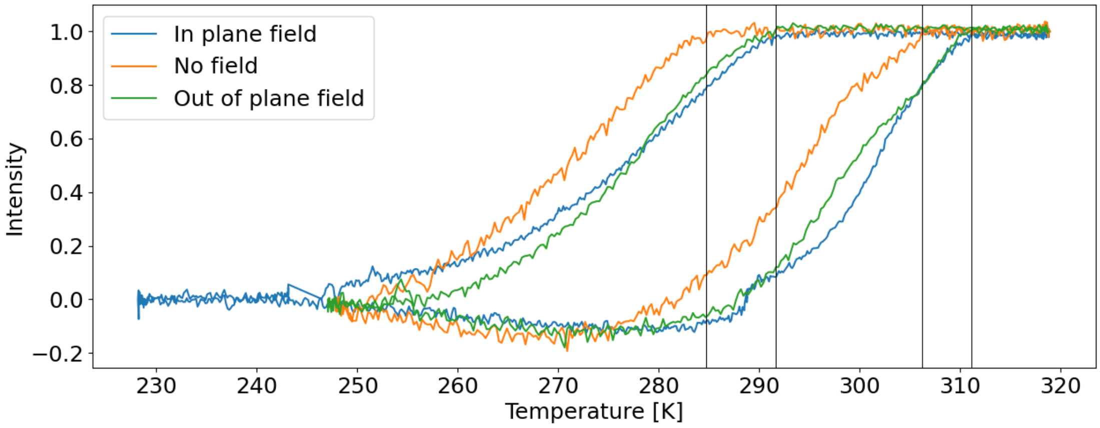

Figure 4.18 Hysteresis behaviour of pattern A formed on the MnTe (VA2685) sample during cooling from 320 K to 250 K and heating back to 320 K, comparing cycles with and without a magnetic field.

To determine whether the detected patterns originate from magneto-optical contrast, we conducted measurements with varying analyser orientations in the microscope. If the patterns had a magneto-optical basis, their contrast would reverse (from black to white and vice versa) with a change in the analyser's orientation. However, across all tested field cooling conditions, no regions exhibited such a contrast reversal, suggesting that the observed patterns were not primarily magneto-optical in nature. Additional tests were performed by rotating the in-plane magnetic field by 60° and 90° at 250 K, but again, no magnetic contrast was observed.

We also examined the effect of a compensator, which corrects ellipticity in the reflected light. Ellipticity can arise from optical imperfections, birefringence effects, or Faraday rotation in optical components, and compensators enhance sensitivity by isolating Kerr signals. However, as shown in Fig. 4.19, no significant differences were observed in the signal between 218.5 K (below the Néel temperature) and 318.5 K (above the Néel temperature). This indicates that the patterns detected using the compensator are more likely related to sample imperfections rather than magnetization. For these measurements, red, green, and blue LED illumination were tested, with red LEDs providing the best contrast.

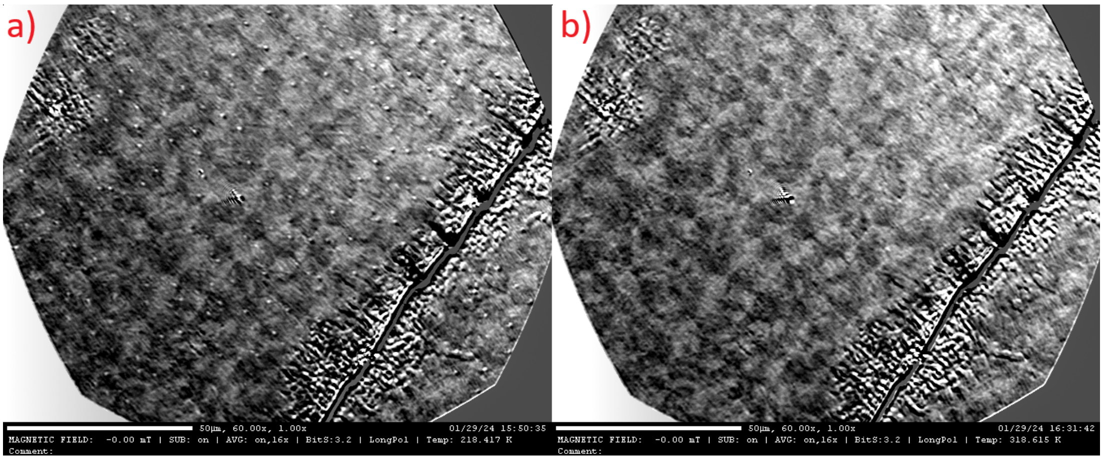

Figure 4.19 Comparison of the signal detected on the MnTe (VA2685) sample using a compensator under red LED illumination. a) 218.5 K, below the Néel temperature; b) 318.5 K, above the Néel temperature. Images were acquired using a Nikon 60x/0.85 NA Plan Fluor objective.

To further investigate the nature of the patterns, images were captured without polarization optics, first removing only the analyser and then removing both the analyser and polarizer. These measurements, taken at 250 K, are presented in Fig. 4.20. Without the analyser, the detected signal reflects surface reflectivity changes under linearly polarized light. When both the analyser and polarizer were removed, the signal represented surface reflectivity changes under unpolarised light. The patterns remained clearly visible in both cases, even without reference image subtraction. Larger patterns (A, B, and C) exhibited distinct reflectivity levels, appearing grey, while the dot-like structures appeared black. Interestingly, the largest patterns (A) often originated around central dots, whereas smaller patterns (C) tended to form away from these dots.

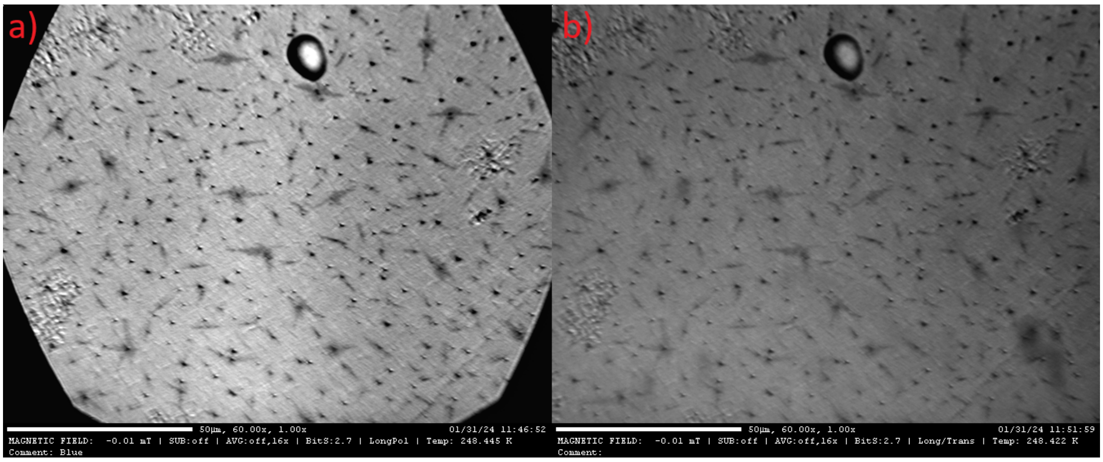

Figure 4.20 Signal detected on the MnTe (VA2685) sample without polarization optics at 248.5 K under blue LED illumination. a) Without analyser; b) without both analyser and polarizer. Images were acquired using a Nikon 60x/0.85 NA Plan Fluor objective.

To confirm that the observed patterns were not peculiarities of the specific MnTe samples grown on SrF_2 substrates, an ultra-thin MnTe film (< 20 nm) grown on InP by Peter Wadley's team at the University of Nottingham was also investigated. These measurements were performed by Ivan Soldatov at IFW Dresden and are included here for comparison. Figure 4.21, compares the MnTe sample grown on SrF_2 and the one grown on InP under identical conditions: at 266.5 K, in a 300 mT in-plane magnetic field, using blue LED illumination, polar MOKE sensitivity and 60x magnification. The InP sample exhibited a smoother surface but displayed similar patterns to those observed in the SrF_2-based samples. Although the patterns in the InP sample were smaller, the same three larger patterns (A, B, C) and two types of dots were identified. According to Dr. Soldatov, the behaviour of the InP sample closely resembled that of the SrF_2-based samples, with patterns appearing in the same locations during repeated measurements and their orientation showing no correlation with the applied magnetic field direction.

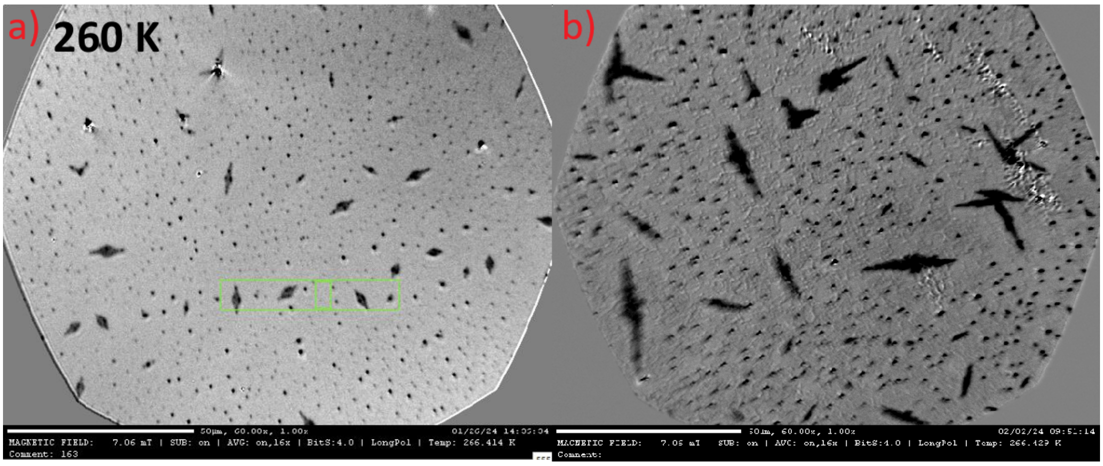

Figure 4.21 Comparison of MnTe samples grown on different substrates under identical conditions (266.5 K, 300 mT in-plane magnetic field, blue LED illumination, polar MOKE sensitivity, 60x magnification). a) thin-film (<20 nm) sample grown on InP (image taken by Ivan Soldatov), b) 500 nm sample grown on SrF_2. Images were acquired using a Nikon 60x/0.85 NA Plan Fluor objective.

4.4.4 Interpretation of the results of the wide-field MOKE microscopy experiment on altermagnetic MnTe

The MnTe sample VA1531 presented intriguing results during the first measurement cycle, with patterns forming on the surface during cooling in an applied magnetic field. These patterns were not observed in subsequent cycles, even under identical conditions, suggesting they may be related to the virgin state of the sample. It is plausible that the patterns resulted from the initial application of a magnetic field disturbing the sample's previously unset state. However, the degradation of the uncapped sample, which had been stored without adequate protection, cannot be excluded as a contributing factor.

The newly prepared MnTe samples (VA2684 and VA2685) offered improved opportunities for investigation. While the thinner VA2684 sample exhibited a rougher surface, it still demonstrated the same formation of patterns as the old sample (VA1531). These patterns were reproducible and appeared irrespective of the applied magnetic field. The 500 nm MnTe sample (VA2685), with its smoother surface, became the primary focus of the measurements.

In the VA2685 sample, three distinct patterns of different contrast (A, B, and C) and varying sizes were observed, each displaying unique hysteresis behaviour. Additionally, two types of dot-like patterns with slightly different sizes and hysteresis characteristics were identified. These patterns appeared consistently during cooling, disappearing upon reheating above the Néel temperature, and were independent of external magnetic field application. However, the contrast of the patterns showed hysteretic behaviour upon temperature sweeps, with the hysteresis loops shifting with the application of a magnetic field, indicating a certain relation to magnetism, possibly by means of magnetostriction. Despite this, the patterns were determined not to be of magneto-optical contrast, as they remained visible even without polarization optics, suggesting they are caused instead by local changes in reflectivity.

One plausible explanation for the pattern formation is a strain within the sample, arising from the differing thermal expansion coefficients of the MnTe thin film and the SrF_2 substrate. This phenomenon was previously explored in [69], where cracks were observed in MnTe thin films grown on SiO_2/Si substrates after multiple thermal cycles. However, the patterns in this study differ in scale and are fully reversible upon reheating above the Néel temperature. It is hypothesized that the dot-like patterns may be linked to strain-induced defects or grains, as their distinct reflectivity sets them apart from the larger patterns. Future experiments are planned to test this hypothesis by thermally cycling samples attached to Si or silica plates, which have differing thermal expansion coefficients [70] compared to SrF_2. Significant differences in pattern formation under these conditions would strengthen the case for strain as the primary cause.

Another possible explanation for the dots is their being inclusions or telluride precipitates. Similar-sized dots (0.5 - 2 μm) were previously observed in MnTe prepared by the travelling heater method [71]. Comparable Te-related features have also been reported in CdTe [72], including six-fold symmetry structures akin to those observed in the largest patterns (A) in this study.

The rate of cooling and heating appears to influence the pattern formation, particularly the size and growth of the observed structures. As shown in the hysteresis graph (Fig. 4.16), some patterns (e.g., B and C) continued growing even as the sample was reheated. All measurements in this study were conducted with a cooling and heating rate of 5 K per minute, which may have been too rapid for complete pattern formation. Future experiments with varied cooling rates could provide additional insights.

Preliminary Raman spectroscopy measurements performed by Irena Matulková (from the Faculty of Science of Charles University) on the VA2684 and VA2685 samples support the hypothesis of Te precipitates and $MnTe_2$ formation. After the Al_2O_3 coating was removed, Raman spectra revealed features consistent with these compounds, showing dependence on both the position of the sample and temperature. While these findings require further study, they suggest that the observed patterns could correspond to Te precipitates and $MnTe_2$ phases that form and dissolve with temperature changes.

Temperature-dependent X-ray diffraction (XRD) measurements could provide additional confirmation. While room-temperature XRD measurements have demonstrated excellent MnTe crystal quality, no XRD data exists for these samples at lower temperatures. Such experiments could explain structural changes correlating with the observed patterns.

Similar patterns were also observed in MnTe samples grown on InP substrates by Peter Wadley's team at the University of Nottingham, as shown in Fig. 4.21. These patterns, also unrelated to magneto-optical contrast, suggest that the behaviour is not specific to SrF_2-based samples but may be a general feature of MnTe thin films. The smoother surface of the InP sample allowed for clearer imaging, though the patterns were smaller in size compared to those in SrF_2-based samples. Patterns in the InP sample consistently appeared in the same locations during repeated measurements, further underscoring the reproducibility of this phenomenon.

Recent studies have successfully demonstrated the imaging of altermagnetic domains in MnTe using XMLD-PEEM and XMCD-PEEM techniques [66]. These experiments revealed six-fold symmetric domains, with sizes as small as μm, particularly in hexagon-shaped patterned MnTe samples grown on InP. This domain size is close to the resolution limit of the wide-field Kerr microscope, which is approximately 300 nm. Larger domains, reaching up to 10 μm, were observed in unfilled hexagon-shaped patterns, where the domain size corresponded to the length of the hexagon's sides. These larger domains fall well within the capabilities of Kerr microscopy, presenting a promising opportunity for further investigations.

To date, however, altermagnetic domains have not been imaged in unpatterned MnTe samples. Investigating patterned MnTe samples using the wide-field Kerr microscope could provide valuable insights, particularly since the patterned samples originate from the same Nottingham facility as the MnTe sample on InP (shown in Fig. 4.21). These patterned samples, featuring hexagonal geometries, are especially relevant because they exhibit domain sizes that are more compatible with the resolution limits of the Kerr microscope.

One of the possible reasons why the MOKE microscopy in MnTe remains challenging is the size of the magneto-optical effects. Recent spectroscopy measurements [73] on MnTe thin films grown on InP have reported polar Kerr rotations of approximately 1–1.5 mdeg under experimental conditions similar to those used in the present study (illumination with blue (455 ± 13 nm), green (520 ± 16 nm), and red light (632 ± 9 nm), and magnetic fields up to 300 mT). This magnitude of Kerr rotation approaches the lower sensitivity threshold of the Kerr microscope, which, for samples with ideal surfaces, is thought to be approximately 0.6 mdeg.

These small Kerr rotations suggest that unpatterned MnTe thin films may exhibit a multidomain state with domains as small as 20 nm [47]. Such domain sizes are significantly below the resolution capabilities of a wide-field Kerr microscope. Consequently, while imaging altermagnetic domains in unpatterned MnTe samples may not be feasible with this technique, future experiments targeting patterned MnTe samples with larger domain sizes hold significant potential for advancing the understanding of altermagnetic phenomena in these materials.

Conclusion

This thesis aimed to explore the imaging of magnetic domains in non-collinear antiferromagnetic and altermagnetic materials using thermoscanning (STGM) and wide-field MOKE microscopy. While multiple sample types were investigated, the primary focus was placed on non-collinear antiferromagnet Mn_3GaN for thermoscanning (STGM) and altermagnetic MnTe for wide-field MOKE microscopy.

The thermoscanning (STGM) experiments on non-collinear antiferromagnet Mn_3GaN provided valuable insights despite the absence of definitive magnetic domain signals. The thermovoltage measurements remained unaffected by applied magnetic fields or transitions through the Néel temperature. Instead, the detected signals scaled with laser intensity and reversed sign between 140 K and 296 K, strongly suggesting a dominant contribution from the Seebeck effect. Structural or compositional irregularities within the sample, such as grains or defects, are likely responsible for localized thermal gradients that do not cancel out, thereby generating the observed signals. The lack of an anomalous Nernst effect (ANE) signal supports the conclusion that the Mn_3GaN sample is in the Γ_{5g} phase, where mirror symmetries suppress Berry curvature contributions. Future work could focus on direct measurements of the Seebeck coefficient in Mn_3GaN to verify these findings.

Similar attempts were made to apply the thermoscanning experiment to the altermagnetic MnTe, but these efforts were inconclusive due to issues with bonding, which prevented meaningful measurements. After resolving the bonding issues, thermoscanning on MnTe remains a promising subject for future investigation. Refining the thermoscanning setup to improve stability at intermediate temperatures and minimize sample drift could enable higher-resolution studies, potentially uncovering finer-scale thermal or magnetic phenomena.

The application of wide-field MOKE microscopy to altermagnetic MnTe produced contrasting results. While most samples exhibited no apparent magneto-optical activity, the 500 nm MnTe sample grown on SrF_2 (VA2685) revealed intriguing, reproducible patterns during thermal cycling. These patterns, which disappeared above the Néel temperature, were attributed to strain-induced reflectivity changes rather than intrinsic magneto-optical signals. A comparison between layers grown on different substrates suggests that the strain could arise from mismatched thermal expansion coefficients between the MnTe thin film and its SrF_2 substrate. Preliminary Raman spectroscopy results and comparisons with MnTe samples grown on an alternative substrate (InP) support the hypothesis that various structural defects can occur, possibly due to strain. These can be telluride precipitates, $MnTe_2$ phases or strain-induced defects. The exact identification of these patterns requires a more detailed interpretation of the Raman spectra alongside further planned Raman experiments. Additional investigation involving different thermal cycling rates, alternative substrates (SrF_2 and InP), and complementary techniques such as temperature-dependent X-ray diffraction and advanced Raman spectroscopy could provide deeper insights into the origin of these patterns and their relation to the sample's structural properties.

Another exciting direction stems from recent XMLD-PEEM and XMCD-PEEM study [66], which successfully imaged altermagnetic domains in patterned

MnTe samples. These studies revealed domain sizes within the resolution limits of wide-field MOKE microscopy, suggesting that patterned samples with hexagonal geometries or tailored designs could enable the visualization of altermagnetic domains using this technique. Such investigations would enhance the understanding of the magnetic domain structures of altermagnets.

In conclusion, this thesis contributes to the understanding of imaging magnetic ordering in non-collinear antiferromagnetic and altermagnetic materials. While magnetic domain structures in $\mathrm{Mn_3GaN}$ and MnTe were not conclusively identified under the conditions employed, the results establish a foundation for future studies. The combination of thermoscanning and wide-field MOKE microscopy offers complementary approaches for probing thermal and optical properties in these materials. By incorporating optimized experimental setups, patterned samples, and advanced spectroscopic techniques, future research can further investigate the interplay between magnetic ordering, structural effects, and thermal properties, unlocking new insights into these complex and promising materials.

Bibliography

1. Wolf, S. A. et al. Spintronics: A Spin-Based Electronics Vision for the Future. *Science* [online]. 2001, vol. 294, no. 5546, pp. 1488–1495 [visited on 2024-12-27]. Available from DOI: `10.1126/science.1065389`. Publisher: American Association for the Advancement of Science.
2. Šmejkal, L.; Sinova, J.; Jungwirth, T. Beyond Conventional Ferromagnetism and Antiferromagnetism: A Phase with Nonrelativistic Spin and Crystal Rotation Symmetry. *Physical Review X* [online]. 2022, vol. 12, no. 3, p. 031042 [visited on 2024-11-10]. Available from DOI: `10.1103/PhysRevX.12.031042`. Publisher: American Physical Society.
3. Jungwirth, T. et al. The multiple directions of antiferromagnetic spintronics. *Nature Physics* [online]. 2018, vol. 14, no. 3, pp. 200–203 [visited on 2024-12-27]. ISSN 1745-2481. Available from DOI: `10.1038/s41567-018-0063-6`. Publisher: Nature Publishing Group.
4. Johnson, F. et al. Identifying the octupole antiferromagnetic domain orientation in Mn 3 NiN by scanning anomalous Nernst effect microscopy. *Applied Physics Letters*. 2022, vol. 120, p. 232402. Available from DOI: `10.1063/5.0091257`.
5. Reichlova, H. et al. Imaging and writing magnetic domains in the noncollinear antiferromagnet Mn3Sn. *Nature Communications* [online]. 2019, vol. 10, no. 1, p. 5459 [visited on 2024-10-10]. ISSN 2041-1723. Available from DOI: `10.1038/s41467-019-13391-z`. Publisher: Nature Publishing Group.
6. Šmejkal, L.; Sinova, J.; Jungwirth, T. Emerging Research Landscape of Altermagnetism. *Physical Review X* [online]. 2022, vol. 12, no. 4, p. 040501 [visited on 2024-11-10]. Available from DOI: `10.1103/PhysRevX.12.040501`. Publisher: American Physical Society.
7. Soldatov, I.; Schäfer, R. *Selective sensitivity in Kerr microscopy* [online]. arXiv, 2016 [visited on 2024-11-27]. No. arXiv:1612.02027. Available from DOI: `10.48550/arXiv.1612.02027`.
8. Coey, J. M. D. *Magnetism and magnetic materials*. Cambridge New York: Cambridge University Press, 2009. ISBN 978-0-511-67743-4 978-0-511-68515-6 978-0-511-68192-9 978-0-511-67994-0 978-0-511-84500-0.
9. Kittel, C. *Introduction to solid state physics*. 8th ed. Hoboken, NJ: Wiley, 2005. ISBN 978-0-471-41526-8.
10. Blundell, S. *Magnetism in condensed matter*. Reprint. Oxford: Oxford Univ. Press, 2014. Oxford master series in condensed matter physics, no. 4. ISBN 978-0-19-850591-4.
11. Dirac, P. A. M. The Quantum Theory of the Electron. *Proceedings of the Royal Society of London. Series A, Containing Papers of a Mathematical and Physical Character* [online]. 1928, vol. 117, no. 778, pp. 610–624 [visited on 2024-11-09]. ISSN 0950-1207. Available from: `https://www.jstor.org/stable/94981`. Publisher: Royal Society.

12. Ruderman, M. A.; Kittel, C. Indirect Exchange Coupling of Nuclear Magnetic Moments by Conduction Electrons. *Physical Review* [online]. 1954, vol. 96, no. 1, pp. 99–102 [visited on 2024-11-09]. Available from DOI: `10.1103/PhysRev.96.99`. Publisher: American Physical Society.

13. Collins, M.; Petrenko, O. Triangular antiferromagnets. Can J Phys 75:605. *Canadian Journal of Physics*. 1997, vol. 75, p. 605. Available from DOI: `10.1139/p97-007`.

14. Gurung, G.; Shao, D.-F.; Paudel, T. R.; Tsymbal, E. Y. Anomalous Hall conductivity of noncollinear magnetic antiperovskites. *Physical Review Materials* [online]. 2019, vol. 3, no. 4, p. 044409 [visited on 2024-11-10]. Available from DOI: `10.1103/PhysRevMaterials.3.044409`. Publisher: American Physical Society.

15. Boldrin, D. et al. Anomalous Hall effect in noncollinear antiferromagnetic ${\mathrm{Mn}}_{3}\mathrm{NiN}$ thin films. *Physical Review Materials* [online]. 2019, vol. 3, no. 9, p. 094409 [visited on 2024-11-10]. Available from DOI: `10.1103/PhysRevMaterials.3.094409`. Publisher: American Physical Society.

16. Jungwirth, T.; Šmejkal, L.; Sinova, J. *Altermagnetism: spin-momentum locked phase protected by non-relativistic symmetries*. 2021. Available from DOI: `10.21203/rs.3.rs-956878/v1`.

17. Feng, Z. et al. An anomalous Hall effect in altermagnetic ruthenium dioxide. *Nature Electronics* [online]. 2022, vol. 5, no. 11, pp. 735–743 [visited on 2024-11-10]. ISSN 2520-1131. Available from DOI: `10.1038/s41928-022-00866-z`. Publisher: Nature Publishing Group.

18. Zhou, X. et al. Crystal Thermal Transport in Altermagnetic ${\mathrm{RuO}}_{2}$ *Physical Review Letters* [online]. 2024, vol. 132, no. 5, p. 056701 [visited on 2024-11-10]. Available from DOI: `10.1103/PhysRevLett.132.056701`. Publisher: American Physical Society.

19. Šmejkal, L. et al. Giant and Tunneling Magnetoresistance in Unconventional Collinear Antiferromagnets with Nonrelativistic Spin-Momentum Coupling. *Physical Review X* [online]. 2022, vol. 12, no. 1, p. 011028 [visited on 2024-11-10]. Available from DOI: `10.1103/PhysRevX.12.011028`. Publisher: American Physical Society.

20. Gonzalez Betancourt, R. D. et al. Spontaneous Anomalous Hall Effect Arising from an Unconventional Compensated Magnetic Phase in a Semiconductor. *Physical Review Letters* [online]. 2023, vol. 130, no. 3, p. 036702 [visited on 2024-11-11]. Available from DOI: `10.1103/PhysRevLett.130.036702`. Publisher: American Physical Society.

21. Sürgers, C. et al. Anomalous Nernst effect in the noncollinear antiferromagnet Mn5Si3. *Communications Materials* [online]. 2024, vol. 5, no. 1, pp. 1–9 [visited on 2025-01-07]. ISSN 2662-4443. Available from DOI: `10.1038/s43246-024-00617-x`. Publisher: Nature Publishing Group.

22. Beckert, S. et al. Anomalous Nernst effect in ${\mathrm{Mn}}_{3}\mathrm{NiN}$ thin films. *Physical Review B* [online]. 2023, vol. 108, no. 2, p. 024420 [visited on 2024-10-10]. Available from DOI: `10.1103/PhysRevB.108.024420`. Publisher: American Physical Society.
23. Zeng, C. et al. Epitaxial ferromagnetic Mn5Ge3 on Ge(111). *Applied Physics Letters* [online]. 2003, vol. 83, no. 24, pp. 5002–5004 [visited on 2024-11-12]. ISSN 0003-6951. Available from DOI: `10.1063/1.1633684`.
24. Mazin, I. I. Altermagnetism in MnTe: Origin, predicted manifestations, and routes to detwinning. *Physical Review B* [online]. 2023, vol. 107, no. 10, p. L100418 [visited on 2024-11-11]. Available from DOI: `10.1103/PhysRevB.107.L100418`. Publisher: American Physical Society.
25. Krempaský, J. et al. Altermagnetic lifting of Kramers spin degeneracy. *Nature*. 2024, vol. 626, no. 7999, pp. 517–522. ISSN 1476-4687. Available from DOI: `10.1038/s41586-023-06907-7`.
26. Szwacki, N. et al. Structural properties of MnTe, ZnTe, and ZnMnTe. *Acta Physica Polonica A*. 2004, vol. 106, p. 233. Available from DOI: `10.12693/APhysPolA.106.233`.
27. Schlesinger, M. E. The Mn-Te (manganese-tellurium) system. *Journal of Phase Equilibria* [online]. 1998, vol. 19, no. 6, pp. 591–596 [visited on 2024-11-11]. ISSN 1054-9714. Available from DOI: `10.1361/105497198770341806`
28. Mori, S. et al. Thermal stress control of the polymorphic transformation in MnTe semiconductor films. *Materialia* [online]. 2022, vol. 24, p. 101493 [visited on 2024-11-11]. ISSN 2589-1529. Available from DOI: `10.1016/j.mtla.2022.101493`.
29. Siol, S. et al. Stabilization of wide band-gap p-type wurtzite MnTe thin films on amorphous substrates. *Journal of Materials Chemistry C* [online]. 2018, vol. 6, no. 23, pp. 6297–6304 [visited on 2024-11-11]. ISSN 2050-7534. Available from DOI: `10.1039/C8TC01828F`. Publisher: The Royal Society of Chemistry.
30. Mu, S. et al. Phonons, magnons, and lattice thermal transport in antiferromagnetic semiconductor MnTe. *Physical Review Materials* [online]. 2019, vol. 3, no. 2, p. 025403 [visited on 2024-11-11]. Available from DOI: `10.1103/PhysRevMaterials.3.025403`. Publisher: American Physical Society.
31. Bossini, D. et al. Exchange-mediated magnetic blue-shift of the band-gap energy in the antiferromagnetic semiconductor MnTe. *New Journal of Physics* [online]. 2020, vol. 22, no. 8, p. 083029 [visited on 2024-11-11]. ISSN 1367-2630. Available from DOI: `10.1088/1367-2630/aba0e7`. Publisher: IOP Publishing.
32. Yin, G. et al. Planar Hall Effect in Antiferromagnetic MnTe Thin Films. *Physical Review Letters* [online]. 2019, vol. 122, no. 10, p. 106602 [visited on 2024-11-11]. Available from DOI: `10.1103/PhysRevLett.122.106602`. Publisher: American Physical Society.

33. Kriegner, D. et al. Magnetic anisotropy in antiferromagnetic hexagonal MnTe. *Physical Review B* [online]. 2017, vol. 96, no. 21, p. 214418 [visited on 2024-11-11]. Available from DOI: `10.1103/PhysRevB.96.214418`. Publisher: American Physical Society.

34. Quintela, C. X. et al. Epitaxial antiperovskite/perovskite heterostructures for materials design. *Science Advances* [online]. 2020, vol. 6, no. 30, eaba4017 [visited on 2024-11-10]. Available from DOI: `10.1126/sciadv.aba4017`. Publisher: American Association for the Advancement of Science.

35. Wang, J. et al. A new noncollinear triangle antiferromagnetic phase in Mn3GaN by Cr doping. *Materials Today Physics* [online]. 2024, vol. 42, p. 101362 [visited on 2024-10-10]. ISSN 2542-5293. Available from DOI: `10.1016/j.mtphys.2024.101362`.

36. Samathrakis, I.; Zhang, H. Tailoring the anomalous Hall effect in the noncollinear antiperovskite Mn 3 GaN. *Physical Review B* [online]. 2020, vol. 101, no. 21, p. 214423 [visited on 2024-11-07]. ISSN 2469-9950, ISSN 2469-9969. Available from DOI: `10.1103/PhysRevB.101.214423`.

37. Sürgers, C. et al. *Optimization of reactively sputtered Mn3GaN films based on resistivity measurements* [online]. arXiv, 2024 [visited on 2024-10-31]. No. arXiv:2405.01203. Available from arXiv: `2405.01203`. version: 1.

38. Nan, T. et al. Controlling spin current polarization through non-collinear antiferromagnetism. *Nature Communications* [online]. 2020, vol. 11, no. 1, p. 4671 [visited on 2024-10-10]. ISSN 2041-1723. Available from DOI: `10.1038/s41467-020-17999-4`. Publisher: Nature Publishing Group.

39. Xiao, D.; Chang, M.-C.; Niu, Q. Berry phase effects on electronic properties. *Reviews of Modern Physics* [online]. 2010, vol. 82, no. 3, pp. 1959–2007 [visited on 2024-11-14]. ISSN 0034-6861, ISSN 1539-0756. Available from DOI: `10.1103/RevModPhys.82.1959`.

40. Xiao, D.; Yao, Y.; Fang, Z.; Niu, Q. Berry-Phase Effect in Anomalous Thermoelectric Transport. *Physical Review Letters* [online]. 2006, vol. 97, no. 2, p. 026603 [visited on 2024-11-13]. Available from DOI: `10.1103/PhysRevLett.97.026603`. Publisher: American Physical Society.

41. Weng, H.; Dai, X.; Fang, Z. From Anomalous Hall Effect to the Quantum Anomalous Hall Effect. 2015.

42. Breidenbach, A. T. et al. Anomalous Nernst and Seebeck coefficients in epitaxial thin film ${\mathrm{Co}}_{2}{\mathrm{MnAl}}_{x}{\mathrm{Si}}_{1\ensuremath{-}x}$ and ${\mathrm{Co}}_{2}\mathrm{FeAl}$. *Physical Review B* [online]. 2022, vol. 105, no. 14, p. 144405 [visited on 2024-11-14]. Available from DOI: `10.1103/PhysRevB.105.144405`. Publisher: American Physical Society.

43. Noguchi, S. et al. Bipolarity of large anomalous Nernst effect in Weyl magnet-based alloy films. *Nature Physics* [online]. 2024, vol. 20, no. 2, pp. 254–260 [visited on 2024-11-15]. ISSN 1745-2481. Available from DOI: `10.1038/s41567-023-02293-z`. Publisher: Nature Publishing Group.

44. Devaraj, N.; Bose, A.; Narayan, A. Interplay of altermagnetism and pressure in hexagonal and orthorhombic MnTe. *Physical Review Materials* [online]. 2024, vol. 8, no. 10, p. 104407 [visited on 2024-11-13]. ISSN 2475-9953. Available from DOI: `10.1103/PhysRevMaterials.8.104407`.

45. Zhou, X. et al. Giant anomalous Nernst effect in noncollinear antiferromagnetic Mn-based antiperovskite nitrides. *Physical Review Materials* [online]. 2020, vol. 4, no. 2, p. 024408 [visited on 2024-11-13]. Available from DOI: `10.1103/PhysRevMaterials.4.024408`. Publisher: American Physical Society.

46. Hovořáková, K. Studium magnetické anizotropie tenkých vrstev feromagnetů pomocí optických metod [online]. 2019 [visited on 2025-01-06]. Available from: `https://dspace.cuni.cz/handle/20.500.11956/109962`. Accepted: 2021-03-25T22:13:49Z Publisher: Univerzita Karlova, Matematicko-fyzikální fakulta.

47. Kriegner, D. et al. *Multiple-stable anisotropic magnetoresistance memory in antiferromagnetic MnTe* [online]. arXiv, 2015 [visited on 2024-11-28]. No. arXiv:1508.04877. Available from DOI: `10.48550/arXiv.1508.04877`.

48. Nerodilová, M. Ultrarychlá laserová spektroskopie nekolineárních antiferomagnetů [online]. 2024 [visited on 2024-11-28]. Available from: `https://dspace.cuni.cz/handle/20.500.11956/191176`. Accepted: 2024-07-09T06:47:45Z Publisher: Univerzita Karlova, Matematicko-fyzikální fakulta.

49. Fruchart, D.; F. Bertaut, E. Magnetic Studies of the Metallic Perovskite-Type Compounds of Manganese. *Journal of the Physical Society of Japan* [online]. 1978, vol. 44, no. 3, pp. 781–791 [visited on 2024-11-28]. ISSN 0031-9015. Available from DOI: `10.1143/JPSJ.44.781`. Publisher: The Physical Society of Japan.

50. Shi, K. et al. Baromagnetic Effect in Antiperovskite Mn3Ga0.95N0.94 by Neutron Powder Diffraction Analysis. *Advanced Materials* [online]. 2016, vol. 28, no. 19, pp. 3761–3767 [visited on 2024-11-19]. ISSN 1521-4095. Available from DOI: `10.1002/adma.201600310`. _eprint: https://onlinelibrary.wiley.com/doi/pdf/10.1002/adma.201600310.

51. Hellenes, A. B. et al. *P-wave magnets* [online]. arXiv, 2024 [visited on 2024-11-28]. No. arXiv:2309.01607. Available from DOI: `10.48550/arXiv.2309.01607`.

52. Alaoui, Y. C. et al. A large magnetocaloric effect and thermoelectric properties of anti-perovskite SnMn3N material: a DFT study and monte carlo simulation. *Physica Scripta* [online]. 2023, vol. 98, no. 9, p. 095942 [visited on 2024-11-19]. ISSN 1402-4896. Available from DOI: `10.1088/1402-4896/acf079`. Publisher: IOP Publishing.

53. Tan, S. et al. An antiperovskite compound with multifunctional properties: Mn3PdN. *Journal of Solid State Chemistry* [online]. 2021, vol. 302, p. 122389 [visited on 2024-11-19]. ISSN 0022-4596. Available from DOI: `10.1016/j.jssc.2021.122389`.

54. McCord, J. Progress in magnetic domain observation by advanced magneto-optical microscopy. *Journal of Physics D: Applied Physics* [online]. 2015, vol. 48, no. 33, p. 333001 [visited on 2024-10-10]. ISSN 0022-3727. Available from DOI: `10.1088/0022-3727/48/33/333001`. Publisher: IOP Publishing.

55. Šubrt, J. Dynamika spinové polarizace ve ferromagnetických polovodičích [online]. 2009 [visited on 2024-12-07]. Available from: `https://dspace.cuni.cz/handle/20.500.11956/23162`. Accepted: 2017-04-19T19:30:15Z Publisher: Univerzita Karlova, Matematicko-fyzikální fakulta.

56. Zvezdin, A. K.; Kotov, V. A. *Modern Magnetooptics and Magnetooptical Materials*. Boca Raton: CRC Press, 1997. ISBN 978-0-367-80260-8. Available from DOI: `10.1201/9780367802608`.

57. Amaladass, E. *Magnetism of amorphous and highly anisotropic multilayer systems on flat substrates and nanospheres*. 2008. Available from DOI: `10.13140/2.1.2794.0168`. PhD thesis.

58. Schäfer, R. et al. Analyzer-free, intensity-based, wide-field magneto-optical microscopy. *Applied Physics Reviews*. 2021, vol. 8, p. 031402. Available from DOI: `10.1063/5.0051599`.

59. Higo, T. et al. Large magneto-optical Kerr effect and imaging of magnetic octupole domains in an antiferromagnetic metal. *Nature Photonics*. 2018, vol. 12. Available from DOI: `10.1038/s41566-017-0086-z`.

60. Yamada, K. T. et al. Magneto-optical Kerr effect of noncollinear antiferromagnetic Mn3Ir films. *AIP Advances* [online]. 2024, vol. 14, no. 8, p. 085020 [visited on 2024-11-12]. ISSN 2158-3226. Available from DOI: `10.1063/5.0217261`.

61. Schäfer, R. Investigation of Domains and Dynamics of Domain Walls by the Magneto-optical Kerr-effect. In: *Handbook of Magnetism and Advanced Magnetic Materials* [online]. John Wiley & Sons, Ltd, 2007 [visited on 2024-12-07]. ISBN 978-0-470-02218-4. Available from DOI: `10.1002/9780470022184.hmm310`. _eprint: https://onlinelibrary.wiley.com/doi/pdf/10.1002/9780470022184.hmm310

62. Zhou, C.; Xu, J.; Wu, T.; Wu, Y. Perspective on imaging antiferromagnetic domains in thin films with the magneto-optical birefringence effect. *APL Materials* [online]. 2023, vol. 11, no. 8, p. 080902 [visited on 2024-10-10]. ISSN 2166-532X. Available from DOI: `10.1063/5.0156439`.

63. Soldatov, I. V.; Schäfer, R. Advanced MOKE magnetometry in wide-field Kerr-microscopy. *Journal of Applied Physics* [online]. 2017, vol. 122, no. 15, p. 153906 [visited on 2024-10-15]. ISSN 0021-8979. Available from DOI: `10.1063/1.5003719`.

64. Soldatov, I. V.; Schäfer, R. Selective sensitivity in Kerr microscopy. *Review of Scientific Instruments* [online]. 2017, vol. 88, no. 7, p. 073701 [visited on 2024-10-15]. ISSN 0034-6748. Available from DOI: `10.1063/1.4991820`.

65. *Magneto-optical Kerr microscope & magnetometer – evico magnetics* [online]. [visited on 2025-01-07]. Available from: `https://evicomagnetics.com/productss/magneto-optical-kerr-microscope-magnetometer/`.

66. Amin, O. et al. *Altermagnetism imaged and controlled down to the nanoscale*. 2024. Available from DOI: `10.48550/arXiv.2405.02409`.

67. Hovořáková, K. Kerr microscopy of magnetic microstructures [online]. 2022 [visited on 2024-10-10]. Available from: `https://dspace.cuni.cz/handle/20.500.11956/171645`. Accepted: 2022-04-06T10:56:32Z Publisher: Univerzita Karlova, Matematicko-fyzikální fakulta.

68. Trejtnar, T. Testování nových optických zdrojů pro Kerrovskou mikroskopii [online]. 2024 [visited on 2024-12-07]. Available from: `https://dspace.cuni.cz/handle/20.500.11956/193848`. Accepted: 2024-11-28T14:25:33Z Publisher: Univerzita Karlova, Matematicko-fyzikální fakulta.

69. Yang, L.; Wang, Z.; Zhang, Z. Transport properties of MnTe films with cracks produced in thermal cycling process. *Applied Physics A*. 2017, vol. 123. Available from DOI: `10.1007/s00339-017-1264-z`.

70. White, G. K. Thermal expansion of reference materials: copper, silica and silicon. *Journal of Physics D: Applied Physics* [online]. 1973, vol. 6, no. 17, p. 2070 [visited on 2024-12-20]. ISSN 0022-3727. Available from DOI: `10.1088/0022-3727/6/17/313`.

71. Reig, C. et al. Growth and characterisation of MnTe crystals. *Journal of Crystal Growth* [online]. 2001, vol. 223, no. 3, pp. 349–356 [visited on 2024-12-23]. ISSN 0022-0248. Available from DOI: `10.1016/S0022-0248(01)00668-6`.

72. Yadava, R. D. S.; Bagai, R. K.; Borle, W. N. Theory of te precipitation and related effects in CdTe Crystals. *Journal of Electronic Materials* [online]. 1992, vol. 21, no. 10, pp. 1001–1016 [visited on 2024-12-23]. ISSN 1543-186X. Available from DOI: `10.1007/BF02684210`.

73. Hubert, M. et al. *Anomalous Spectroscopical Effects in an Antiferromagnetic Semiconductor* [online]. arXiv, 2024 [visited on 2024-12-23]. No. arXiv:2411.11673. Available from DOI: `10.48550/arXiv.2411.11673`.